UNIVERSITY OF OKLAHOMA

GRADUATE COLLEGE

APPLICATION OF A NOVEL LCMS METHOD TO ANALYZE POLAR BIOMARKERS OF THE WOODFORD SHALE, WYCHE FARM SHALE PIT, OKLAHOMA

A THESIS

SUBMITTED TO THE GRADUATE FACULTY

In partial fulfillment of the requirement for the

Degree of

MASTER OF SCIENCE

By

DEREK RUSSELL PARKS

Norman, Oklahoma

2021

APPLICATION OF A NOVEL LCMS METHOD TO ANALYZE POLAR BIOMARKERS OF THE WOODFORD SHALE, WYCHE FARM SHALE PIT, OKLAHOMA

A THESIS APPROVED FOR THE
SCHOOL OF GEOSCIENCES

BY THE COMMITTEE CONSISTING OF

Dr. Xiaolei Liu, Chair

Dr. Gerilyn Soreghan

Dr. Michael Engel

ACKNOWLEDGEMENTS

I would first of all like to thank Dr. Xiaolei Liu for his guidance, mentorship, and support from the beginning. He has believed in my capabilities and helped focus my research. The time he took to meet with me and discuss possibilities of the research has been invaluable and helped to progress my understanding of the field of geochemistry immensely.

I would also like to thank Dr. Engel and Dr. Gerilyn Soreghan for agreeing to serve on my committee and providing their time to review my thesis. Dr. Engel has provided his expertise and lab time for analyzing the organic carbon isotopes in this study proving to be incredibly helpful. Dr. Soreghan helped me to progress my scientific writing skills through the multiple classes I had with her allowing me to become a more adept writer. They both have my sincere gratitude.

My appreciation is also extended to Dr. Gregory Connock, for his enthusiasm and guidance in the lab. He taught me the proper lab procedures and techniques that were instrumental in keeping samples uncontaminated. His help in understanding the geochemistry of the samples also proved to be a valuable addition to this work.

The Geology department at OU is also deserving of gratitude. The generosity in providing funding and scholarships for my research allowed everything in my research and academic life to be possible. I would also like to thank the office staff on the 7th floor especially Rebecca Fay for providing assistance with anything I needed no matter how trivial or painfully obvious the question.

I very much appreciate the constant support provided by my family. Their support has pushed me to achieve this level of academia, without which would never have been possible. Their moral support has kept me driven to achieve this goal and their financial support has allowed me to focus on my studies.

Finally, I would like to thank my girlfriend, Amy Pham, for providing me with emotional support through all these years. The distance between us has been difficult but, even as she is busy with her own studies, she has always been there for me and made time to support me.

My deepest appreciation to you all.

TABLE OF CONTENTS

LIST OF TABLES

LIST OF FIGURES

ABSTRACT

This study examined the Wyche Farm-1 core and selected depths of interest for biomarker analysis. Previously employed methods for biomarker characterization were slow and labor-intensive using the gas chromatography mass spectrometer (GCMS), but this study utilizes a new method for the liquid chromatography mass spectrometer (LCMS) that requires minimal time and labor to produce comparable results. Applying this novel LCMS method, the previously undetected polar biomarkers, such as metalloporphyrins and newly identified tocopherol derivatives, are characterized in this study. Comparing results of aromatic carotenoids generated by both GCMS and LCMS yields, a general consistency in composition and depth profile, thus validating the new characterization method. However, due to the different procedures of sample preparation applied and standards used for quantification, the calculated absolute concentrations of aromatic carotenoids are two orders of magnitude higher for the GCMS method. Metalloporphyrin analyses indicates an unexpected high nickel porphyrin abundance during the euxinic Middle Woodford Shale evidenced by the distribution of aromatic carotenoids. This unexpected spike in nickel porphyrin concentration reflects a possible metal chelation preference related to the different molecular structures of BiCAP, DPEP and ETIO porphyrins, calling into question their use as reliable redox proxies. The MTTCs have been proposed as a salinity proxy in previous studies. However, our data show they possibly correlate to redox. The distribution of tocopherol derivatives likely reflects the population dynamics of phytoplankton resulting from the evolution of water chemistry during this time interval.

CHAPTER I

1. Introduction

The Woodford Shale is the richest and most important source rock in Oklahoma, holding the majority of the state's hydrocarbon reserves (Philp and DeGarmo, 2020). It is also a massive unconventional reservoir subject to increased interest along with other unconventional plays. The Woodford Shale is Late Devonian-Early Mississippian in age (Comer, 1991) and records an estimated 29 My of deposition (Johnson et al., 1985). During that length of time, significant variations in the depositional environment likely occurred. Sedimentation rate, redox conditions, light intensity, and water chemistry would have all varied, resulting in changes in the planktonic microbial communities. The resulting biological changes are recorded in the sediments by fluctuations in the organic geochemical and fossil biomarker compositions. Therefore, biomarker analysis of the shale provides an interpretation of the paleoenvironment that resulted in the sedimentation of the Woodford Shale. The Woodford Shale is conventionally separated into three sections, the Lower, Middle, and Upper.

Romero and Philp (2012) conducted geochemical analyses on the Wyche-1 core providing essential data about the environment of deposition through various hydrocarbon biomarkers. They found that the total organic carbon (TOC) of Woodford Shale ranged from 5.01 to 14.81%, and was marginally mature and dominated by type II kerogen. Using pristane, phytane, steranes, and hopanes they documented a mix of marine and terrigenous organic matter characterized by high-salinity conditions and a stratified water column. Turner et al. (2015) provided analysis of the trace metals in the same core using X-ray fluorescence (XRF)

and a detailed chemostratigraphic sequence for the Woodford Sale. Connock's (2015) work provided a geochemical analysis of the Woodford Shale to more accurately define depth and extent of photic zone euxinia during deposition. Using C_{40} aromatic carotenoids he documented episodic photic zone euxinia in the Lower Woodford Shale and sustained photic zone euxinia in the Middle Woodford Shale. In order to expand our knowledge of the temporal variation of Woodford Shale deposition environment, this project further refined the sampling resolution and focused on specific biomarkers of planktonic microbial communities by applying a completely new liquid chromatography–mass spectrometry (LCMS) based analytical protocol.

1.1 Geological Context and the Woodford Shale

The Woodford Shale is one of many black shales found worldwide that were deposited during the late Devonian and early Mississippian. These shales provide insight into many Earth processes such as the paleoclimate, paleogeography, eustasy, and tectonism (Ettensohn, 1992). These black shales accumulated during widespread anoxic events within epeiric seas while the planet was in a greenhouse climate (Jones, 2017). The late Devonian saw one of the five major mass extinction events, credited to two significant events called the Kellwasser and Hangenburg events (Jones, 2017; Molinares-Blanco, 2019). The Kellwasser can be split into two events, the Upper Kellwasser and the Lower Kellwasser. These events are contained within the Woodford Shale and likely contributed to the deposition and high preservation potential of the Woodford Shale.

Tectonic activity played a prominent role in the deposition of the black shales, as it would have formed the restricted basins required for the high preservation potential of organic matter and provided accommodation space for deposition (Johnson and Suneson, 1997). The Arkoma Basin is a foreland basin that strikes east-west from the Gulf coastal plain in central Arkansas to the Arbuckle Mountains in southcentral Oklahoma (Sutherland, 1988), (Figure 1).

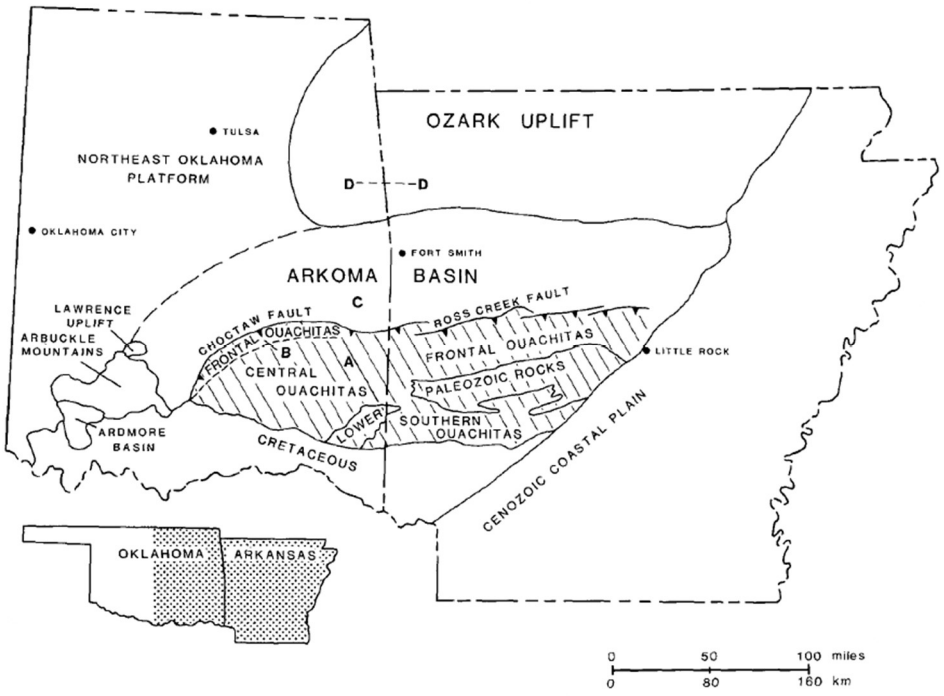

Figure 1. Arkoma basin of Oklahoma and Arkansas and the surrounding geologic provinces. (Sutherland, 1988)

It is structurally warped with many high-angle normal faults formed at deposition during the Ouachita orogeny (Johnson and Suneson, 1997), (Figure 2).

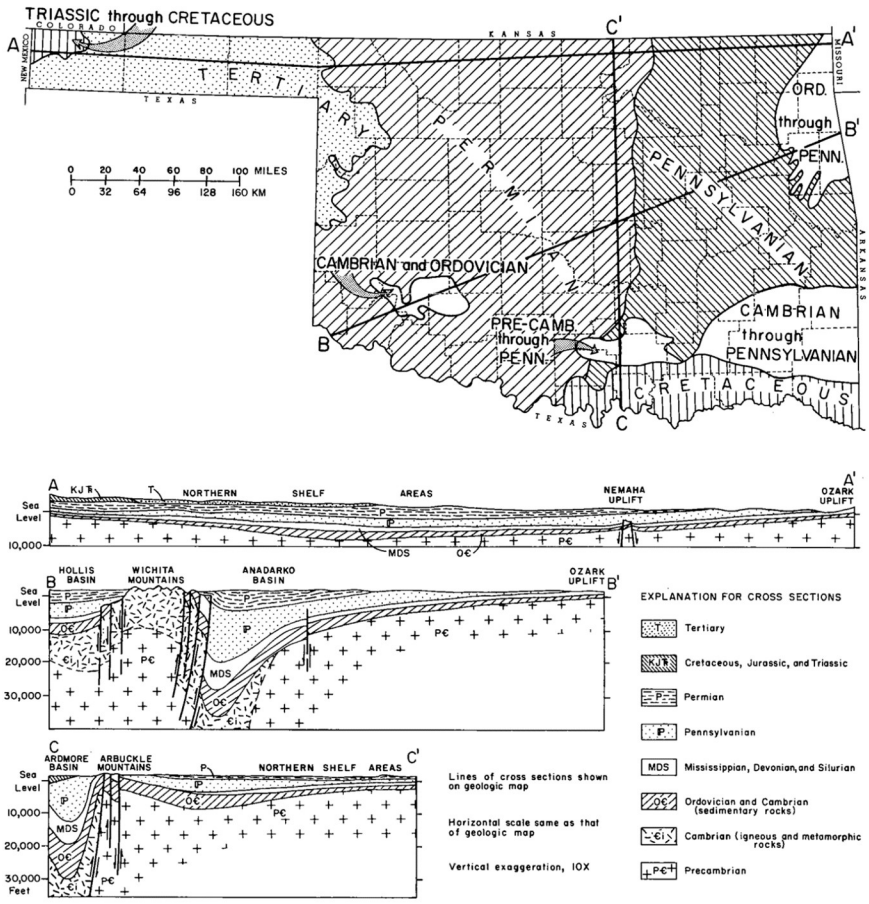

Figure 2. Geologic map and geologic cross sections of Oklahoma. Cross sections follow lines A-A', B-B', and C-C' on the map (Johnson and Suneson, 1997)

It has an area of about 87,500 km^2, with the maximum length being about 507 km and the maximum width being about 282 km (Perry et al., 1995). It is bounded on the north by the Ozark uplift and the Northeast Oklahoma platform (Figure 3). In the south, it is bounded by the Choctaw fault in Oklahoma and the Ross Creek fault in Arkansas (Sutherland, 1988). It is separated from the Ozark uplift by the south-dipping Mulberry Fault in the northeast. Finally, it is bounded by the Seminole Arch on the West (Suneson, 2012). It ranges from 914 to 6096 m in depth, where the deepest regions are in Oklahoma (Perry et al., 1995).

The Woodford Shale was deposited unconformably on top of the Hunton Group, which are shelf carbonates, and it is overlain by the Sycamore Limestone (Turner et al., 2016). It was formed by fine-grained siliciclastic hemipelagic rain and/or hyperpycnites and turbidites (Slatt et al., 2012a). The Woodford Shale ranges from 18 to 67 m thick (Turner et al., 2016). It crops out in the Lawrence Uplift with a thickness of less than 15 meters (Molinares-Blanco, 2013). The Lawrence Uplift occurred in the Pennsylvanian and is bounded by the Ahloso Fault in the north and the Stonewall Fault in the south (Portas and Slatt, 2010). The Woodford Shale in this study is in the Laurence Uplift and is about 37 meters thick; it is a core taken from the Wyche shale pit and the Wyche-1 well. The Woodford Shale is divided into three members, the Lower, Middle, and Upper. These divisions have been determined through various methods, each of which generally agree on where the divisions should be placed. Urban (1960) divided it by palynological data, whereas Over (1990) placed the divisions based on conodont stratigraphy. Gamma-ray spectroscopy has also been used to locate the divisions along with lithologic attributes (Abousleiman et al., 2007; Romero and Philp, 2012; Molinares-Blanco, 2013, 2019; Turner et al., 2015). The Lower Woodford Shale is characterized as black-gray, fissile, siliceous/carbonaceous shale (Molinares-Blanco, 2013, 2019; Turner et al., 2015). The Middle Woodford Shale is pyritic, black shale, which has the highest gamma-ray values resulting from the high organic matter (Slatt et al., 2012a; Molinares-Blanco, 2013, 2019). The Upper Woodford Shale is a quartzose, phosphatic gray-black shale which can be easily distinguished from the Lower Woodford Shale by the phosphate nodules and silicified logs it contains (Slatt et al., 2012a; Molinares-Blanco, 2013, 2019; Turner et al., 2015). In this study, the Wyche-1 well

core has the Upper-Middle Woodford Shale boundary at about 36 m and the Middle-Lower Woodford Shale boundary at 56 m (Romero and Philp, 2012; Connock et al., 2018).

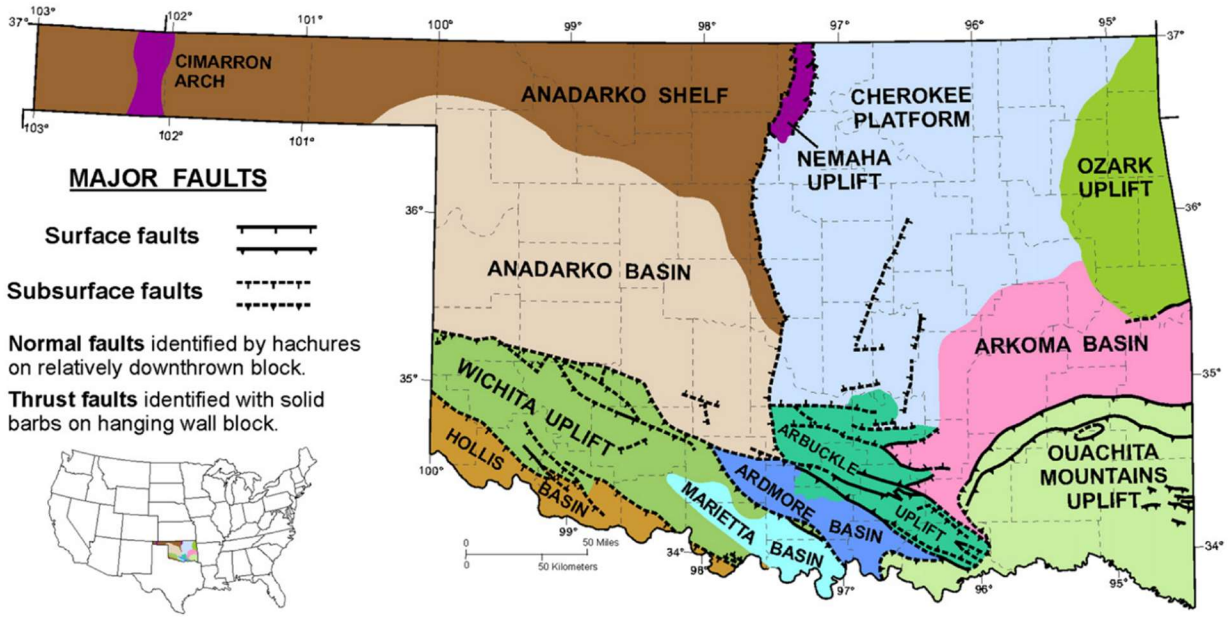

Figure 3. Modern geologic provinces of Oklahoma (Cardott, 2012)

In the Woodford Shale, total organic carbon (TOC) values range from 5.01-14.81% and are dominated by Type II and some Type I kerogens, with vitrinite reflectance (R_0) values of 0.29-0.63% (Romero and Philp, 2012). This indicates that the Woodford Shale is a high-quality source rock of low to moderate maturity. The pristane (Pr) and phytane (Ph) ratios, sterane (C30/C29), and terpane (C23 Tri/H) indicate the source of the organic matter in the sediments was a mixture of marine and terrigenous materials, which would have been deposited in anoxic bottom waters. High salinity also characterized the area of deposition, as evidenced by the gammacerane index. Gammacerane, along with aryl isoprenoids, indicates high stratification of

the water column and the presence of H_2S in the photic zone resulting in photic zone euxinia (PZE) (Romero and Philp, 2012; Connock et al., 2018).

In the Wyche-1 core, variations in the aryl isoprenoid ratio (AIR) indicate that the Upper and Lower Woodford Shale are characterized by episodic PZE and a more persistent PZE present in the Middle Woodford Shale. While the Woodford Shale contains a mix of marine and terrigenous organic matter, according to the ratios of C30 steranes/C29 steranes, hopanes/steranes, and C23 tricyclic/C30 hopanes, the Middle Woodford Shale shows the greatest marine input (Connock, 2015; Philp and DeGarmo, 2020). The Pr/Ph ratio and AIRs show that the lower and upper are characterized by dysoxic to suboxic conditions, and the middle is characterized by primarily euxinic and/or anoxic conditions (Romero and Philp, 2012). Gammacerane shows that while high salinity and water column stratification persisted throughout the deposition of the Woodford Shale, the Middle Woodford Shale shows the highest salinity and stratification (Connock, 2015). These geochemical proxies indicate that the Middle Woodford Shale was characterized by high organic productivity and preservation resulting from a shallow chemocline that entered into the photic zone. There is evidence for sea-level fluctuations and intermittent chemocline depth changes in the Lower and Upper Woodford Shale, resulting in episodic euxinia and oxidative periods, which degraded parts of the organic matter (Romero and Philp, 2012; Connock et al., 2018).

1.2 Sequence Stratigraphy

Sequence stratigraphy shows the relationships between sedimentary rocks within a chronostratigraphic or geologic-time framework (Catuneanu, 2017). It often relies on evidence of cyclical sea level rise and fall; sequences are created from this evidence, and causes for the cycles are interpreted (Posamentier and Vail, 1988; Posamentier et al., 1988). The Woodford Shale deposition responded to eustatic fluctuations. The sea-level cycle consists of a fall, a transitionary phase, and then a rise of sea level. The falling sea level is when the Lowstand Systems Tract (LST) is deposited. During the initial rise in sea level, the Transgressive Systems Tract (TST) is created, characterized by the abrupt rise in sea level. The Highstand Systems Tract (HST) is deposited later after the rapid initial rise in sea level when the rise is slower than the TST (Turner et al., 2016) as shown in figure 4 (Simmons, 2012).

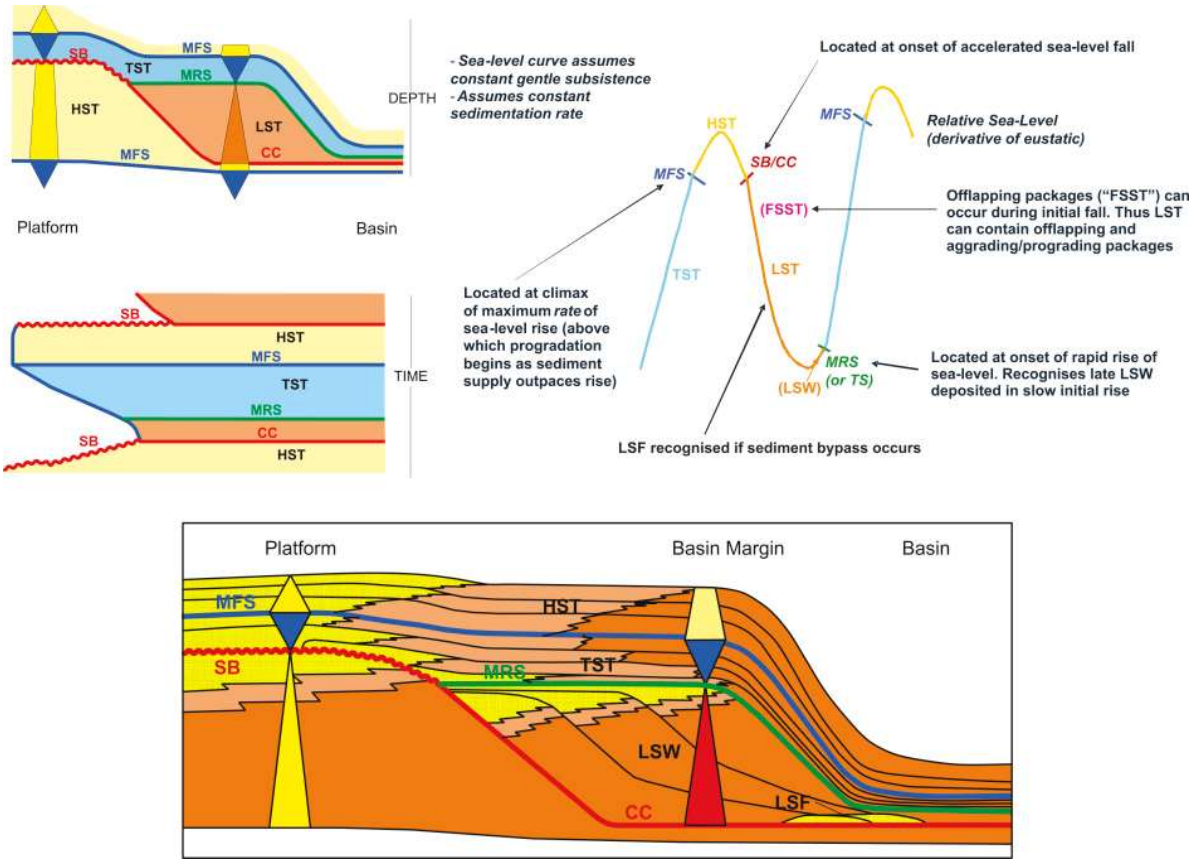

Figure 4. Relative sea-level curve comprising one complete cycle from one highstand to the next highstand. The falling limb represents the falling stage of the relative sea level and the rising limb represents the rising stage of the relative sea level. (Simmons, 2012)

These sequences are interpreted through characterization of the core using gamma-ray logs, SP logs, elemental analysis, TOC, and other sources (Buckner et al., 2009). Interpretation of these sequences helps to better understand the deposition of the rock unit of interest. The sequence stratigraphy of a rock unit will allow sections to be correlated regionally and locally.

Sequence stratigraphy alone does not give the most accurate record of geologic history; there are gaps in geologic time, fluctuations in sedimentation rates, and changes in accommodation space. Interpretation of these and other small-scale variations can be difficult with the traditional sequence stratigraphy framework used. Use of geochemical data can

enhance the resolution of the interpretations made. This enhanced resolution makes more accurate environmental interpretations possible. The TOC can be a helpful tool for determining where an interval fits in the sequence stratigraphic framework. If an interval has low TOC, it is interpreted as an LST (2%TOC or less); if the interval has higher organic matter (up to 10% TOC), then it is interpreted as a TST (Isaksen and Bohacs, 1995). Condensed sections lying between the late TST and the maximum flooding surface (MFS) at the beginning of the HST have the highest TOC and best source rock potential (Slatt et al., 2012b). This, however, is not always the case; in the Woodford Shale, the TST/HST boundary does not contain the highest TOC, but instead, the Middle Woodford Shale does and is characterized by an overall transgressive pattern (Molinares-Blanco, 2013).

In the Woodford Shale, high organic productivity is tied to the restriction of marine circulation. Topography underlying the Woodford Shale likely resulted in areas of restricted marine circulation resulting in organic-rich shale deposits (Molinares-Blanco, 2013). On the Wyche-1 core, the regressive and transgressive cycles were found based on gamma-ray readings (Buckner et al., 2009; Slatt et al., 2012a) as shown in figure 5 (Molinares-Blanco, 2013).

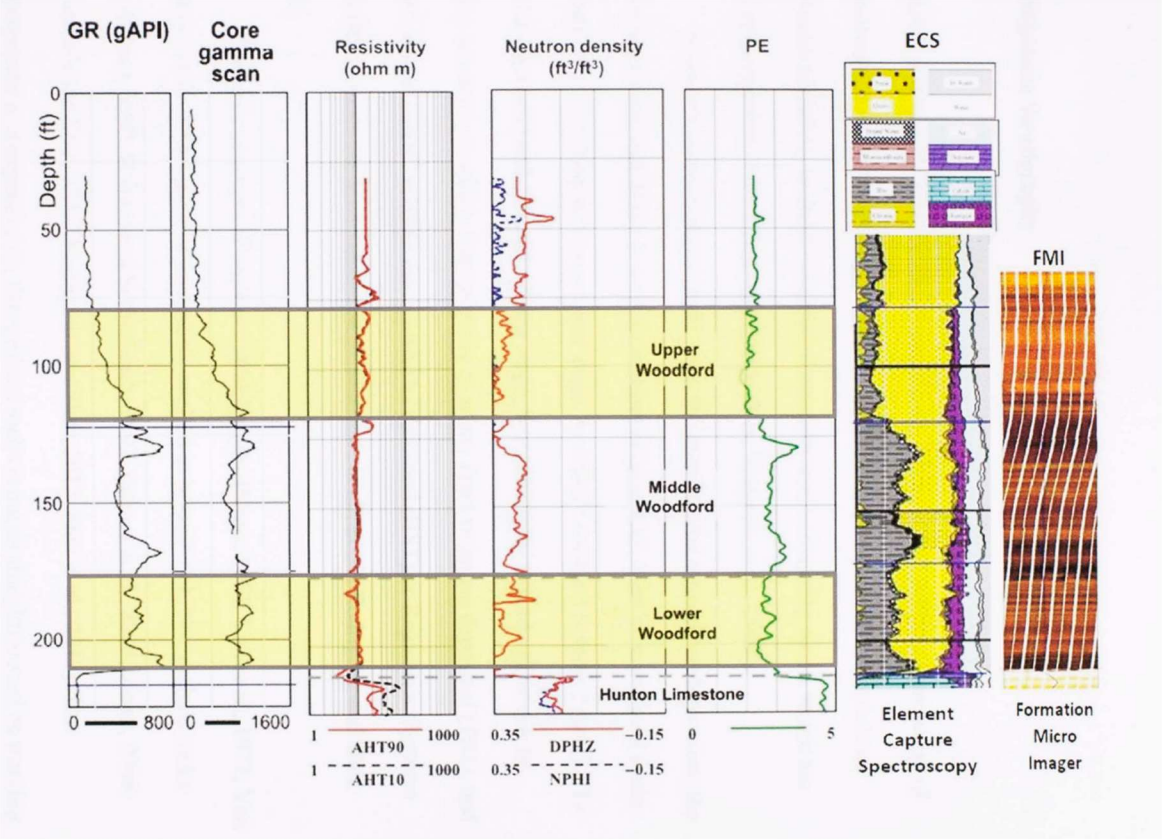

Figure 5. Borehole log data set from the Wyche-1 well. (Molinares-Blanco, 2013)

Romero and Philp (2012) used a geochemical approach to define the cycles, relying on relative hydrocarbon potential (RHP). The RHP is derived from Rock-Eval pyrolysis data ([S1+S2]/TOC) characterizing depositional environments and their temporal variations (Fang et al., 1993; Slatt et al., 2009). Using the RHP, the vertical organic facies changes or vertical organic facies sequences (VOFS) can be defined. There are two main VOFSs, rising-upward and falling-upward sequences. The rising-upward sequence shows a change in the organic facies vertically from hydrogen poor to hydrogen-rich, indicating a change from oxic to anoxic conditions and a sea-level rise. The falling-upward sequence shows a vertical organic facies change going from hydrogen-rich to hydrogen poor, indicating a change from anoxic to oxic conditions and a sea-

level fall. Rising-upward VOFS is where most organic matter is preserved, while falling-upward VOFS has less organic matter preservation. Romero and Philp (2012) found that based on RHP analysis of the Wyche-1 core, there were five falling and five rising stages of sea level in the Woodford Shale (Figure 6).

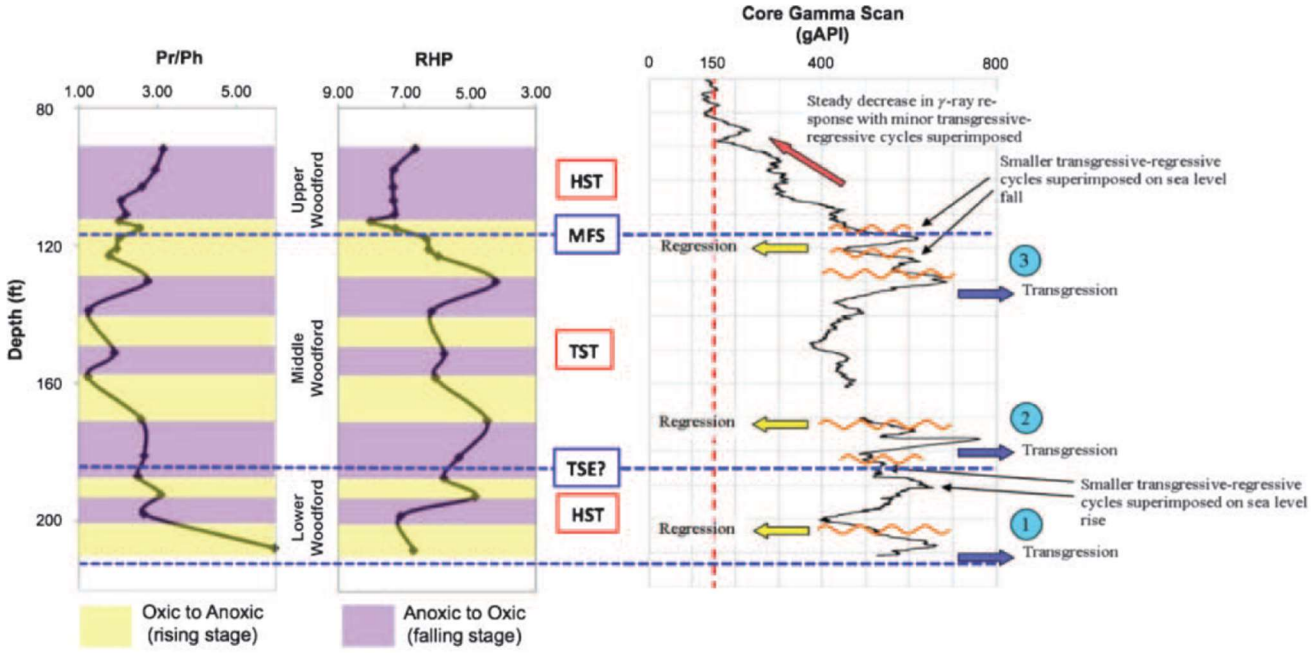

Figure 6. Sequence stratigraphic framework developed by RHP analysis and correlation to preexisting characterizations of the Woodford Shale (Romero and Philp, 2012)

At the base of the Lower Woodford Shale, there is a major transgression followed by a small regression and followed with another transgression. This interval corresponds to a transgressive/highstand systems tract (TST/HST) correlating to dysoxic to suboxic conditions. During the Middle Woodford Shale, a major transgression was found related to a possible TST or sea-level rise. The Middle-Upper Woodford Shale boundary is where the maximum flooding surface (MFS) occurs (Slatt et al., 2012a); this is followed by a regression, meaning that the

Upper Woodford Shale was deposited during a HST with high sediment input (Romero and Philp, 2012). These interpretations were later refined, resulting in nine different lithofacies being identified. The Lower and Middle Woodford Shale represent second-order TST; they were characterized by five 3rd order cycles. The Upper Woodford Shale represents a 2nd order HST with six 3rd order cycles (Molinares-Blanco, 2013); (Figure 7).

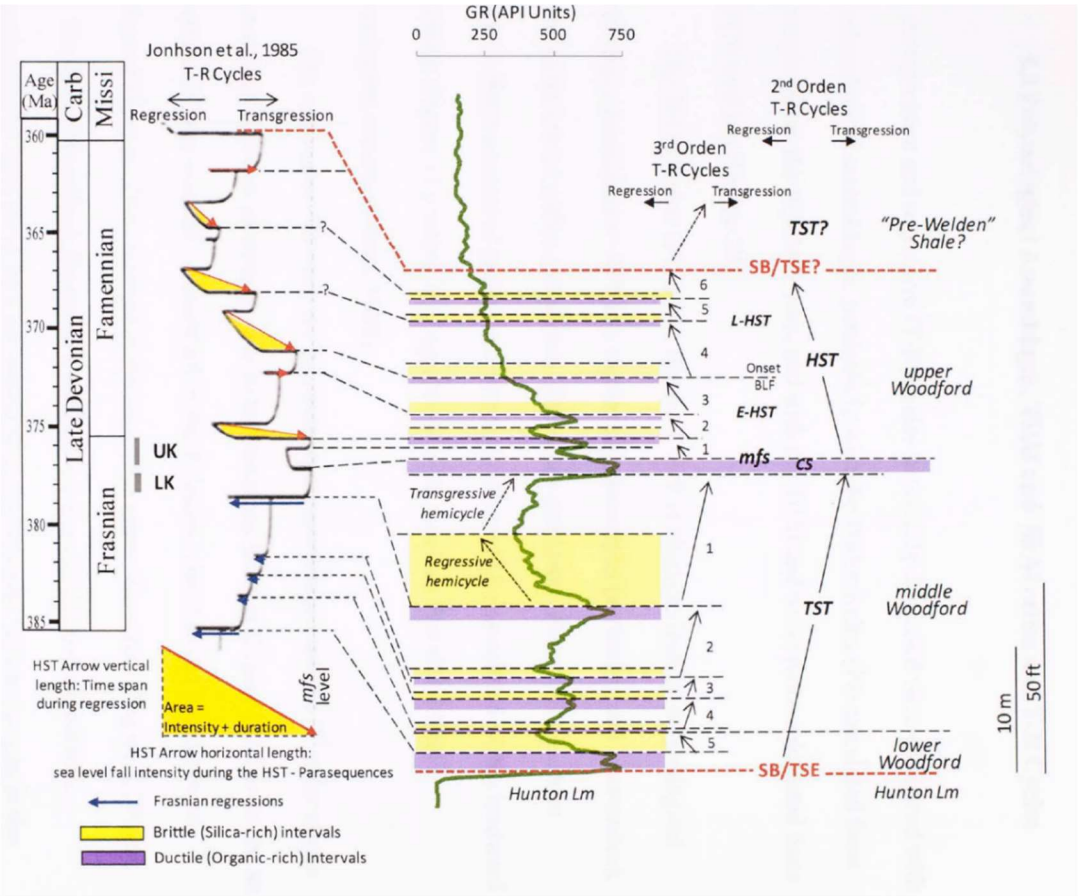

Figure 7. Sequence stratigraphic framework generated for the Wyche-1 core by Molinares-Blanco (2013). UK=Upper Kellwasser LK=Lower Kellwasser

Using gamma-ray logs (GR) and chemostratigraphy, the MFS was placed at 130 feet based on the GR, indicating increasing sea level through the Lower and Middle Woodford Shale (Turner et al., 2015, 2016). Chemostratigraphy further divides the sequences detecting four 4th order

parasequences indicating the retreat and advancement of the shoreline occurring during a 3rd order TST. The HST contains four 4th order parasequences detected by clay, biogenic quartz, and carbonate and detritus elemental proxies (Turner et al., 2015); (Figure 8).

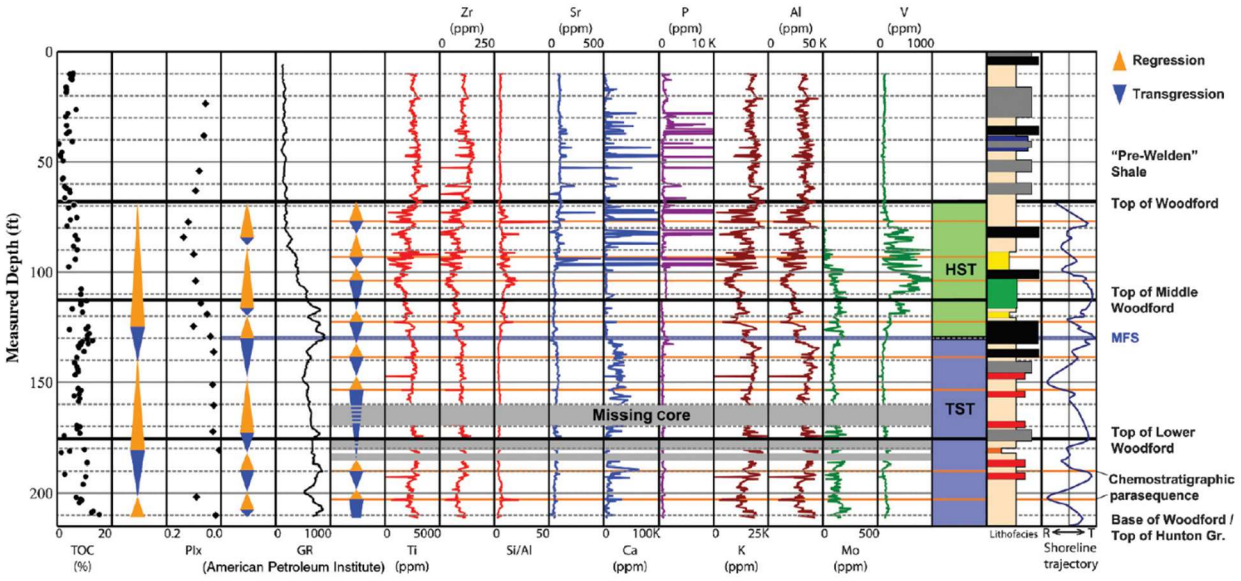

Figure 8. Gamma ray, trace element, organic richness, and pollen index logs of the Wyche-1 core. (Turner et al., 2015)

1.3 Mass Extinctions and the Frasnian-Famennian Boundary

Contained within the Woodford Shale is one of the five major mass extinction events. This mass extinction is considered to have resulted from two events in the Late Devonian; the first is the Kellwasser event at the Frasnian-Famennian boundary (F/F), which is often split into two separate events, the Lower Kellwasser (LK) and Upper Kellwasser (UK). The second is the Hangenberg event at the Devonian-Carboniferous boundary. During this extinction, 22% of all marine families and 50% of genera were lost (Algeo et al., 1995; McGhee, 1996). Shallow water families residing in the warm equatorial and tropical waters were most affected by this

extinction, while paleontological data shows polar families and those in deeper, cooler water fared much better (Copper, 1986). Jawless fish, brachiopods, ammonites, and trilobites were some of the most impacted by this extinction. However, the most significant losses were the warm water reef systems. Before the extinction events, warm-water reef systems covered 5,000,000 km^2, ten times modern reef systems; following the extinction events, they were reduced to less than 1,000 km^2 (McGhee, 1996). These reef systems would not even begin to recover until the Mesozoic era and arguably still have yet to recover to their previous prevalence (Algeo et al., 1995). The cause for these extinctions is still debated, but there are multiple hypotheses, many of which are complimentary. These hypotheses include vulcanism, bolide impact, land plant evolution, and algal blooms.

Volcanism and the bolide impact both left geochemical evidence during the D/C event at the top of the Woodford Shale. The volcanism hypothesis stems from elevated mercury found in multiple locations worldwide, showing concentrations approximately 12-84 times higher than background values (Rakociński et al., 2020). Elemental mercury is not necessarily toxic to life, but methylmercury (MeHg) does have a high toxicity. Concentrations of methylmercury are also elevated in the Hangenberg in multiple sites, including the Woodford Shale, where it has concentrations of 72.72 pg/g (Cullen, 2020; Rakociński et al., 2020). The bolide impact hypothesis stems from the finding of a large iridium (Ir) anomaly just prior to or at the D/C boundary. This anomaly exists in samples from around the world as well, with Woodford Shale samples showing a 250 pg/g Ir anomaly at the top of the section, which is well above the local 35 pg/g background Ir levels (Wang et al., 1993). Volcanic and hydrothermal activity plays an essential role in the global mercury cycle and acts as the primary source of mercury found in

sedimentary rock (Pyle and Mather, 2003; Grasby et al., 2019). There are, however other sources of mercury spikes, including wildfires, terrestrial input, magmatic emplacement, or thermogenic processes related to bolide impacts (Bergquist, 2017; Grasby et al., 2019; Rakociński et al., 2020). The most likely source remains large igneous provinces (LIPs); the Magdalen silicic LIP and Siberian (Yakutsk-Viluy) and/or Kola-Dnieper LIPs could be possible sources (Kravchinsky et al., 2002; Rakociński et al., 2020). While the iridium spikes in the Hangenberg seem like solid evidence of a bolide impact, it is not conclusive. No large impact craters, microtektites, or shock quartz are associated with these iridium spikes (Wang et al., 1993; Racki, 1999). This, however, does not rule out an impact between the Kellwasser event and Hangenberg. There is evidence of coarse slope breccias, coquinas, debris flows distributed over 200 km, and reef-margin collapses (Racki, 1999). These can be interpreted to be the result of megatsunamis possibly driven by an oceanic bolide impact. There could have been multiple small, closely spaced impacts (Wang et al., 1993; Racki, 1999). These Ir spikes all occur at redox, and facies change boundaries which implies they might have resulted from a sudden redox change (Wang et al., 1993).

Land plants and algal blooms create a feedback loop and result in the sequestration of large amounts of atmospheric carbon resulting in catastrophic global cooling. Land plants first appeared in the Late Ordovician or Early Silurian and began diversifying and growing in size during the Devonian (Mosbrugger, 1990; Algeo et al., 1995, 1998). There seems to be a correlation between the formation of black shales and the evolutionary milestones for land plants and their spread (Algeo et al., 1995). Land plant roots began breaking up rock and creating soils that increased silicate weathering, which, combined with forest fires and loss of

the retaining roots, meant more nutrients were flowing into the oceans, resulting in massive algal blooms. These algal blooms would have contributed to ocean water stratification and resulted in anoxia, increasing the preservation potential for organic matter. The increased burial of atmospheric carbon resulted in a drop in CO_2 levels from about 12-16 times present atmospheric level (PAL) during the early-middle Paleozoic to about 1 PAL in the Carboniferous (Algeo et al., 1995). The enrichment of conodont $\delta^{18}O$ by +1.5‰ across the F/F boundary indicates global cooling, translating to about a 5-6°C drop in global average temperature (Joachimski and Buggisch, 2002). Across the D/C boundary abiotic marine carbonate $\delta^{18}O$ was enriched by about +3‰, which corresponds to a roughly 26°C drop in tropical surface water temperatures (Algeo et al., 1995, 1998).

Carbon isotopes can also be used to locate these extinction boundaries, also supporting many of these extinction hypotheses. Carbon released from volcanic sources tends to be isotopically heavier, which would result in the positive excursion of $\delta^{13}C$. Land plant and algal blooms are enriched in isotopically light carbon due to kinetic fractionation; when the organic matter is buried in coal beds and organic-rich black shales, this sequesters the isotopically light carbon and results in the positive excursion of carbonate $\delta^{13}C$ (Algeo et al., 1995; Joachimski and Buggisch, 2002; Chen et al., 2005). There is a strong positive $\delta^{13}C$ excursion during both the Kellwasser and Hangenberg events which can be used to identify the location of these events in the core (Chen et al., 2005). This is done by comparing the global stable carbon isotopic curve to the stable isotope curve of a core and lining up the positive excursions associated with these events (Molinares-Blanco, 2019).

1.4 Biomarkers

Biomarkers are fossil molecules preserved in the sediments and hydrocarbons, derived from precursor molecules found in the organisms that lived at the time of deposition. Using biomarkers, the environment of deposition can be determined; they also can provide information on diagenesis, thermal maturation, biodegradation, and sediment source (Eganhouse, 1997; Farrimond et al., 1998). The utilization of biomarkers is also vital for industry. For example, biomarkers that indicate oxic or anoxic bottom water conditions can be used to evaluate the viability of potential gas-shale plays (Slatt and Rodriguez, 2012; Philp and DeGarmo, 2020). Biomarkers generally retain the molecular structure of their biological source, even after experiencing biodegradation, early diagenesis, and catagenesis. Using this preserved structure, it can be determined if the source of the molecule is a bacterial, algal, vascular plant, or animal source. The determination of the source can then be used to infer variations in the biosphere, chemosphere, geosphere, and atmosphere. The optimal preservation of these biomarkers during and after deposition requires anoxic conditions to prevent them from being consumed or degraded by oxygenation.

Carotenoids are pigment molecules synthesized in many different photosynthetic organisms (Hartgers et al., 1994). Some carotenoids are unique to specific organisms, making them useful as biomarkers and paleoenvironmental proxies (Grice and Brocks, 2011). In the Woodford Shale and for this study, the carotenoids of interest come from the family *Chlorobiaceae* in the phylum *Chlorobi* (Koopmans et al., 1996a). *Chlorobiaceae* are often referred to as green sulfur bacteria (GSB); these bacteria are obligate phototrophs and obligate autotroph anaerobes (Frigaard and Bryant, 2004; Frigaard et al., 2004). The GSB produce the

carotenoids isorenieratene, chlorobactene, paleorenieratane (**II**), and possess a unique organelle, the chlorosome, which contains bacteriochlorophyll (BChl) *c, d,* and *e* (Hartgers et al., 1994; Koopmans et al., 1996a; Frigaard and Bryant, 2004; Frigaard et al., 2004; French et al., 2015). The chlorosome allows GSB to inhabit deeper in the water column in the photic zone with low light intensities than it would otherwise be able to (Frigaard et al., 2003). In addition to light, GSB also require hydrogen sulfide (H_2S) as an electron donor for its metabolic function (van Gemerden, 1983; Frigaard and Bryant, 2004). The GSB incorporate carbon using the reversed tricarboxylic acid cycle (TCA), which results in the significant enrichment of ^{13}C in the biomass (Kohnen et al., 1992; van der Meer et al., 1998; Grice and Brocks, 2011). This isotopic signature is retained regardless of any structural changes during burial and diagenesis (Grice et al., 1996; Koopmans et al., 1996b). As a result of these unique attributes possessed by GSB, analyzing biomarkers indicating their presence provides compelling evidence of environmental conditions present at the time of deposition. Since they require hydrogen sulfide, light, and the lack of oxygen, finding evidence of their presence indicates that anoxia and sulfidic waters were shallow enough to be in the photic zone and thus indicate photic zone euxinia (PZE).

An important biomarker this study analyzes is isorenieratane(**I**). This biomarker is produced by the hydrogenation of the double bonds found along the isorenieratene chain (Hartgers et al., 1994). There are two types of GSB, the brown and the green versions. The brown version can live in low light conditions at depths up to 100 m, while the green versions are restricted to shallower waters at depths up to 15 m (Sousa Júnior et al., 2013; French et al., 2015); (Figure 9).

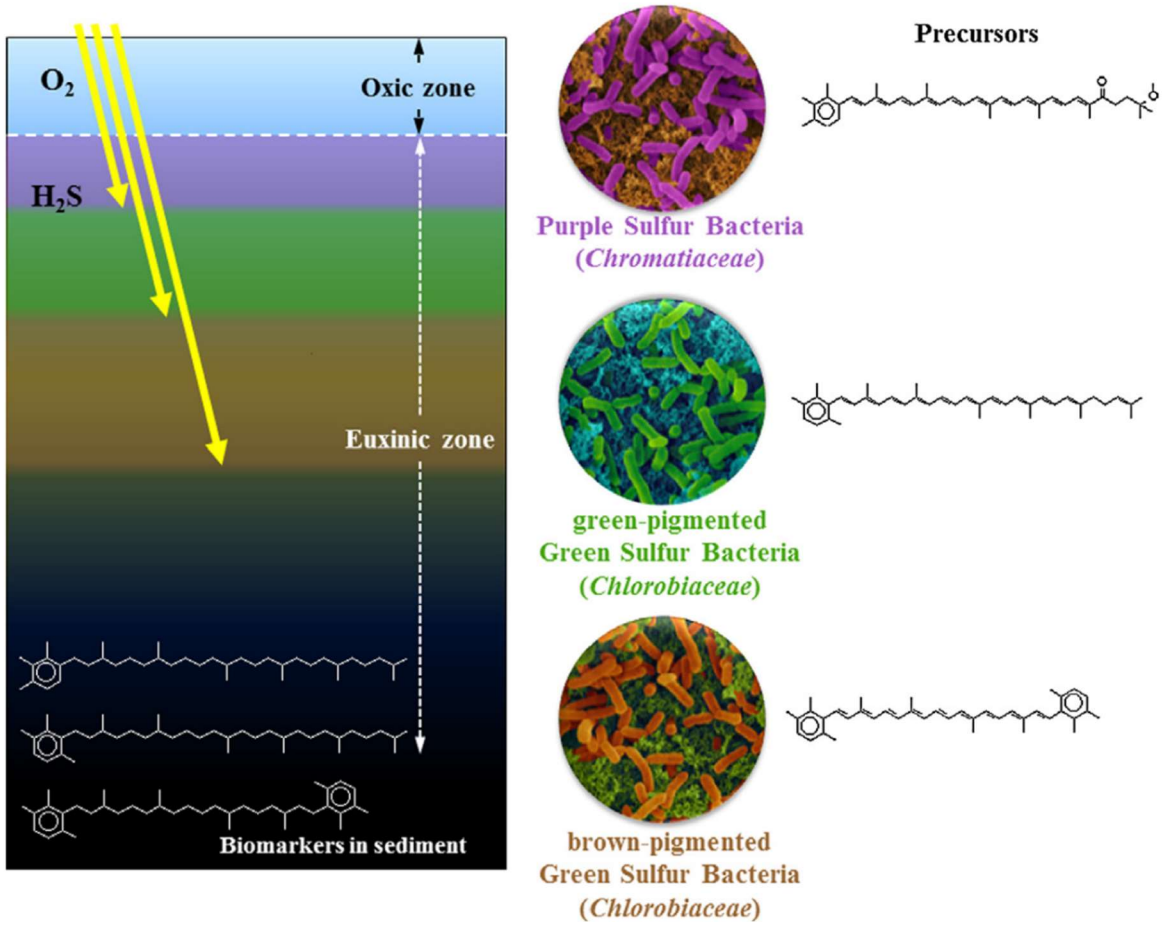

Figure 9. Water column structure and biology during times of euxinia. Marker molecule for each sulfur bacteria is shown beside it. (Sousa Júnior et al., 2013)

Isorenieratene is almost exclusively produced by the brown version of GSB, while the green GSB produces predominantly chlorobactene (van Breugel et al., 2005). Therefore, the detection of isorenieratane(**I**) can provide information about the depth of the chemocline and redox conditions present at deposition (Brocks and Schaeffer, 2008; Meyer and Kump, 2008; French et al., 2015). This study also looks at paleorenieratane (**II**), a 2,3,6-/3,4,5-trimethyl substituted C40 diaromatic carotenoid (French et al., 2015). First identified by Hartgers et al. (1993), it is thought to have been produced by a now extinct species of *Chlorobiaceae* (Hartgers et al.,

1993, 1994; Koopmans et al., 1996a; Clifford et al., 1998; French et al., 2015; Aderoju and Bend, 2018). It is also enriched in ^{13}C (Hartgers et al., 1993), much like isorenieratene (van Breugel et al., 2005, 2006), supporting the idea that it comes from photosynthetic GSB and is therefore an indicator of PZE. The GSB producing paleorenieratane (**II**) likely inhabited a shallower region than the isorenieratene producing GSB (Connock, 2015). Paleorenieratane (**II**) is also valuable for age dating, it is limited to being found between the Neoproterozoic and the Early Triassic, but the relatively high concentrations occur in the Devonian (Hartgers et al., 1994; French et al., 2015). The Woodford Shale contains both isorenieratane(**I**) and paleorenieratane (**II**) in high concentrations, with paleorenieratane (**II**) being dominant and isorenieratane(**I**) being the second most abundant (Connock, 2015).

Porphyrins were the first biomarkers identified in sedimentary organic matter (Treibs, 1936). They are molecular fossils resulting from the degradation of pigments such as chlorophyll, bacteriochlorophylls, and hemes (Huseby et al., 1996; Junium et al., 2008, 2015). They help determine paleoenvironmental data such as water column redox state, biological activity, sedimentary geochemical conditions, and geologic age (Junium et al., 2008). Porphyrins can also be indicators of organic matter source, diagenetic history, and petroleum thermal maturity (Huseby et al., 1996; Marín et al., 2014; Junium et al., 2015). Three classes of porphyrin were detected in this study, deoxophylloerythroetioporphyrin (DPEP), etioporphyrin (ETIO), and bicycloalkanoporphyrin (BiCAP). They can be produced by the diagenetic alteration of chlorophyll and bacteriochlorophyll (Ohkouchi et al., 2010; Fulton et al., 2018; Gueneli et al., 2018). The process of alteration begins first by losing the Mg, phytol, and the carbomethoxy moiety; it then undergoes keto reduction/dehydration/reduction; and is finally decarboxylated

to DPEP (Louda et al., 2000, 2011; Fulton et al., 2018), then a cyclization of the C-17 propionic acid substituent to form the seven-member ring for BiCAP (Junium et al., 2008). The ETIO in immature sediments is produced by oxidative cleavage of the isocyclic ring (Baker and Louda, 1983; Barwise and Roberts, 1984; Louda et al., 2011). The DPEP/ETIO ratio can indicate the thermal maturity of oils, where a decrease in the DPEP/ETIO ratio correlates to an increase in the maturity of the samples (Huseby et al., 1996; Marín et al., 2014). These porphyrins can form metallic complexes with many different available metal ions. Once these molecules have bonded with a metal, it flattens the porphyrin structure, significantly reducing its reactivity and making it geologically stable (Junium et al., 2015). This study will focus on analyzing the nickel (Ni^{2+}) and vanadyl (VO^{2+}) complexes. The relative proportions of nickel (Ni^{2+}) and vanadyl (VO^{2+}) indicate the Eh/Ph of deposition. The prominence of VO species is indicative of anoxic or euxinic conditions; this is due to sulfide-reducing bacteria producing hydrogen sulfide, which causes Ni to precipitate as nickel sulfide (Lewan and Maynard, 1982; Lewan, 1984; Huseby et al., 1996; Junium et al., 2008, 2015).

Methyltrimethyltridecylchromans (MTTCs) are a class of biomarkers that closely resemble vitamin E with the hydroxyl group in tocopherol at position six replaced by a hydrogen (Shanfa et al., 1989; Dutta et al., 2013). The MTTCs were first identified in geologic samples by (Sinninghe Damste et al., 1987) and are found in many sediments and crude oils. The MTTCs have the structure of methylated 2-methyl-2-(4, 8, 12-trimethyltridecyl) chromans and occur in distinct isomers of monomethyl (δ-MTTC), dimethyl (β-MTTC(**XIII**), γ-MTTC(**XIV**), ζ-MTTC(**XV**)), and trimethyl (α-MTTC(**XVI**)) homologs (Sinninghe Damste et al., 1993; Jiang et al., 2018, 2019). There has been much research on the origins of MTTCs, but it has all been

inconclusive. Many believe that they are biosynthesized by primary photosynthetic producers (Sinninghe Damste et al., 1993; Jiang et al., 2018, 2019); (Figure 10).

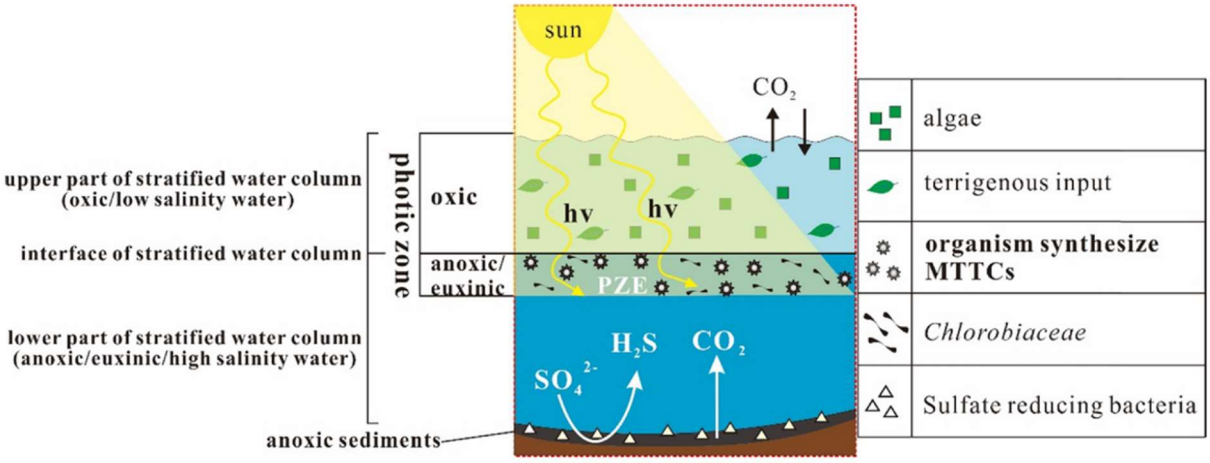

Figure 10. A conceptual model of the biosynthetic origin of MTTCs. MTTCs are suggested to derive from photosynthetic organisms originating in euxinic portions of photic zones (PZE). (Jiang et al., 2019)

However, Li et al. (1995) suggested that MTTCs may be non-biosynthetic, produced by a condensation reaction of alkylated phenols with phytol during early diagenesis. The MTTCs are used as a biomarker to assess the paleosalinity by looking at the α/δ-MTTC ratio. Low ratios (<2) indicate high-salinity conditions, whereas high α/δ-MTTC ratios (>100) reflect relatively low salinity (Shanfa et al., 1989; Sinninghe Damste et al., 1993; Dutta et al., 2013; Jiang et al., 2018, 2019). Another ratio used to indicate paleosalinty is the MTTCI (α-MTTC/total MTTCs), where MTTCI values less than 0.5 or 0.4 indicate high-salinity conditions and values greater than 0.5 or 0.4 indicate low-salinity conditions (Jiang et al., 2018, 2019). Variation in abundance for dimethyl MTTCs remain poorly understood and do not seem to correspond to salinity like the other isomers (Jiang et al., 2019). However, there does seem to be a positive correlation

between the abundances of δ-MTTC and (β+γ)-MTTC and a negative correlation between the abundance of α-MTTC and the abundances of δ-MTTC and (β+γ)-MTTC (Jiang et al., 2018).

Trimethylphytylbenzoquinone (TMPBQ(**XVII**)) is a novel compound tentatively identified by Connock (2021). Isomers of TMPBQ are also detected in the Woodford Shale. Individual isomers have not yet shown any potential for indicating anything significant. However, the TMPBQ/α-MTTC ratio has the potential to be used as a redox proxy

1.5 Objectives

There have been many biomarker studies performed on the Woodford Shale, but all are restricted to conventional GCMS based analysis. This study applies a novel LCMS method targeted on the polar biomarkers that are not amenable to GCMS. Aromatic carotenoids, such as isorenieratane(**I**) and paleorenieratane (**II**), are the most significant biomarkers recently studied in the Woodford Shale (Connock et al., 2018), and they can also be analyzed with the LCMS method. The samples studied by Connock et al. (2018) were reanalyzed to compare results generated with GCMS and LCMS. This allows assessment of the feasibility of this new method. This study will also expand the fidelity of isorenieratane(**I**) and paleorenieratane (**II**) in the Middle and Upper Woodford Shales, with new samples taken from the Wyche-1 core. This study also detects metalloporphyrins and attempt to use them to glean information on primary productivity, redox potential, and thermal maturity for the core. Analyses of MTTCs will provide information on salinity and primary productivity. Furthermore, a novel compound TMPBQ is measured and compared to other biomarkers in an attempt to investigate its geochemical

significance. Previous sample preparation methods used the Soxhlet extraction combined with column fractionation; while efficient, this method is time-consuming, limiting the number of samples that can be run. This work validates an ultrasonic bath extraction method that is much quicker, although less efficient. If this new analytical protocol is viable, characterization of black shales can become a rapid process. To summarize, the main objectives of this thesis project are:

1. Determine the feasibility of using the ultrasonic bath extraction and LCMS methods by reanalyzing samples run by Connock et al (2018) and comparing the results to provide a high throughput analytical method for aromatic carotenoids in black shales.
2. Expand the fidelity of isorenieratane(**I**) and paleorenieratane (**II**) in the Middle and Upper Woodford Shale to provide more data on the progression and evolution of photic-zone euxinia (PZE) and thus the paleoenvironment.
3. Use metalloporphyrins to indicate characteristics of the redox condition during Woodford Shale deposition. Provide insight into primary productivity at the time of deposition.
4. Use MTTCs to determine relative paleosalinity of the environment and as a possible indicator of primary productivity.
5. Compare the distribution of TMPBQ with other biomarkers to test its potential as a redox proxy.
6. Use $\delta^{13}C$ isotope curve and other biomarkers to further constrain the Frasnian-Famennian boundary.

7. Construct the evolution of water chemistry during Woodford Shale and the impact on planktonic microbial communities.

CHAPTER II

2. Methods

2.1 Area of Study and sample collection

The core used was the Wyche-1 core taken from the Wyche Shale Pit located at UTM: 14S X=7I6339 Y=3839956 (34.67875°N, -96.63864°E; Figure 11). Wyche-1 was drilled to be a research well, producing core and log data for the OU-Devon-Schlumberger enterprise. The total core length is approximately 200 ft. long, comprised of Woodford Shale and pre-Welden formations. There are portions of the core missing due to previous research projects and analysis, with the remaining core stored in cardboard boxes. Thirty-one rock samples were collected from Dr. Roger Slatt's core lab in Sarkey's Energy Center located on the main University of Oklahoma campus. An additional thirty samples were obtained from a previous thesis that had been obtained from the same source. Samples were taken from the core in whole pieces or as small chips where a portion was taken, leaving at least half of the core remaining for further study.

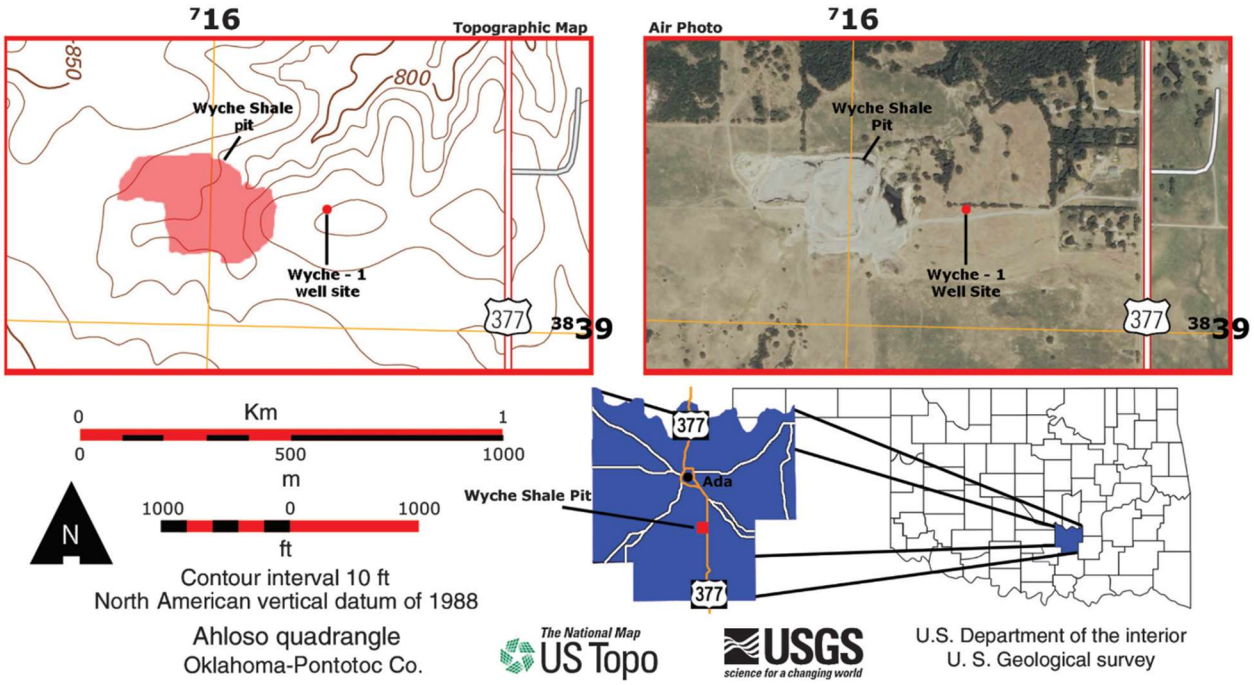

Figure 11. Location map of the Wyche Farm-1 core in Pontotoc County, Oklahoma. The coordinates on the side of the air photo and topographic map are in Universal Transverse Mercator. (Turner et al., 2015)

Sample	Depth (ft)	County	Global Position	Member
WCH-1	74.00	Pontotoc	2N 6E S2	Upper
WCH-2	75.50	Pontotoc	2N 6E S2	Upper
WCH-3	77.08	Pontotoc	2N 6E S2	Upper
WCH-4	78.00	Pontotoc	2N 6E S2	Upper
WCH-5	79.67	Pontotoc	2N 6E S2	Upper
WCH-6	80.67	Pontotoc	2N 6E S2	Upper
WCH-7	81.00	Pontotoc	2N 6E S2	Upper
WCH-8	84.50	Pontotoc	2N 6E S2	Upper
WCH-9	88.00	Pontotoc	2N 6E S2	Upper
WCH-10	91.50	Pontotoc	2N 6E S2	Upper
Wch-40	93.83	Pontotoc	2N 6E S2	Upper
WCH-11	94.33	Pontotoc	2N 6E S2	Upper
WCH-12	98.00	Pontotoc	2N 6E S2	Upper
WCH-13	102.17	Pontotoc	2N 6E S2	Upper
WCH-14	105.50	Pontotoc	2N 6E S2	Upper
WCH-41	109.17	Pontotoc	2N 6E S2	Upper
WCH-42	112.50	Pontotoc	2N 6E S2	Upper
WCH-15	115.00	Pontotoc	2N 6E S2	Upper
WCH-16	118.00	Pontotoc	2N 6E S2	Upper
WCH-17	121.00	Pontotoc	2N 6E S2	Upper
WCH-18	124.42	Pontotoc	2N 6E S2	Upper
WCH-43	126.17	Pontotoc	2N 6E S2	Upper
WCH-19	129.00	Pontotoc	2N 6E S2	Upper
WCH-20	130.00	Pontotoc	2N 6E S2	Middle
WCH-60	131.75	Pontotoc	2N 6E S2	Middle
WCH-61	132.75	Pontotoc	2N 6E S2	Middle
WCH-21	133.50	Pontotoc	2N 6E S2	Middle
WCH-44	134.00	Pontotoc	2N 6E S2	Middle
WCH-22	136.00	Pontotoc	2N 6E S2	Middle

WCH-23	137.25	Pontotoc	2N 6E S2	Middle
WCH-24	138.50	Pontotoc	2N 6E S2	Middle
WCH-25	139.67	Pontotoc	2N 6E S2	Middle
WCH-26	141.08	Pontotoc	2N 6E S2	Middle
WCH-27	142.25	Pontotoc	2N 6E S2	Middle
WCH-28	143.50	Pontotoc	2N 6E S2	Middle
WCH-45	145.17	Pontotoc	2N 6E S2	Middle
WCH-29	146.00	Pontotoc	2N 6E S2	Middle
WCH-30	147.08	Pontotoc	2N 6E S2	Middle
WCH-31	149.25	Pontotoc	2N 6E S2	Middle
WCH-46	153.58	Pontotoc	2N 6E S2	Middle
WCH-47	160.17	Pontotoc	2N 6E S2	Middle
WCH-48	160.83	Pontotoc	2N 6E S2	Middle
WCH-49	169.33	Pontotoc	2N 6E S2	Middle
WCH-50	170.92	Pontotoc	2N 6E S2	Middle
WCH-51	172.00	Pontotoc	2N 6E S2	Middle
WCH-52	172.42	Pontotoc	2N 6E S2	Middle
WCH-53	173.83	Pontotoc	2N 6E S2	Middle
WCH-54	174.42	Pontotoc	2N 6E S2	Middle
WCH-32	181.92	Pontotoc	2N 6E S2	Lower
WCH-33	185.92	Pontotoc	2N 6E S2	Lower
WCH-34	186.42	Pontotoc	2N 6E S2	Lower
WCH-35	187.75	Pontotoc	2N 6E S2	Lower
WCH-36	191.08	Pontotoc	2N 6E S2	Lower
WCH-55	191.33	Pontotoc	2N 6E S2	Lower
WCH-37	192.75	Pontotoc	2N 6E S2	Lower
WCH-38	193.75	Pontotoc	2N 6E S2	Lower
WCH-39	195.42	Pontotoc	2N 6E S2	Lower
WCH-56	203.08	Pontotoc	2N 6E S2	Lower
WCH-57	207.00	Pontotoc	2N 6E S2	Lower
WCH-58	209.92	Pontotoc	2N 6E S2	Lower

Table 1. Woodford Shale samples with associated depths and locations obtained from the Wyche-1 core for geochemical analyses

2.2 Experimental Procedure

2.2.1 Initial Sample Preparation

Rock samples were taken from the core by breaking off portions with a rock hammer while the sample was wrapped in combusted foil. The samples were rinsed with DI water to remove any dust on their outside, then rinsed with a 1:4 solution of dichloromethane (DCM) and methanol (MeOH) to remove any residual contaminants from handling, plastics, drilling mud, or other samples. The samples were then left to dry completely before being crushed. The samples were crushed to a fine powder using a clean porcelain mortar and pestle which was

cleaned between each sample by first rinsing with DI water, grinding combusted sand into powder, finally rinsing with 1:4 DCM:MeOH. The crushed rock powder was then stored in combusted glass jars.

2.2.2 Rock Eval Total Organic Carbon

Approximately 0.5g of each of the first 31 samples was transferred to a combusted 4mL vial and sent to the Research and Technology Center at Chesapeake Energy Corporation located in Oklahoma City, OK for bulk geochemical evaluations. The TOC analysis was performed on a LECO-C144 Carbon series. A combusted ceramic crucible was loaded with 25 mg of rock powder followed by the addition of 1mL of 5N HCl. The crucible was then heated to 115°C. Once the 5N HCl evaporated, an additional 1mL of 5N HCl was added and left to dry. The sample was then washed with 2mL of distilled deionized water and completely dried. The LECO C-230 Carbon Determinator was calibrated prior to sample analysis using five blanks and two carbon standards (5.02%, part no. 502-319 and 1.89% part no. 502-320) with identical accelerants for each sample measurement. One LECO metal scoop (part no. 773-579) of copper metal (part no. 501-263) and Lecocell II (part no. 501-008) accelerants were added to each sample before being loaded into the C-230 instrument. The two carbon standards were analyzed every 10 sample runs.

2.2.3 Extraction for Biomarker Analysis

Approximately 0.4-0.5g of crushed rock powder was transferred into a combusted 4mL vial using a spatula that was cleaned with a chemwipe and 1:1 DCM:MeOH between each

sample. The samples were spiked with standards 100ng of C46 GTGT, 1000ng of β-carotene, 1000ng of Vo-tetraphenylporphyrin (Vo-TPP), and 1000ng of Ni-tetraphenylporphyrin (Ni-TPP).

The samples then had 1.5mL of 1:1 DCM:MeOH added to them. They were mixed with a vortexer for a few seconds then sonicated for 20 minutes. After they had been sonicated, they were centrifuged for 5 minutes at 3000 rpm. The solvent was then transferred into a combusted and weighted 4mL vial which was then placed on a hot plate set to low and had nitrogen blown over them to evaporate the solvent. The extraction process was repeated a total of 4 times. After the 4^{th} extraction the solvent was dried completely and the vial and the total lipid extract (TLE) were weighed. If there was still color in the solvent after the 4^{th} extraction it was noted.

After weighing the TLE, 1mL of 1:1 DCM:MeOH was added to the 4mL vial and 500µL was transferred to a 2mL vial. The 2mL vial was then placed on the hot plate set to very low and had nitrogen blown over it until the solvent was completely dried. Then 1mL of MeOH was added into the now dried 2mL vial, the vial was then ultrasonicated for 5 minutes and centrifuged for 5 minutes at 3000 rpm. The solvent was then transferred into a new clean 2mL vial. The samples were then placed into the Q-TOF LC/MS for characterization. Figure 12 shows a graphic outlining the experimental procedure.

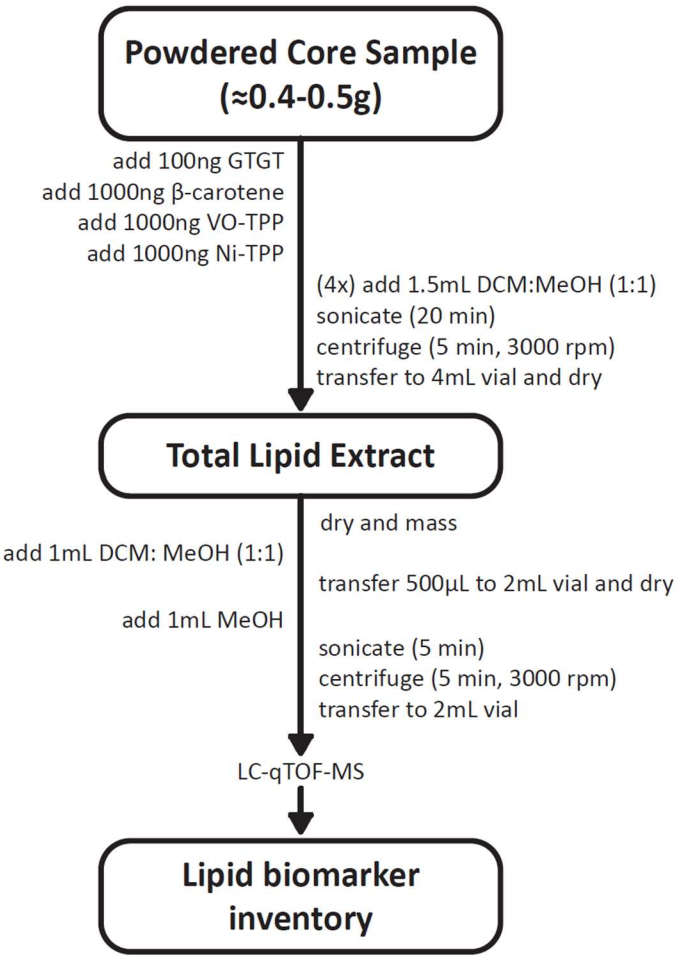

Figure 12. Experimental procedure for preparation, extraction, and analysis of biomarkers

2.2.4 Liquid Chromatography Quadrupole Time-of-Flight Mass Spectrometry (LC-qTOF-MS)

Analysis was done on an Agilent 1290 series UPLC system coupled with an Agilent 6530 qTOF mass spectrometer through an Agilent jet stream dual electrospray ionization (AJS-ESI) interface. As an ESI drying gas N_2 was used with a temperature set to 300°C, the flow rate of N_2 was 8 L min^{-1} with the nebulizer gas (N_2) pressure at 35 psi. The qTOF parameters were set to: capillary voltage 3.5 kV, fragmentor voltage 175 V, skimmer voltage 65 V, and octupole voltage 750 V in auto MS/MS scanning mode with an MS range of m/z 50-2000 and an MS/MS range of

m/z 20-2000. The collision gas used for CID was N_2. Depending on the application the CID voltage of collision cell was set from 40 to 200 eV. Compound separation was achieved by injecting 10 µl of sample into an ACE UltraCore Super C18 column (5 µm, 2.1 x 250 mm, ACE, Aberdeen, UK) maintained at 45°C. The LC program was set to have a flow rate of 0.2 mL min^{-1}, first hold 100% A for 5 min, to 70% A and 30% B to 25 min, followed by a gradient to 50% B at 50 min and hold for 5 min, and finally re-equilibrated with 100% A at a flow rate of 0.4 mL min^{-1} for 5 min. Eluent A was 95: 5: 0.04: 0.10 of methanol/H_2O/formic acid/14.8 M NH_3(aq.), eluent B was 50: 50: 0.04: 0.10 of hexane/2-propanol/formic acid/14.8 M NH_3(aq.).

2.2.5 Biomarker Detection and Quantification

Data analyses were performed by using Agilent MassHunter Qualitative Analysis software (version B.08.00). Compounds were detected based on their accurate masses, MS^2 fragmentation patterns and relative retention time. Peaks of targeted biomarkers were extracted with the type set to EIC (extracted ion chromatograph), MS level set to MS, polarity positive, the single m/z expansion set to symmetric (m/z) ±0.0200 for most of the samples and ±0.0250 for Wch-35-39,44-47. Compounds analyzed generally fell into three categories, carotenoids, metalloporphyrins, and MTTCs. Their concentrations are calculated using the equation below.

$$\frac{Compound\ peak\ area}{Standard\ peak\ area} * \frac{mass\ of\ standard\ injected\ (ng)}{wt\ OC\ (g)} = Compound\ concentration\ (\frac{ng}{g\ OC})$$

The aromatic carotenoids, MTTCs, and TMPBQ were all normalized using the C_{46} GTGT standard. The VO porphyrins were normalized using the VO-TPP standard and Ni porphyrins were normalized using Ni-TPP standard.

2.2.6 Carbon Isotope Measurement

Carbonate was completely removed prior to organic carbon isotopic analysis. Samples were placed into an acid-resistant tray, submerged in 3N HCl and let sit overnight. The following day, additional 3N HCl was added until there was no visible reaction. Samples were then brought to a neutral pH using water and dried completely before analysis. Approximately 1-2 ng of each sample was transferred to tin capsules (Costech 041074) and loaded onto a Costech zero blank autosampler attached to a Costech 4010 Elemental Analyzer (EA) interfaced to a Thermo Delta V Plus isotope ratio mass spectrometer (IRMS) via a Conflo III valve. Two reagents, silvered cobalt oxide (Costech 011007) and chromium oxide (Costech 011001) were used in the quartz combustion column held at 1000°C, while reduced copper wire (Costech 011013) was used in the reduction column held at 650°C. The gas chromatograph (GC) oven temperature was held at 55°C. Air was removed via a purge with high purity He before flash combustion, achieved by introducing a substantial O_2 pulse coincident with the sample drop. Helium was used as the carrier gas at a flow rate of 100 mL/min, transporting the combusted sample to a Thermo Conflo III interface that introduced sample to the ion source of the IRMS. The organic carbon isotopic composition ($\delta^{13}C_{org}$) was reported relative to the VPDB standard.

CHAPTER III

3. Results

The recovery of standard β-carotene is generally poor. This is likely due to the absorption of β-carotene by some yet uknown minerals rich in the shale and preventing its extraction, possibly related to the multiple double bonds in the central carbon chain of β-carotene. The real mechanism for organic molecule absorption to minerals requires further investigation to understand. Figure 13 shows the depth profile of each of the major compound groups side by side for ease of comparison.

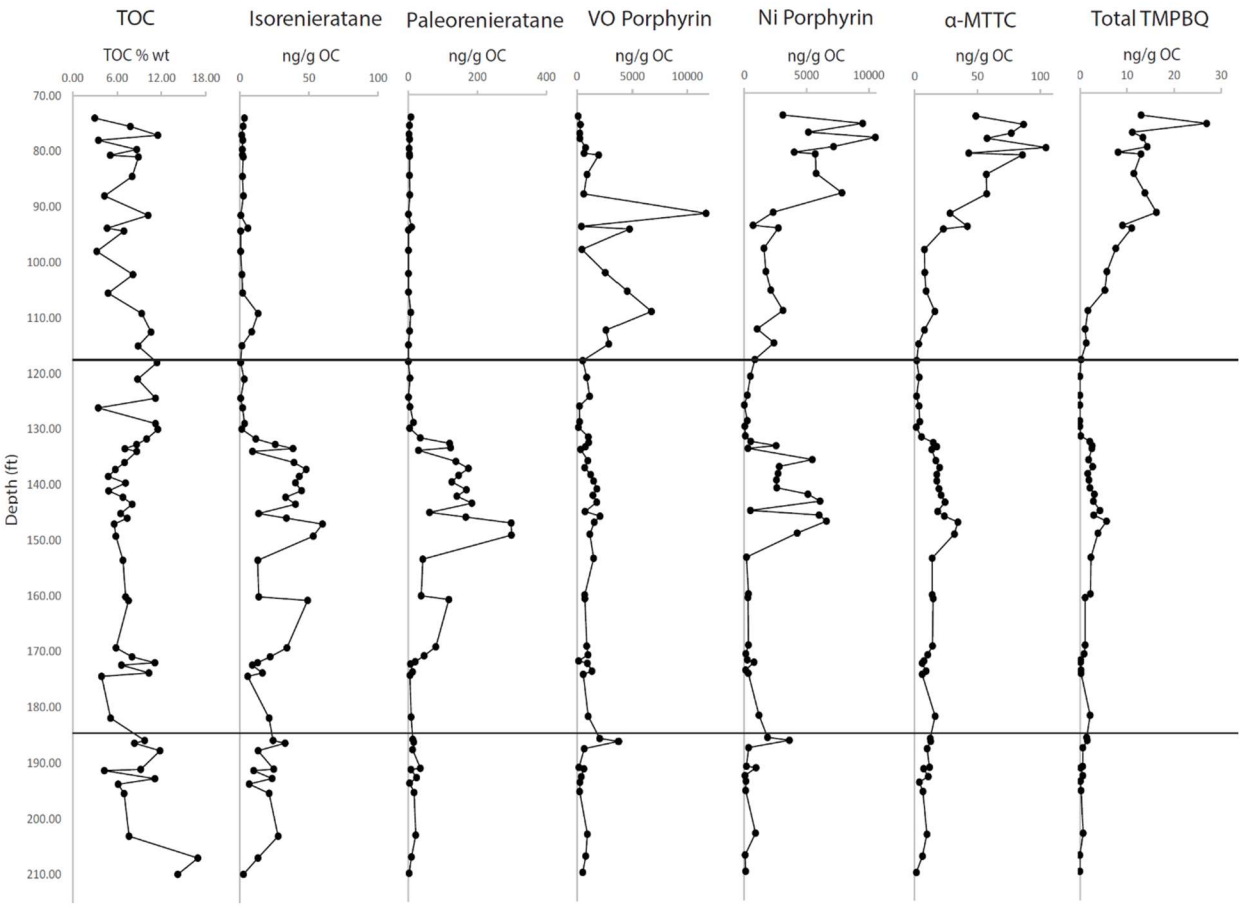

Figure 13. General Depth Plot of TOC, Isorenieratane(**I**), Paleorenieratane (**II**), VO-Porphyrin(**VII-XI**), Ni-Porphyrin(**X-XII**), α-MTTC(**XVI**), and Total TMPBQ(**XVII**)

3.1 Aromatic Carotenoids Derivatives

The carotenoids analyzed were C_{38}, C_{39}, isorenieratane, paleorenieratane, C_{41}, and C_{42} (Appendix I: **I-VI**; Appendix III: **I-VI**). An example of a chromatogram and the structure of isorenieratane and paleorenieratane is seen in figure 14.

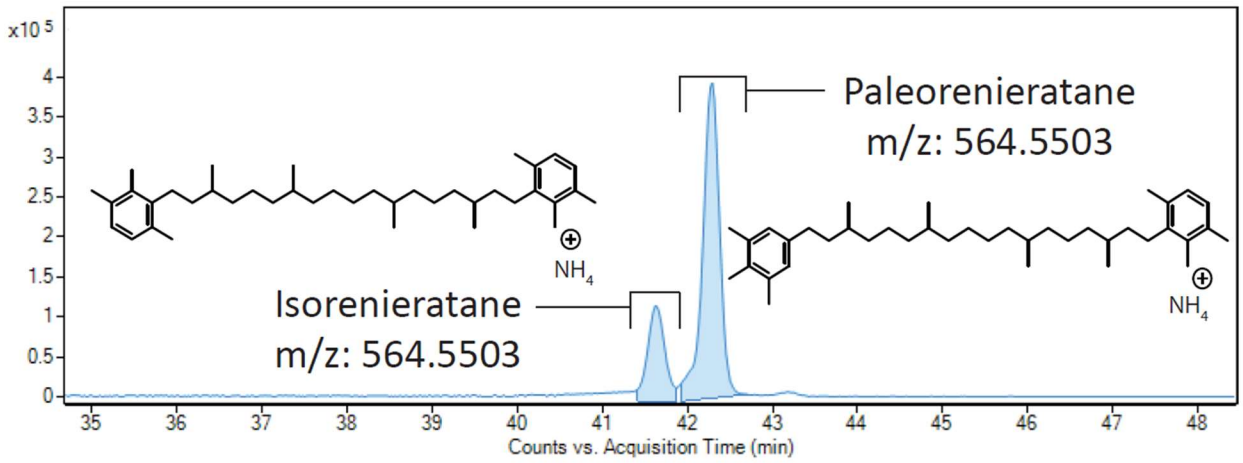

Figure 14. Example of the chromatogram and molecular structures for isorenieratane and paleorenieratane.

There is some variability in the concentrations in the Lower Woodford Shale for each of the compounds although they remain relatively low before decreasing around the Lower/Middle Woodford Shale boundary. Aromatic carotenoids generally show a significant increase in abundance during the Middle Woodford Shale (Figure 15). Beginning at about 170.00 ft the abundance begins to increase and almost completely drops off in concentration at about 130.00 ft. There is also much variability in the concentrations in the Middle Woodford Shale with low concentrations between 160.17-153.58 ft, 145.17 ft, and 134 ft. They all reach their peak concentrations at 147.08 ft except for the C_{42} Carotenoid which sees a peak at 132.75 ft. The concentrations detected are nearly zero in the Upper Woodford Shale, with only C_{39},

isorenieratane(**I**), and paleorenieratane(**II**) showing small isolated peaks at 109.17 ft and 93.83 ft. The peak and subsequent decrease corresponds to a general transgression and lithology change seen in the core (Figure 16). In figure 16 the general regression ends at around 150 ft and begins the general transgression, this is close to where the carotenoid concentrations peak and then begin to decrease. The lithology here changed from mixed siliceous/argillaceous mudstone with thin clay laminations to black to dark gray laminated argillaceous mudstone.

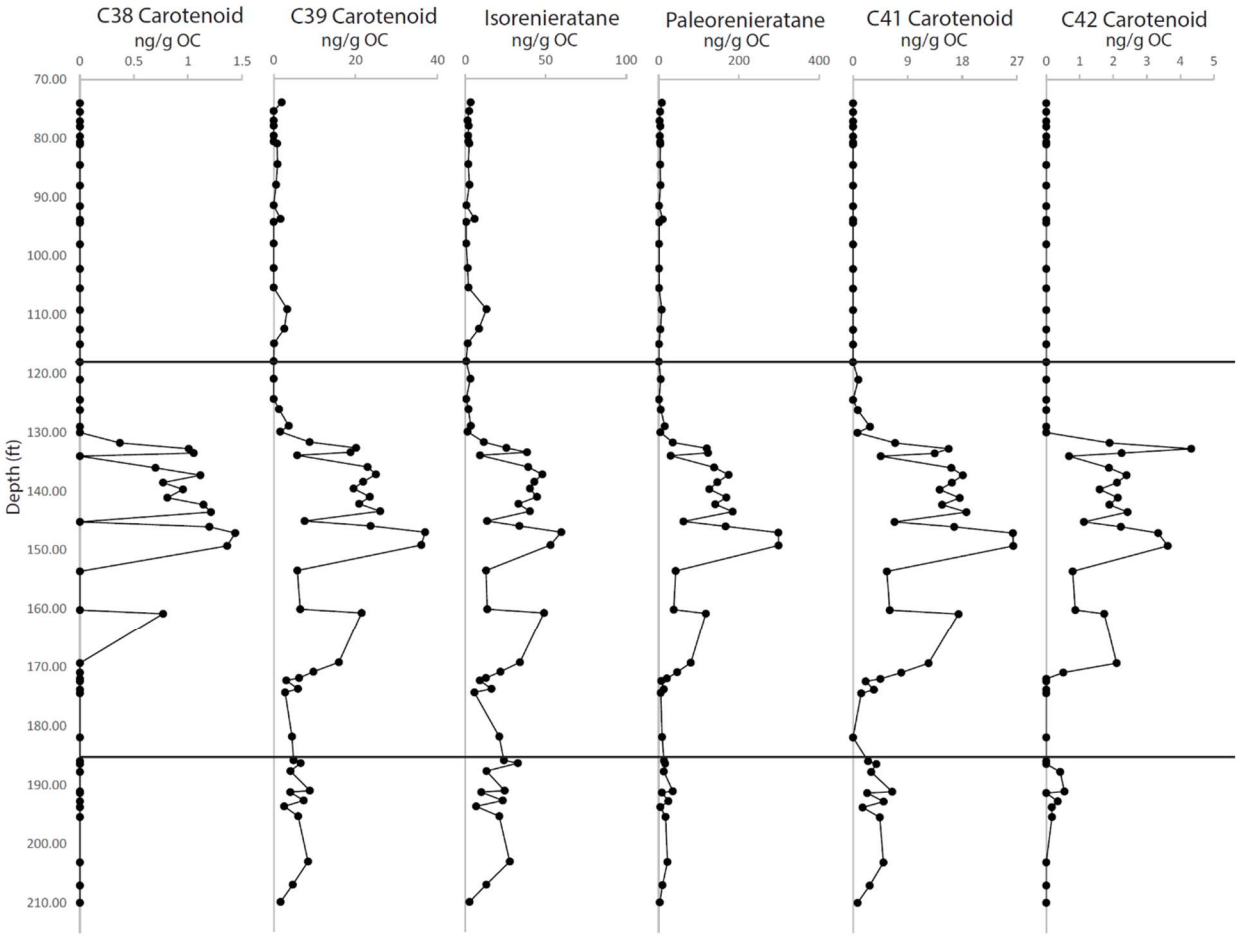

Figure 15. Depth profile of the Aromatic Carotenoid Methylation Derivatives(**I-VI**). The line at 118ft divides the Upper Woodford Shale and the Middle Woodford Shale, the line at 185ft divides the Middle Woodford Shale and the Lower Woodford Shale

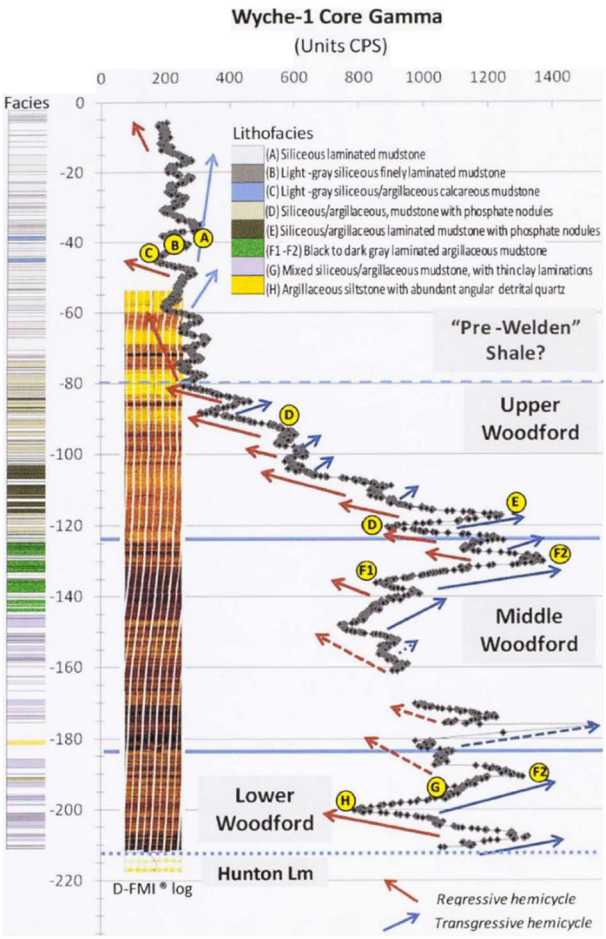

Figure 16. Gamma profile of the Wyche-1 core correlated to the lithofacies of the core. Red arrows represent regressive cycles and blue arrows represent transgressive cycles. Dashed lines represent unconformities at the top and bottom of the Woodford Shale. Figure modified from (Molinares-Blanco, 2013).

3.2 Porphyrins

Porphyrins can be indicators of primary productivity since they are degradation products of chlorophylls and bacteriochlorophylls (Huseby et al., 1996; Junium et al., 2008, 2015). In all analyzed samples no free base porphyrins were detected. Metalloporphyrins can be indicators of thermal maturity (Baker and Louda, 1983; Barwise and Roberts, 1984; Chen and Philp, 1991; Huseby et al., 1996; Marín et al., 2014), water column redox state (Chen and Philp,

1991; Huseby et al., 1996; Junium et al., 2008, 2015), and diagenetic history (Barwise and Roberts, 1984; Huseby et al., 1996; Junium et al., 2008, 2015; Louda et al., 2011). The concentrations of the metalloporphyrins that were detected in these samples are interesting when compared to the carotenoid data found in this study and will be explained in the Discussion section. For each category of metalloporphyrin multiple compounds were detected. See Appendix I (**VII-XII**) for molecular weights detected and the tentatively assigned structures. The metalloporphyrins analyzed where chelated with VO^{2+} and Ni^{2+} and consisted of BiCAP, DPEP, and ETIO. The VO metalloporphyrins consisted of C_{31}-C_{33} BiCAP, C_{29}-C_{32} DPEP, and C_{29}-C_{32} ETIO. The dominant species of each category, C_{33} VO-BiCAP, C_{32} VO-DPEP, and C_{32} VO-ETIO are shown in figure 17.

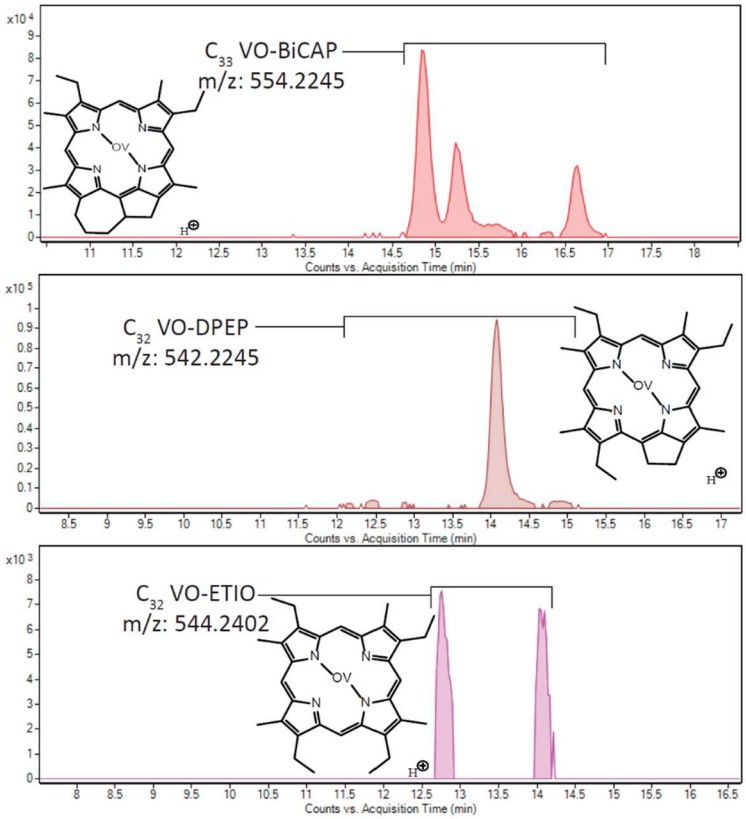

Figure 17. Example of the chromatograms and molecular structures of the major compound detected for each class of VO metalloporphyrins

The Ni metalloporphyrins consisted of C_{31}-C_{33} BiCAP, C_{30}-C_{32} DPEP, and C_{27}-C_{32} ETIO. The chromatogram and structure of the dominant species of each is shown in figure 18.

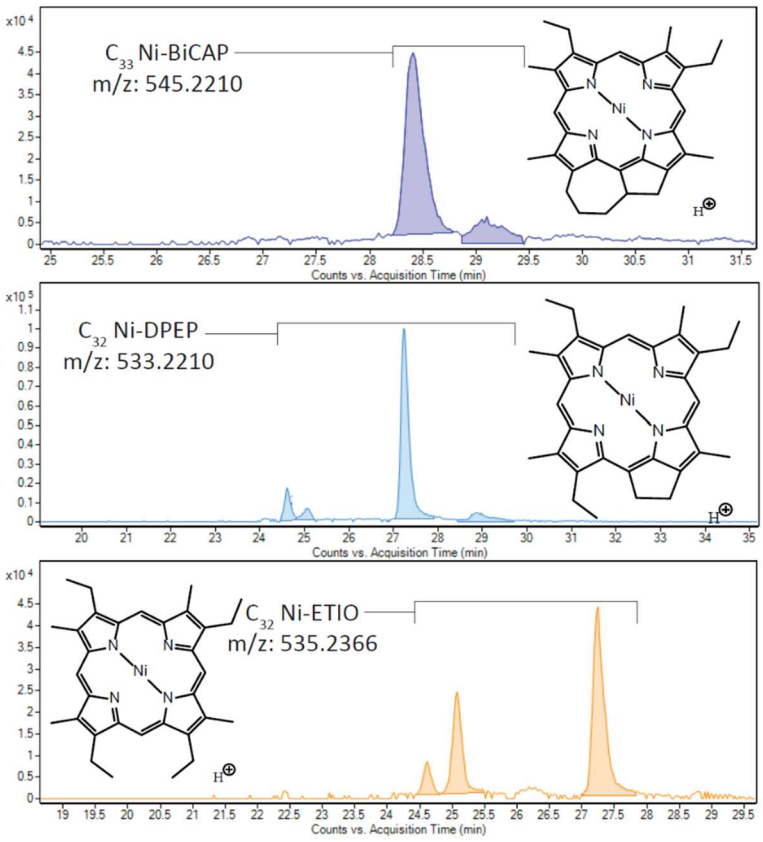

Figure 18. Example of the chromatograms and molecular structures of the major compounds detected for each class of Ni metalloporphyrins.

For the depth profiles in figure 19 each of these compounds in the class were summed for the total concentration. The vanadyl species each have similar profiles with peaks with similar retention times. They are low in the Lower Woodford Shale with a peak right before the Lower/Middle Woodford Shale boundary at 186.42 ft then decreasing and remaining low through most of the Middle Woodford Shale before seeing an increase at 160.17 ft, peaking at

146.00 ft, and then returning to low concentrations at 130.00 ft. Then beginning in the Upper Woodford Shale their concentrations increase dramatically corresponding to the increased oxygenation seen in the Upper Woodford Shale. The nickel species also have very similar depth profiles. They show low concentrations in the Lower Woodford Shale with a peak at 186.42 ft right before the Lower/Middle Woodford Shale boundary. In the Middle Woodford Shale they have low concentrations until at 153.58 ft they begin to increase in concentration peaking at 147.08 ft then dropping to low concentrations again at 131.75 ft. In the Upper Woodford Shale they increase dramatically much like the VO compounds but after the VO peak at 91.50 ft and its subsequent drop off in concentration the Ni compounds continue to increase with their overall peak concentrations at 78.00 ft. In the Middle Woodford Shale their increase in concentration corresponds to the peak and subsequent decrease in concentration of the aromatic carotenoids. This means they also correspond to a general transgression and lithology change seen in the core.

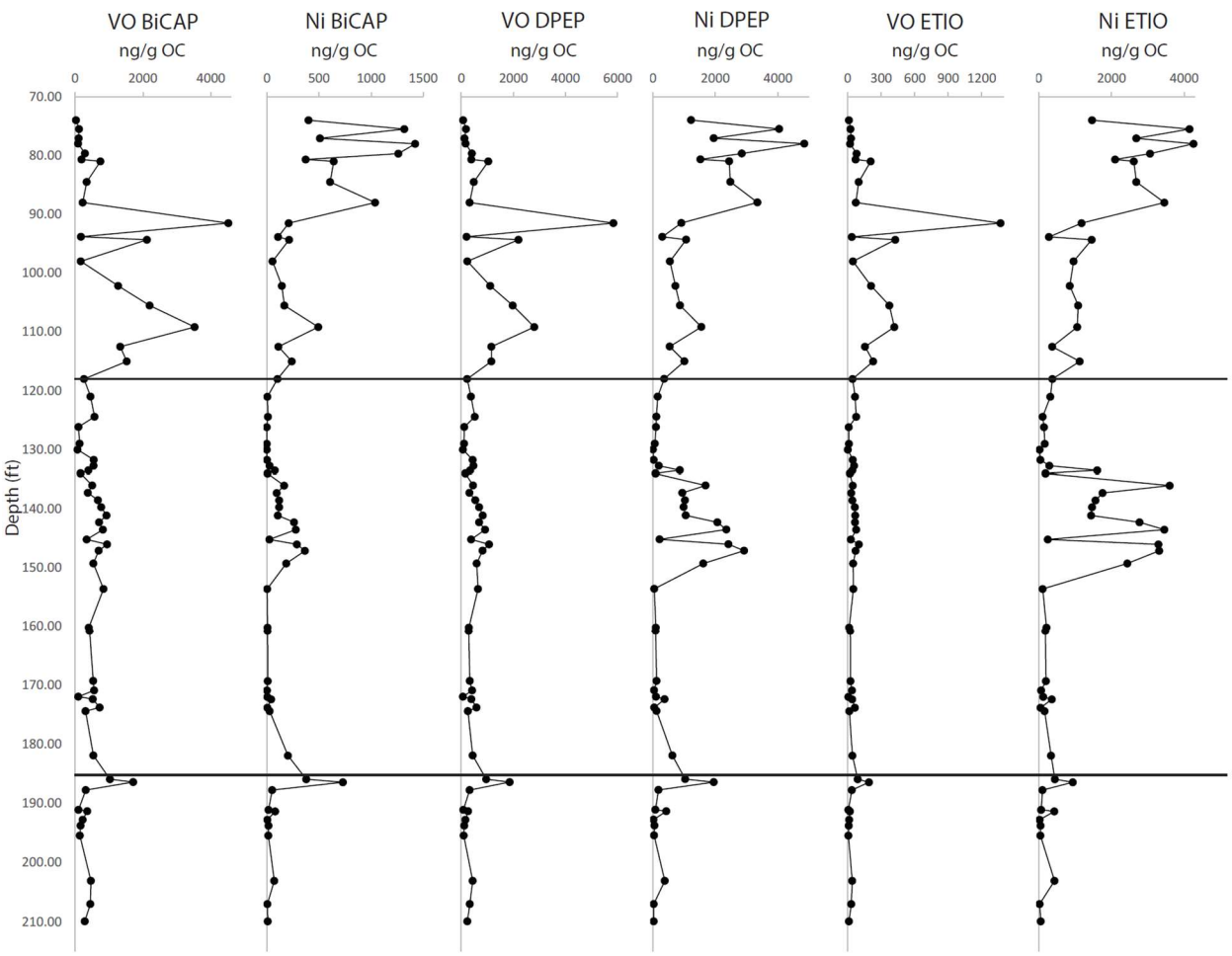

Figure 19. Depth profile of the metalloporphyrins. The line at 118ft divides the Upper Woodford Shale and the Middle Woodford Shale, the line at 185ft divides the Middle Woodford Shale and the Lower Woodford Shale.

3.3 MTTC

The MTTCs analyzed were β-MTTC, γ-MTTC, ζ-MTTC, and α-MTTC (Appendix I: **XIII-XVI**).

The chromatograms and structures of these compounds are shown in figure 20.

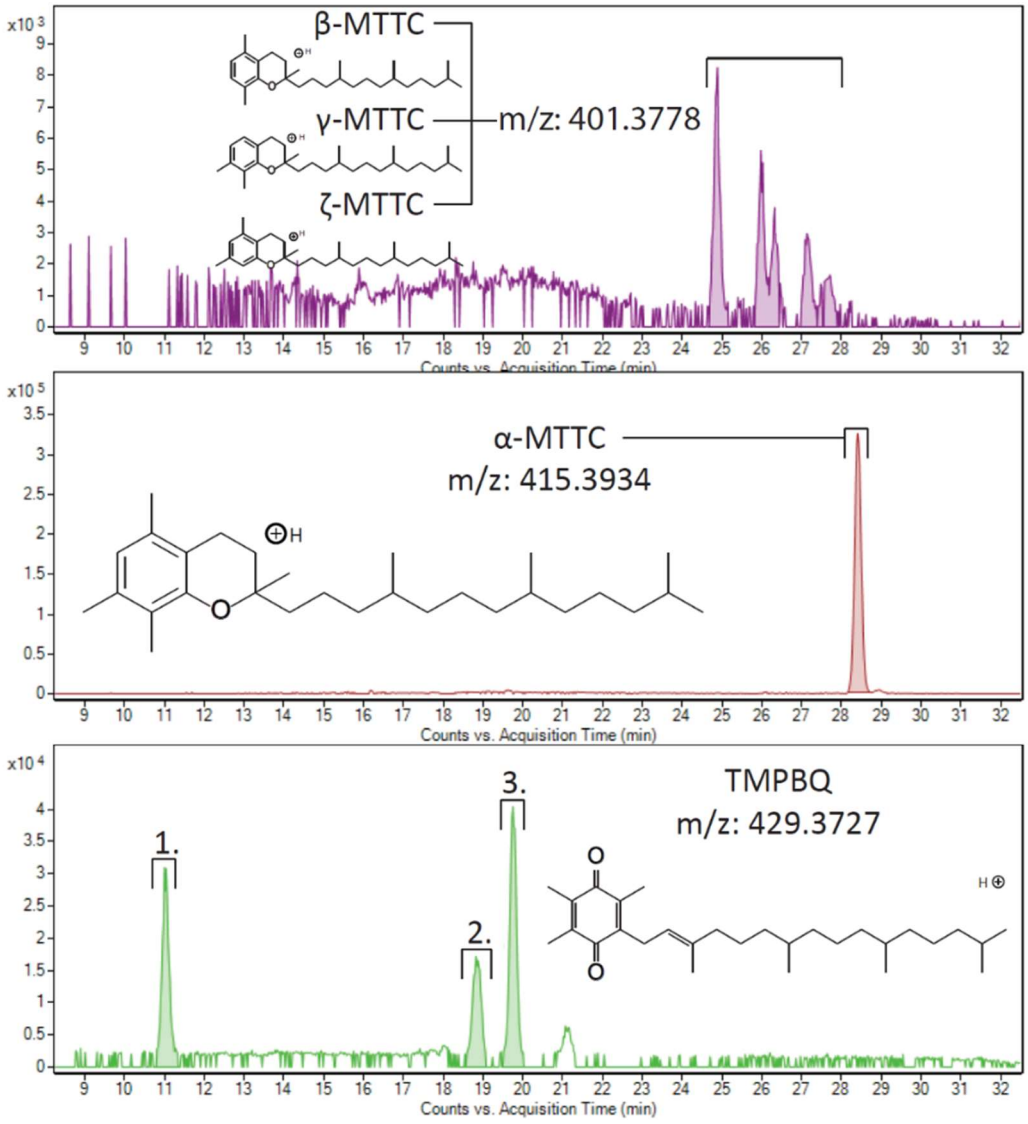

Figure 20. Chromatograms and molecular structures of the MTTCs and of TMPBQ. The first chromatogram shows the demethylated MTTCs, there are three peaks but without a proper standard individual peaks for each isomer can not be determined. The second chromatogram shows the trimethylated MTTC. The third chromatogram shows TMPBQ with each of the isomer peaks identified as 1, 2, and 3.

It is widely thought that MTTCs are biosynthetic in origin being produced by a yet unidentified photosynthetic organisms living in PZE portions of the water column not but in the upper or bottom portions of the water column (Figure 20) (Sinninghe Damste et al., 1987, 1993; Shanfa et al., 1989; Dutta et al., 2013; Jiang et al., 2018, 2019). The α-MTTC is the trimethyl MTTC

compound. The β, γ, and ζ MTTCs are isomers of the dimethyl MTTC. In the samples tested δ-MTTC, the monomethyl MTTC, was not detected and therefore not discussed in this study. In the Lower Woodford Shale the MTTCs are low in concentration with some limited variability. They remain low into the lower Middle Woodford Shale and begin to increase in concentration at about 172.42 ft. This rise in concentration continues through the Middle Woodford Shale until there is a drop off at 130.00 ft. The peak concentration during this interval is at 147.08 ft corresponding with the peak concentration of the aromatic carotenoids and the rise in concentration of the nickel porphyrins. In the Upper Woodford Shale, the concentrations are initially low but generally rises through the Upper Woodford Shale reaching the highest concentrations in the late Upper Woodford Shale.

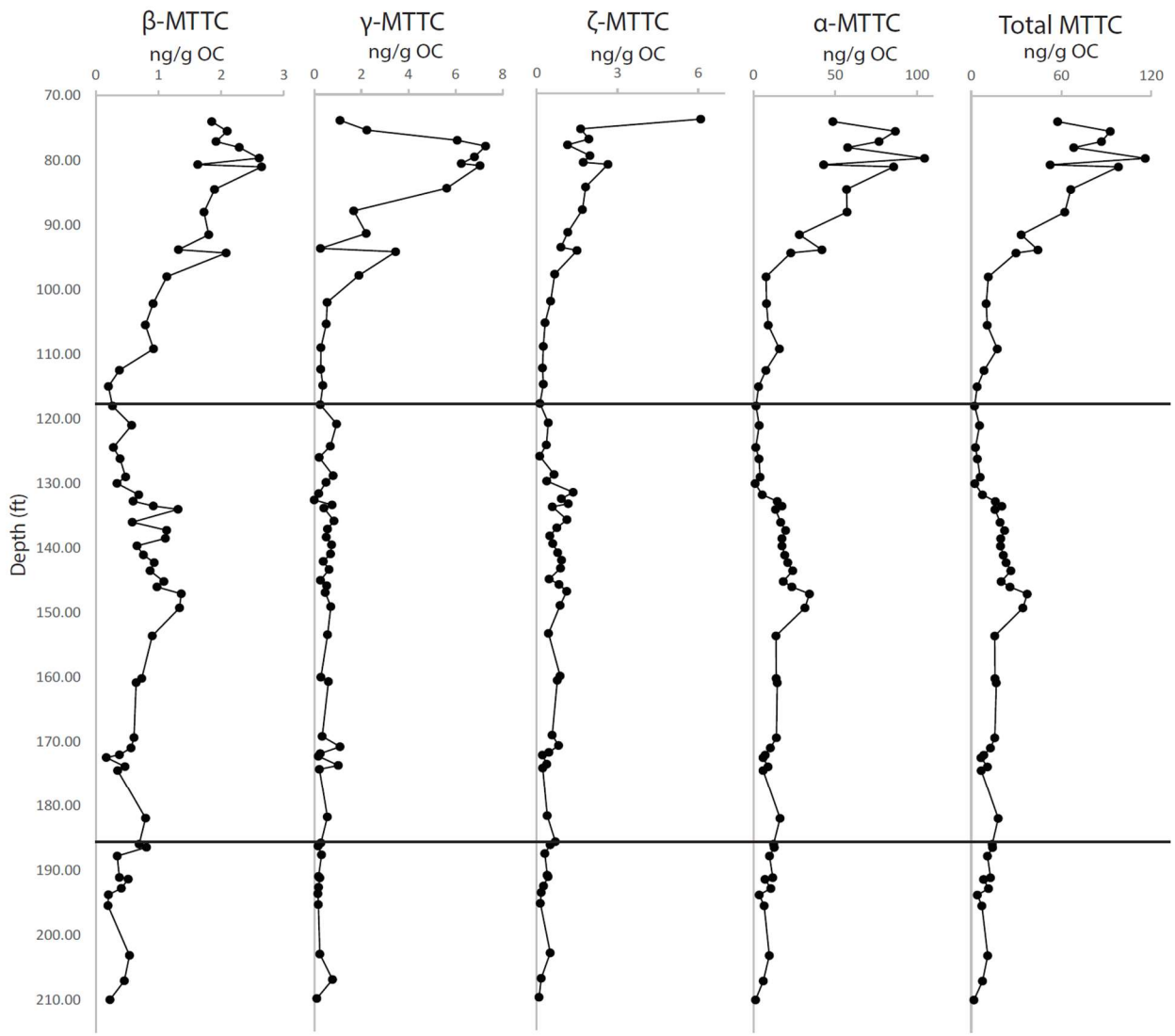

Figure 21. Depth profiles of the MTTC isomers. The line at 118ft divides the Upper Woodford Shale and the Middle Woodford Shale, the line at 185ft divides the Middle Woodford Shale and the Lower Woodford Shale.

3.4 Trimethylphytylbenzoquinone

Trimethylphytylbenzoquinone (TMPBQ Appendix I:**XVII**) is a novel compound tentatively identified by Connock (2021). The chromatogram of TMPBQ (Figure 20) shows three distinct isomer peaks. Their concentrations and depth profiles are shown in figure 22. The TMPBQ is fairly low in the Lower Woodford Shale and sees a slight rise in the Middle Woodford

Shale right after the Lower/Middle Woodford Shale boundary. In the Middle Woodford Shale the concentration begins to increase at 172.00 ft. The concentrations peaks at 147.08 ft and then begin to decrease before becoming undetectable at 131.75 ft. The concentration remains low until the Upper Woodford Shale where concentrations again begin to increase significantly showing limited variability in the Upper Woodford Shale and finally reaching its highest concentration at 75.50 ft. The TMPBQ/α-MTTC ratio has a depth profile very similar to that of the total TMPBQ in the Lower Woodford Shale and Middle Woodford Shale. However, in the Upper Woodford Shale it departs from the similarities showing a spike in the early Upper Woodford Shale reaching its peak at 98.00 ft then decreasing in the late Upper Woodford Shale. This means that the TMPBQ was more prevalent proportionally than the α-MTTC in the early Upper Woodford Shale and returned to similar concentrations in the later Upper Woodford Shale. The TMPBQ isomer ratio is the ratio of the 2^{nd} and 3^{rd} isomers divided by the 1^{st} isomer. This depth profile is missing many points compared to others in this study resulting from when the 1^{st} isomer was not detected. From the available data it is low in the Lower Woodford Shale and then rises in the Middle Woodford Shale peaking at 142.25 ft before decreasing again at 131.75 ft. In the Upper Woodford Shale the ratio remains relatively low with minimal variation.

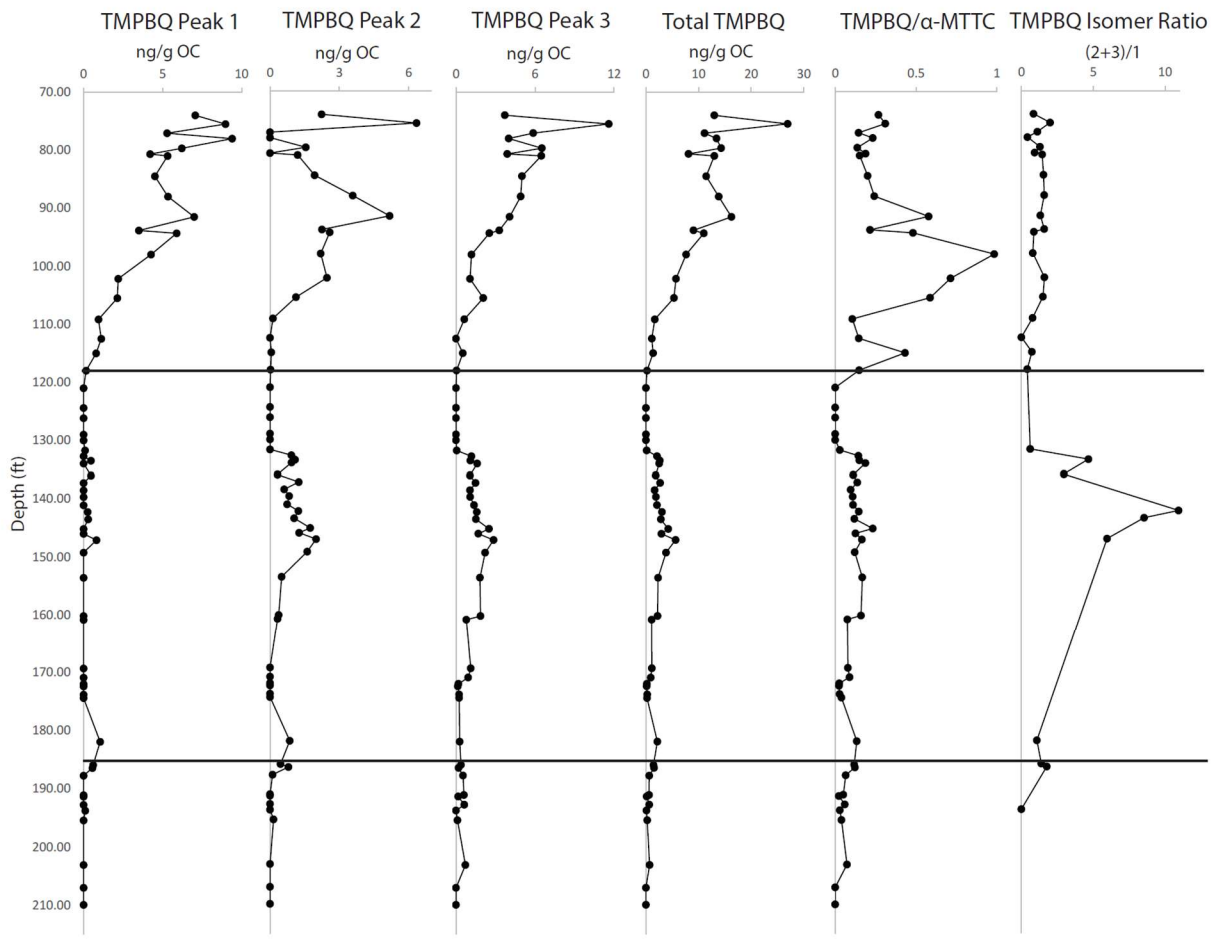

Figure 22. Depth profiles of TMPBQ(**XVII**) isomer peaks. Ratio of the total TMPBQ(**XVII**)/α-MTTC(**XVI**) and the ratio of the 2nd and 3rd isomers divided by the first isomer.

3.5 $\delta^{13}C$ of Organic Carbon

Figure 23 shows the depth profile of the organic carbon isotope composition using the results found in Molinares-Blanco (2019) along with select samples in this study. In figure 23 it shows the depth plot of both Molinares-Blanco (2019) and a plot of Molinares-Blanco (2019) and this study combined. The D/C, F/F, and Kellwasser boundaries are placed according to Molinares-Blanco (2019) which defined the boundaries by comparing their data to the global carbon isotope excursion curve. Molinares-Blanco (2019) determined that there were

excursions around 155 ft, 145 ft, and 85 ft indicating that is where the Hangenberg and Kellwasser events took place. However, the data from this study questions some of these conclusions. In the D/C boundary some of the data points show a much more negative value but then one is very close to the Molinares-Blanco (2019) study. This suggests the D/C boundary should be moved up slightly to fit more with the positive excursion. In the LK and UK the data points just show fluctuations when combined with the Molinares-Blanco (2019) data, alone they would show a similar trend. This data also shows a large positive isotope excursion at 126.17 ft. In the Lower Woodford Shale the data from this study tends to be more positive than the data from Molinares-Blanco (2019), but in the Middle and Upper Woodford Shale the data from this study tends to be more negative.

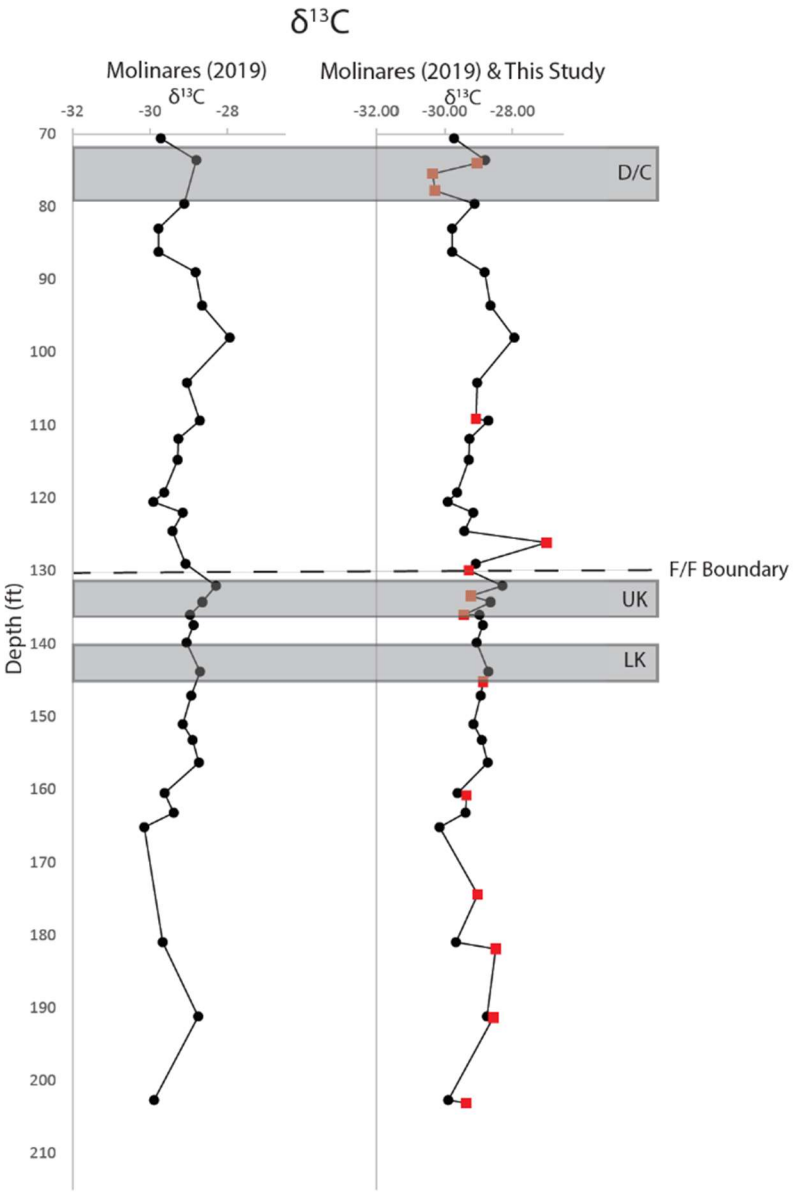

Figure 23. Depth profiles of $\delta^{13}C$ organic carbon. Lower Kellwasser event (LK), Upper Kellwasser event (UK), Frasnian/Famennian Boundary (F/F Boundary), and the Devonian/Carboniferous event (D/C) were all found using Molinares-Blanco (2019) findings and proposals. Red squares indicate samples from this study, black circles are data points from Molinares-Blanco (2019).

CHAPTER IV

4. Discussion

4.1 LCMS vs. GCMS for aromatic carotenoids

All previous studies looking at biomarkers in the Wyche-1 core of the Woodford Shale have been done using GCMS. The analytical window of GCMS is restricted to volatile compounds, such as the non-polar hydrocarbons. However, with LCMS the polar fraction of biomarkers can be well characterized. Extraction and sample preparation methods for GCMS is tedious and takes much more time than LCMS (Connock et al., 2018). Comparatively, the ultra-sonic bath method used in this study for LCMS analysis is quick. On average 8 samples could be processed in approximately 5 hours. The temperature needed to elute the aromatic carotenoids is too high for the GCMS to safely be operated. However, the ultra-sonic bath extraction used in this study also has some drawbacks; it is not as efficient as the Soxhlet extraction Connock et al. (2018) used. Comparing our LCMS results with those obtained by Connock et al. (2018) for isorenieratane(**I**) and paleorenieratane(**II**) helps to determine if the new LCMS methods are a viable alternative to the GCMS methods. The LCMS total yields are several orders of magnitude lower than GCMS yields, although the trends are similar (Figure 24).

Table 9. Results obtained from the LCMS method and the GCMS method *(Connock et al., 2018)*.

Sample	Depth (ft)	Isorenieratane (ng/g OC)	Paleorenieratane (ng/g OC)	Isorenieratane (ng/g OC)	Paleorenieratane (ng/g OC)
		LCMS		GCMS Connock (2018)	
WCH-40	93.83	20.76	36.62	700	1770
WCH-41	109.17	13.14	7.41	970	1080
WCH-42	112.50	8.47	4.24	1080	580
WCH-43	126.17	2.79	8.34	1100	3790
WCH-60	131.75	11.43	35.10	1470	5760
WCH-61	132.75	25.53	120.17	2760	17720
WCH-44	134.00	9.01	30.02	6600	33090
WCH-45	145.17	14.59	67.88	13820	92840
WCH-46	153.58	15.62	50.90	14370	59280
WCH-47	160.17	13.54	37.68	10630	37070
WCH-48	160.83	49.06	117.79	7170	20660
WCH-49	169.33	33.95	80.00	7760	23710
WCH-50	170.92	21.83	46.01	5690	15160
WCH-51	172.00	12.76	20.61	1320	2680
WCH-52	172.42	8.97	6.66	630	970
WCH-53	173.83	16.18	12.83	2090	1760
WCH-54	174.42	5.55	5.09	810	820
WCH-32	181.92	21.15	8.49	880	570
WCH-33	185.92	123.40	66.10	4470	7050
WCH-34	186.42	32.70	15.96	3350	2350
WCH-35	187.75	13.11	12.87	2250	2960
WCH-36	191.08	24.43	35.26	5060	8320
WCH-55	191.33	9.84	8.18	1130	1130
WCH-37	192.75	23.22	24.07	1450	2590
WCH-38	193.75	6.69	4.03	2370	1490
WCH-39	195.42	21.13	16.80	1600	1430
WCH-56	203.08	27.63	21.72	3810	3400
WCH-57	207.00	12.95	9.49	1840	1520
WCH-58	209.92	2.44	2.75	200	120

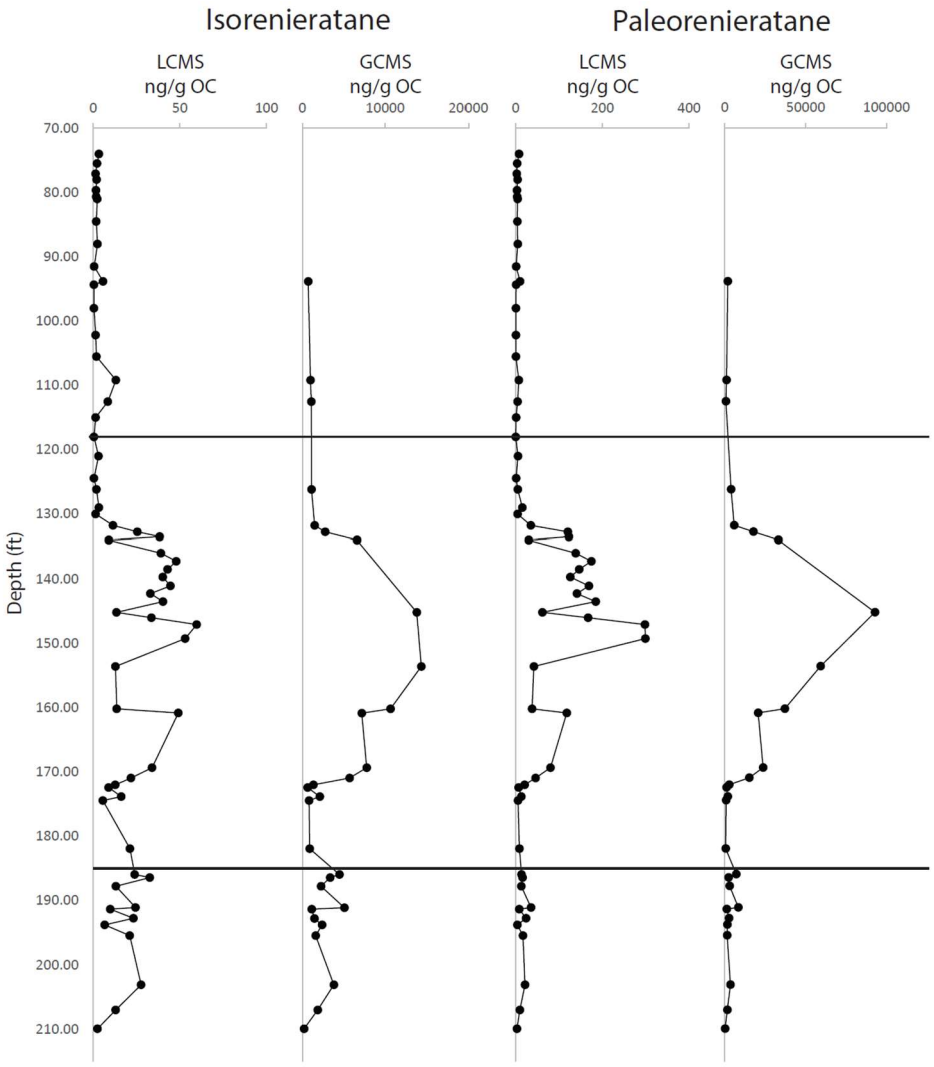

Figure 24. Depth profiles of Isorenieratane(**I**) and Paleorenieratane (**II**) measured on the LCMS and GCMS. GCMS results were obtained from Connock et al. (2018).

Aromatic carotenoids (C40+) are one group of the biomarkers that can be analyzed with both GCMS and LCMS methods. They do not fully elute from the GCMS at 310°C, meaning the samples must be run at higher temperatures, explaining why previous studies do not detect these compounds (Romero and Philp, 2012). In Connock et al. (2018), they run the samples at 315°C, and they speculate that running at even higher temperatures such as 320°C would elute even higher amounts relative to the internal standard. However, these higher temperatures

have the potential to damage the GC capillary column. The GCMS is better suited to measuring volatile compounds that the gas phase can easily carry. Carotenoids are not very volatile, and therefore it is difficult to measure them using GCMS. Under the LCMS setup all aromatic carotenoids are readily detected in the injected TLEs (Appendix III: **I-VI)**, regardless of the complex background signal of the matrix. Each LCMS analysis takes only one hour which is much shorter compared to the two hour program for GCMS.

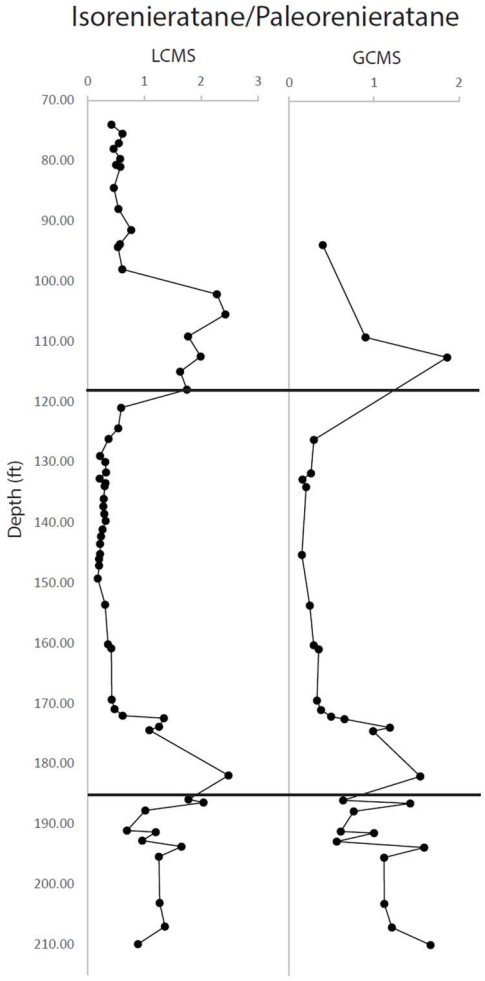

Figure 25. the depth profiles of the Isorenieratane(**I**)/Paleorenieratane(**II**) ratio found on the LCMS and the GCMS. GCMS results were obtained from Connock et al. (2018). The line at 118ft separates the Upper Woodford Shale and the Middle Woodford Shale, the line at 185ft separates the Middle Woodford Shale and the Lower Woodford Shale.

The extraction and detection efficiencies between the two methods are different. This is likely because, for the LCMS procedure, the total lipid extract (TLE) was injected, while for the GCMS, the samples were fractionated first. Injecting the TLE instead of fractionated samples results in a much higher background for the LCMS method. Comparing the results between the GCMS and LCMS methods in figures 24 and 25 shows that the depth profiles appear very similar for each compound and the ratio. However, when looking at the cross plots in figure 26, they do not seem to correlate as well. Isorenieratane(**I**) and paleorenieratane(**II**) show very low R^2 values, indicating their correlation between the LCMS and GCMS methods is low. The cross plot for the isorenieratane/paleorenieratane ratios, however, shows a much stronger correlation. There were four outliers identified (Figure 26) that, if removed, would result in a much higher correlation for isorenieratane and paleorenieratane. These were samples WCH-44, WCH-45, WCH-46, and WCH-47. These outliers showed a much lower relative concentration detected by the LCMS than by the GCMS. It is possible these outliers resulted from the different recovery efficiency of the two lipid extraction methods, which could be related to mineral absorption. The bias could also be a result of a bias in the mass extraction and peak area integration. However, reintegrating with a different mass deviation window provided similar results. Nevertheless, comparing the ratio between isorenieratane and paleorenieratane removed these possible biases. The correlation observed for the carotenoid ratios is strong enough to determine that this new ultrasonic bath extraction and LCMS method is a viable method for biomarker extraction for future experiments.

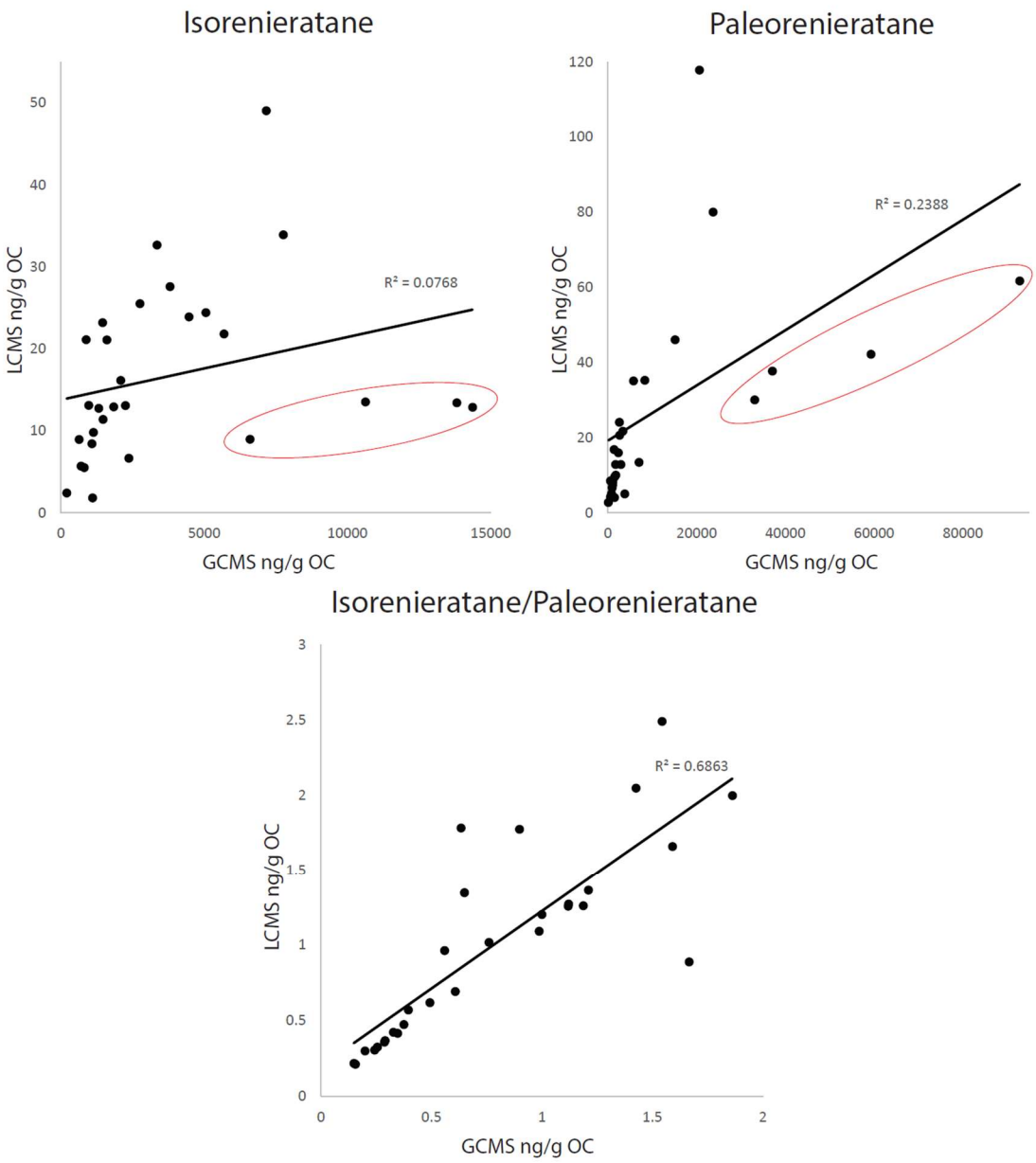

Figure 26. Correlation plots between results obtained from the LCMS and GCMS methods for Isorenieratane(**I**), Paleorenieratane (II) and the Isorenieratane(**I**)/Paleorenieratane (II) ratio. A straight line of best fit was used and the R^2 value was displayed. GCMS results were obtained from Connock et al (2018). The four outliers are circled in red.

4.2 Isorenieratane and Paleorenieratane as biomarkers for PZE

Carotenoids are pigment molecules that are produced by many different photosynthetic organisms. However, C40 aromatic carotenoids are exclusively produced by green (GSB), purple sulfur bacteria (PSB), and cyanobacteria and can therefore be used as a biomarker for photic zone euxinia (PZE) (Brocks and Summons, 2005; Cui et al., 2020). Using C40 aromatic carotenoids as a proxy can provide information about the extent of the PZE. Since light availability, pH, sulfidic concentration, and competition from organisms in the oxic layer impact the growth of PSB/GSB, carotenoid concentrations can also be used to provide some ideas about these as well. This study focuses on the carotenoids produced from the degradation of carotenoids produced by GSB, mainly isorenieratane(**I**) and paleorenieratane (**II**). Since GSB can live in deeper water than PSB, these results will not provide information on the minimal depth of PZE but instead provide a general indication of the presence of PZE (Meyer et al., 2011).

Aromatic carotenoids were detected in varying concentrations throughout the Woodford Shale (Figure 15: Table 2). Of these carotenoids, isorenieratane(**I**) and paleorenieratane (**II**) were detected in the highest concentrations. Other carotenoids derivatives with higher (up to C42) and lower (to C38) methylation level (Cui et al., 2020) were also detected in the samples (Appendix I: **I-VI**). These compounds have potential future applications, but their significance is beyond the scope of this study. Isorenieratane(**I**) and paleorenieratane (**II**) seem to parallel each other in the samples, which may indicate that they come from similar sources. Paleorenieratane (**II**) currently does not have a known modern source; the most recent sediments where it is detected occur in the Mesozoic. However,

because of the similarity in abundance to isorenieratane(**I**), it is assumed to be produced by a now extinct GSB (Spaak et al., 2018).

Isorenieratane(**I**) is produced by the brown strain of GSB (bGSB), which can live in low light conditions owing to their special light-harvesting organelle, the chlorosome. They are efficient sulfide oxidizers in low light conditions with the ability to survive with light as low as 20 lux (Biebl and Pfennig, 1978). They also have more light-harvesting pigments than other strains of GSB or PSB, resulting in them having concentrations of these molecules 175% higher than these other strains (Overmann et al., 1992). As a result of the low light conditions, bGSB have an increased number of photosynthetic units. In their chlorosomes, bGSB contains 5000-8000 BChl c molecules/reaction centers (Frigaard et al., 2003). They also require lower concentrations of CO_2 to survive at 3.5-4.5 mol quanta/mol CO_2 (Brune, 1989). Due to the positive linear increase of both paleorenieratane(**II**) and isorenieratane(**I**), it is likely that the producers of each molecule have little resource competition with each other or they are produced by the same source organisms. Since isorenieratane(**I**) can absorb lower wavelengths of light (460nm) within the wavelength of the deepest penetrating daylight wavelengths 450-470nm, it is most likely that the organism that produced paleorenieratane(**II**) lived at a shallower depth than the bGSB producing isorenieratane(**I**) (Connock, 2015). The GSB living in natural environments has both planktonic and microbial mat forming species. So, the occurrence of isorenieratane can be a signal of microbial mats in shallow water, not necessarily PZE. When GSB is inferred to live in algal mats, there is also the presence of wavy laminations in the rock (French et al., 2014). However, in the Woodford Shale, the only lithofacies with wavy laminations are in the Upper Woodford Shale (Molinares-Blanco, 2013), where the

concentrations of these carotenoids are at their lowest. It is assumed that GSB in the Woodford Shale lived as a planktonic community and not as benthic algal mats (Connock et al., 2018).

Isorenieratane(**I**) and paleorenieratane(**II**) in the Wyche-1 core show very similar trends, with paleorenieratane(**II**) being about three times more abundant than isorenieratane(**I**). They are both present in the Lower Woodford Shale, showing a few excursions in concentration and begin a significant increase in concentration during the Middle Woodford Shale. Their increase in the Middle Woodford Shale begins in the Wyche-1 core at about 172 ft. Their concentration increases and then begins to fall before becoming almost negligent at around 130 ft which is at the MFS according to Turner et al. (2015, 2016). Isorenieratane(**I**) reaches a maximum of 59.70 ng/g OC at 147.08 ft, and paleorenieratane(**II**) reaches its maximum of 299.00 ng/g OC at 149.25 ft. After the MFS, the carotenoid concentrations drop to relatively low concentrations, with only a small spike in the Upper Woodford Shale. The decrease in the concentration of carotenoids corresponds to a change in lithology. Utilizing the lithology determined by Molinares et al. (2013) (Figure 16), in the Lower Woodford Shale and Middle Woodford Shale, the main lithology is mixed siliceous/argillaceous mudstone with thin clay laminations (G) corresponding to an overall 2nd order TST. There are some places where this is not the case, like the argillaceous siltstone with abundant angular detrital quartz (H) at 180ft, but it mostly remains true. Around the peak of the isorenieratane(**I**) and paleorenieratane(**II**) concentrations in the Middle Woodford Shale, there is a lithology change; it changes to black to dark gray laminated argillaceous mudstone (F1-F2). During this lithology change, the concentration of carotenoids begins to decrease until finally, at 130ft, they all but disappear, which corresponds to a massive transgressive hemicycle. Based on the peaks of isorenieratane(**I**) and

paleorenieratane(**II**) in the Lower Woodford Shale, episodic PZE can be inferred. These episodic PZEs take place after a regressive hemicycle during a small transgressive hemicycle.

4.3 Unexpected Metalloporphyrin Distribution

Porphyrins are the degradation products of chlorophyll and bacteriochlorophylls (Huseby et al., 1996; David, 1998; Stuart Walker and Keely, 2004; Junium et al., 2008, 2015). It is believed that grazing by herbivorous invertebrates begins the process of producing porphyrins from these tetrapyrroles (Junium et al., 2008). This is supported by the isolation of porphyrins from fecal pellets of benthic macroinvertebrates (Goericke et al., 2000). The BiCAP structure is produced from the cyclization of the C-17 propionic acid substituent (Chicarelli et al., 1984; Junium et al., 2008). The DPEP is produced by chlorophyll losing the Mg, phytol, and the carbomethoxy moiety; it then undergoes keto reduction/dehydration/reduction; and is finally decarboxylated resulting in DPEP (Louda et al., 2000, 2011; Fulton et al., 2018). The ETIO is then produced by the oxidative cleavage of the isocyclic ring in immature sediments (Baker and Louda, 1983; Barwise and Roberts, 1984; Louda et al., 2011). It has been established that DPEP thermally degrades to ETIO allowing DPEP and ETIO to be used as a maturity parameter for the hydrocarbons present in the sediment (Barwise and Roberts, 1984; Huseby et al., 1996; Louda et al., 2000, 2011; Marín et al., 2014). These porphyrins also produce metallic complexes; in this study, vanadyl (VO^{2+}) and nickel (Ni^{2+}) were observed. These metalloporphyrins are produced diagenetically after sedimentation but show promise for providing information about the redox state of the environment of deposition (Lewan and Maynard, 1982; Lewan, 1984).

Thermal maturity parameters are important when determining the amount of diagenesis that has occurred in a system. It is also crucial to know what type and the quality of hydrocarbons that will be produced. Using the porphyrins DPEP and ETIO, the thermal maturity can be determined by the ratio of porphyrins. The DPEP/ETIO ratio will decrease along with the decrease in the average molecular weight of porphyrins with increasing thermal maturity (Huseby et al., 1996; Grosjean et al., 2004; Marín et al., 2014). Figure 27 shows that the DPEP/ETIO ratio is highly variable in the Lower and Middle Woodford Shale. The ratio severely decreases between 149.25ft and 133.5ft, corresponding to the decrease in carotenoid concentration from its peak and a transgression beginning. The ratio then increases again and becomes variable before decreasing again in the Upper Woodford Shale. In general, the ratio decreases from the Lower to the Upper Woodford Shale, which would indicate that the Upper Woodford Shale is more thermally mature than the Lower Woodford Shale. If this ratio indicates thermal maturity for these samples, then there was also an increase in thermal maturity during the sustained PZE. Connock et al. (2018) found the thermal maturity of the Woodford Shale in the Wyche-1 core to be thermally immature with T_{max} values ranging from 410°C-428°C. It also shows a trend of becoming more thermally mature from the Lower Woodford Shale to the Upper Woodford Shale. Combining these previous findings with the DPEP/ETIO ratio observed in this study shows a general trend towards being more mature from the Lower to the Upper Woodford Shale. Connock et al. (2018) did observe an increase in maturity between 149.25ft and 133.5ft, although not as significant as is seen in the DPEP/ETIO ratio. This could be due to the limited samples that were taken between these depths making the changes less obvious. Between these depths is the onset of the continuous PZE, which

would have resulted in increased preservation potential of organic matter. With enhanced OM preservation, we would expect to see less DPEP being degraded to ETIO, but instead, there is an increase in the concentration of ETIO relative to DPEP. This could be caused by a preferential degradation of DPEPs between these depths. Since the Woodford Shale is relatively shallowly buried, the thermal maturity is inconsequential. Since the entire core is thermally immature, the minor deviations of perceived maturity matter less. It is promising that the previously found T_{max} trend supports the DPEP/ETIO ratio trend. This shows that this ratio can also be used to determine thermal maturity information for more thermally mature cores.

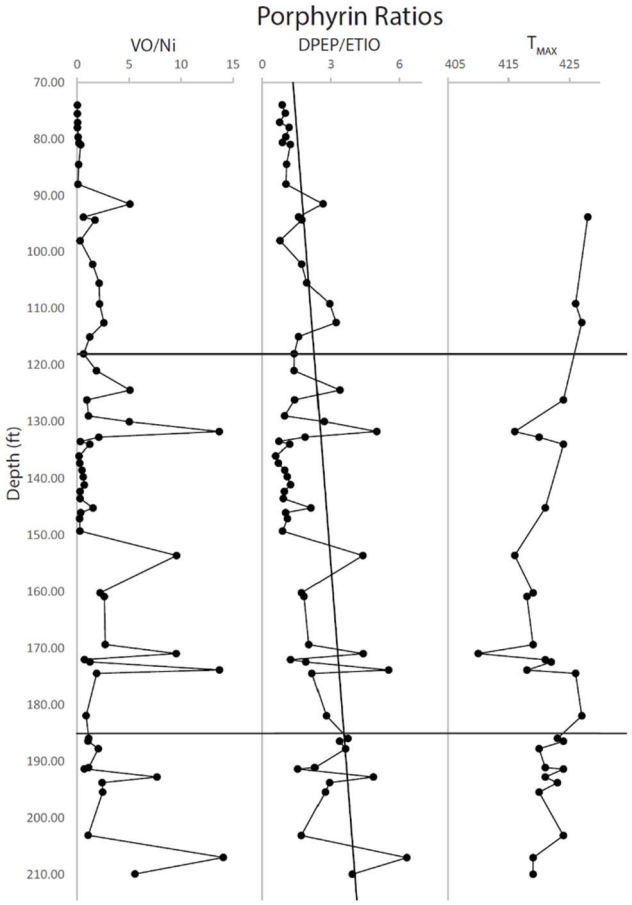

Figure 27. Depth profile of the VO/Ni ratio where the total VO porphyrins are divided by the total Ni porphyrins. Depth profile of the DPEP/ETIO ratio where total DPEP is divided by total ETIO. Depth profile of T_{MAX} found by Connock et al. (2018). The trend line on the DPEP/ETIO ratio shows a general decrease indicating an increase in thermal maturity.

Metalloporphyrins can be used as an indicator of redox potential in the water column during deposition. The metalloporphyrins are produced during early diagenesis and rely on the availability of metals in the surrounding sediments to produce the metal complexes (Huseby et al., 1996; Junium et al., 2008, 2015). In this study, two metallic complexes were examined, vanadyl (VO^{2+}) and nickel (Ni^{2+}) porphyrins. The ratio observed of the sum of these two metalloporphyrins to each other should indicate relative Eh/pH conditions present at deposition. In highly reducing conditions, vanadyl porphyrins should be the dominant member, while nickel porphyrins should be low. This results because in marine environments where reducing conditions and sulfide is present, nickel will be removed from the system by the precipitation of nickel sulfides. Since these nickel sulfides are removed from the system, vanadyl complexes with porphyrin are favored. In more oxidative environments, an increase in the nickel porphyrins would be expected to be seen relative to the vanadyl complexes since the nickel is not removed by sulfide. When nickel is not removed by sulfide, it leaves both nickel and vanadyl ions in solution, which compete for chelation with free base porphyrins. The nickel ions dominate this competition due to the higher equilibrium constant of formation of nickel porphyrins compared to that of vanadyl porphyrins and the higher Eh associated with a more oxidative environment (Moldowan et al., 1985; Chen and Philp, 1991). The VO porphyrin/Ni porphyrin ratio can be seen in figure 27, where a higher ratio number indicates a more reducing environment. The ratio shows variation in the Lower Woodford Shale, which is expected as there were episodic reducing conditions during this deposition. There is also some variation in the lower parts of the Middle Woodford Shale until it reaches 149.25ft when it drops and remains low until 133.5ft. This mirrors the pattern that was seen in figure 27 with the

DPEP/ETIO ratio and is a result of the anomalous excursion of Ni porphyrins. Above 133.5ft, it has some more variation before reaching the Upper Woodford Shale, where it decreases again, indicating a more oxygenated environment. If the VO/Ni porphyrin ratio shows the redox conditions, the low numbers between 149.25 and 133.5ft are perplexing. The presence of isorenieratane(**I**) and paleorenieratane(**II**) at these depths indicates sustained euxinic conditions in the paleoenvironment during the time of deposition. Since that is the case, it would be expected that the VO/Ni porphyrin ratio should be high here, with the VO complexes significantly outnumbering the Ni complexes.

Both the DPEP/ETIO and the VO/Ni ratios have low numbers between 149.25ft and 133.5ft. It does not correspond with the onset of the PZE indicated by the carotenoids but instead corresponds more closely to the peak and then decline of the carotenoids. The low numbers in both ratios are a result of high concentrations of Ni-ETIOs at these depths. Ni-DPEP has very similar concentrations to Ni-ETIO, both of which are much higher than their respective VO concentrations. This results in the low ratios seen between these depths. Looking back to figure 16, there seem to be two correlations to the onset of the nickel porphyrin excursion, a lithology change, and a general transgression. The change in lithology shows less of a correlation to the excursion of nickel porphyrins since it comes after the excursion begins. The change in lithology also does not correlate to the small spike in the Lower Woodford Shale of nickel porphyrins that occurs right before the Lower/Middle Woodford Shale boundary. Prior to the excursion of nickel porphyrins, the Middle Woodford Shale generally exhibits a regression during which the nickel porphyrins remain relatively low. Then, around the beginning at the transgression later in the Middle Woodford Shale, their concentration increases significantly.

The small regression between 140ft and 135ft corresponds to a dip in nickel porphyrins before increasing during the following transgression. In the Lower Woodford Shale, the small excursion before the Lower/Middle Woodford Shale boundary also corresponds to a transgression, but here the VO species also increases in concentration, which could indicate enhanced productivity or preservation. A possible explanation for this could be the presence of GSB in this reducing environment. With enough sulfur-reducing bacteria present, the sulfide concentration in the water might be reduced enough to prevent nickel sulfide from being formed in large enough quantities to cause a drop in nickel porphyrin production, an explanation also proposed by (Eckardt et al., 1991). However, a problem with this idea is that the isorenieratane and paleorenieratane concentrations are decreasing through this area, meaning GSB are in decline.

There seems to be a bias in the formation of VO and Ni porphyrins, which could skew the ratio data. Overall, there is a strong preference for Ni to be chelated to ETIO compared to BiCAP but a strong preference for VO BiCAP to be formed compared to VO-ETIO. This bias can be seen in figure 28, which shows the relative percentages of each porphyrin compared to the total. The Middle Woodford Shale shows even a more substantial bias between the BiCAP and ETIO nickel percentages, with Ni-BiCAP being undetectable in some samples. The distribution of porphyrins based on VO and Ni being different suggests that the diagenesis that occurred to exchange the metal center took place in different conditions or at a different time for each metal. Since ETIO is a degradation product of DPEP, it could be that the VO product is produced earlier in diagenesis than the Ni product. This, however, does not provide an answer as to why the Middle Woodford Shale has such a strong bias with respect to the nickel constituents (Figure 19 & 27). Returning to the previously mentioned correlation of transgressions and the

excursion of nickel porphyrins (Figure 16 & 19), it could be that the transgression brought terrigenous sourced nickel into the system. This explains the high nickel abundance but not its preferred chelation to ETIO vs DPEP and BiCAP. Alternatively, nickel-containing fluids could have permeated the sediment providing nickel to the later diagenetic porphyrin product. Turner et al. (2015) did not test for nickel as a trace metal so this remains speculative. Fluids produced in the Upper Woodford Shale would contain more available nickel as the Upper Woodford Shale is more oxygenated and does not contain PZE, which would limit the nickel. These fluids permeating the sediment would encounter more ETIO as there would have been time for the degradation of BiCAP and DPEP to ETIO to occur. This idea, however, does not explain the bias seen in the Upper Woodford Shale for Ni-ETIO.

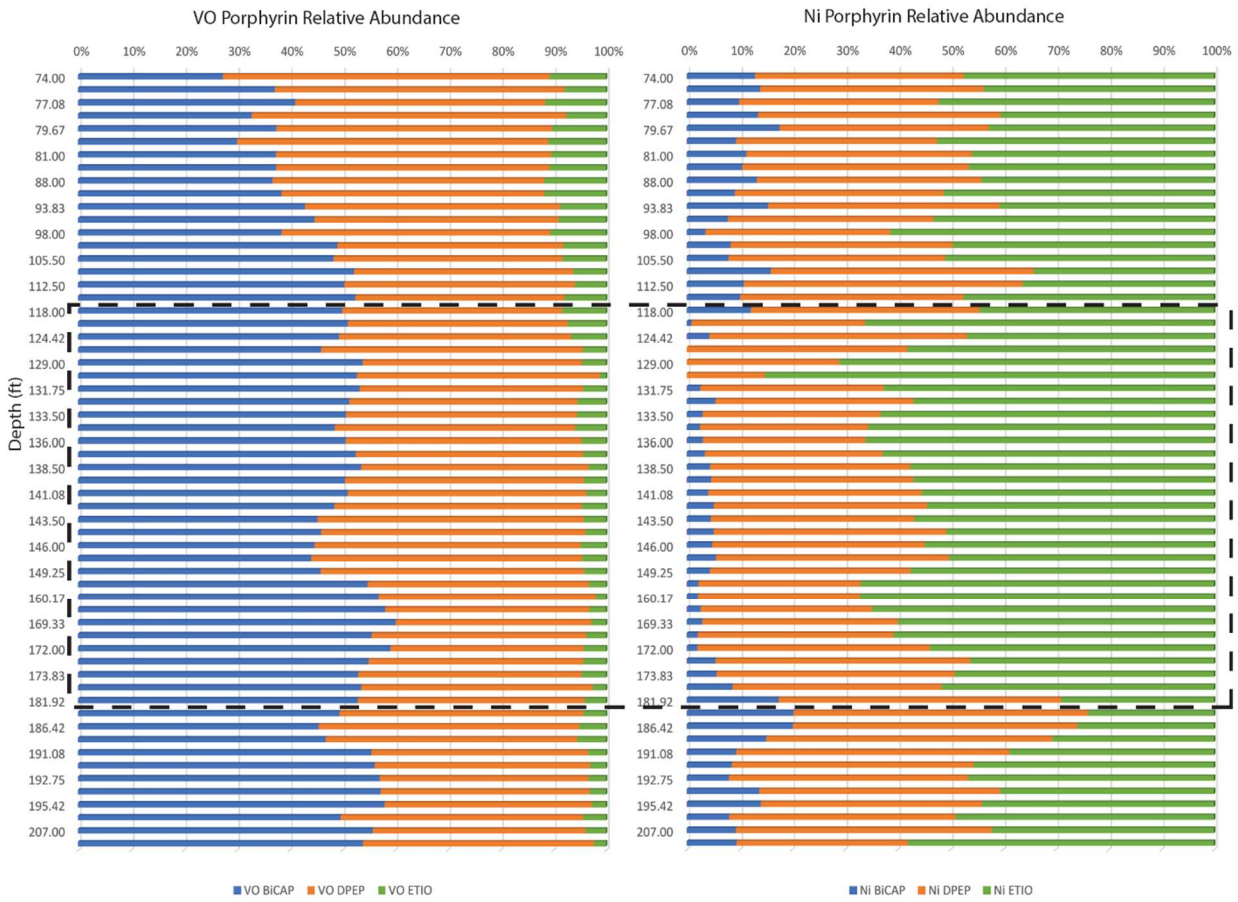

Figure 28. Relative abundance of BiCAP, DPEP, and ETIO for all the VO porphyrins and all the Ni Porphyrins. The dashed box surrounds the Middle Woodford Shale.

With a limited free porphyrin pool, implied by the absence of free porphyrin in all analyzed shales, there could be a bias in the formation of VO and Ni BiCAP and ETIO determined merely by the chemical features of BiCAP and ETIO. The VO has a smaller ionic radii at 0.63 angstroms than Ni at 0.69 angstroms (Lewan and Maynard, 1982); the smaller size might be favored in the BiCAP structure as opposed to the ETIO structures. The VO being a molecule, has a highly negative oxygen, which means that the overall positive charge could be more shielded than a single Ni atom. The extra E and F ring structures on BiCAP (Figure 29)

could mean the electrons are not drawn away from the binding nitrogen as strongly, and therefore BiCAP can hold onto VO better. Conversely, ETIO has hydrogens in place of these ring structures providing a slight positive charge which would draw the negative charge from the nitrogen's; this would require a metal with less electron shielding to form a strong bond with ETIO.

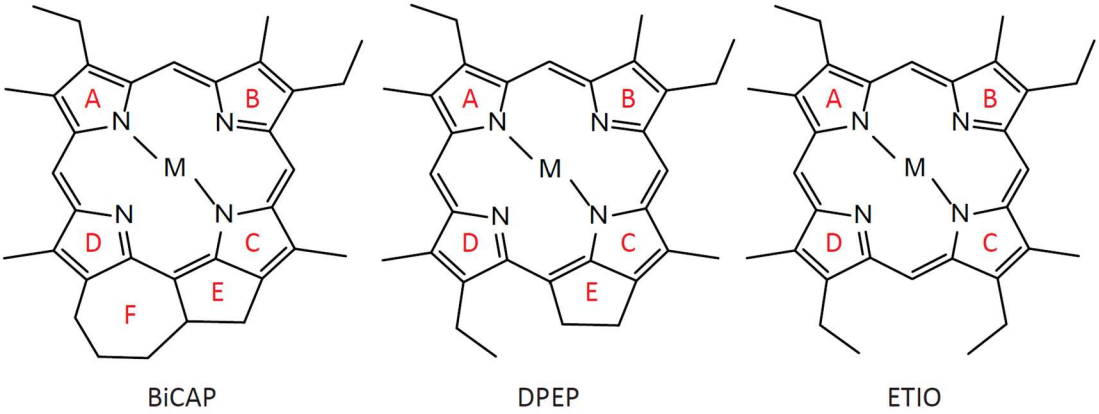

Figure 29. The ring configurations in BiCAP, DPEP, and ETIO. The red letters delineate each ring. In addition to the A,B,C, and D rings BiCAP has both an E and F ring, DPEP only the E ring, and ETIO has neither of the extra ring structures.

There is also the possibility that this bias results from structural differences and preferences. The Ni(II) ions have a very strong preference for square-planar binding with the Ni atom in the plane of the four porphyrin N atoms (Kim et al., 1996). However, vanadyl complexes have a five-coordinate square-pyramidal geometry, with the V atom sitting above the plane of the four porphyrin N atoms and the O atom bound in the axial position (Drew et al., 1984; Zhang et al., 2019). Since ETIO is the least constrained in its ring movement, it can adopt a conformation in which the N atoms form a perfect square-planar coordination environment for the Ni. Due to the increased rigidity from the extra ring structures BiCAP and

DPEP, these structures might now be able to adopt such a geometry, leading to some puckering of the porphyrin ring and a non-ideal arrangement for Ni. Since VO does not sit in the porphyrin plane, it might be less constrained to coordinating to a porphyrin that can easily adopt the square-planar arrangement and more able to coordinate to porphyrin with a less than perfect arrangement. Bias between VO and Ni DPEP and ETIO have been reported in other studies. Qian et al. (2010) reported that ETIO is favored relative to DPEP when in a nickel complex. Conversely, DPEP is favored relative to EITO in vanadyl complexes. This bias could also be explained by the fact that this study used a new method to detect and quantify these compounds. It could be that this new method somehow selected for Ni-ETIO, most likely during the extraction process and not in the detection.

In the Upper Woodford Shale, the vanadyl porphyrins peak at 91.5 ft before falling off and being replaced by a strong nickel porphyrin presence. The strong signal of vanadyl porphyrins in the Upper Woodford Shale could result from excess vanadium present in the sediments. Figure 8 shows the bulk geochemistry of the Wyche-1 core found by Turner et al. (2015), and it shows that the concentration of vanadium in the sediment significantly increases in the Upper Woodford Shale compared to the Middle Woodford Shale and Lower Woodford Shale. This significant increase in available vanadium could contribute to the spike in vanadyl porphyrins seen in the Upper Woodford Shale.

4.4 Trimethylphytylbenzoquinone and MTTC

Trimethylphytylbenzoquinone (TMPBQ(Appendix I: **XXXV**)) has been tentatively identified in a recent study (Connock, 2021). Its presence has tentatively been linked with primary productivity, enhanced preservation, and PZE/anoxia in Cretaceous Black Shales. The TMPBQ has three isomers labeled as 1, 2, and 3 in Figure 20. The TMPBQ can be biosynthesized in photosynthetic organisms such as plants, phytoplankton, and some cyanobacteria as one of the steps in producing α-tocopherol (Figure 30). Tocopherols are lipophilic antioxidants and are part of the vitamin- E family. Tocopherol synthesis increases in response to environmental stresses, including high-intensity light, high salinity, heavy metals, and chilling (Lushchak and Semchuk, 2012). The primary purpose of tocopherol in photosynthetic organisms is the scavenging of lipid peroxy radicals and quenching singlet oxygen. Since TMPBQ is part of the tocopherol quinone-recycling system (Figure 30), its presence is likely an environmental stress indicator. Its presence in the Upper Woodford Shale could be an indicator of specifically oxygenation, resulting from the reaction of anoxic phototrophs to higher mixing of oxygenated waters. Based on figure 22, looking at the total TMPBQ, using it to indicate oxygenation indicates that the Upper Woodford Shale is much more highly oxygenated which is also indicated by the lack of aromatic carotenoids present. As a result of being produced by phytoplankton and cyanobacteria, it would have low concentrations in euxinic waters like in the Lower Woodford Shale and Middle Woodford Shale and high concentrations in oxic waters like in the Upper Woodford Shale. However, in the Middle Woodford Shale and Lower Woodford Shale, it shows a similar depth profile to the concentration of isorenieratane(**I**) and paleorenieratane (**II**) (Figure 13). It shows an increase in concentration at a similar depth to

these two aromatic carotenoids, peaks at around the same point, then decreases and is no longer detected around the same depth. In the Middle Woodford Shale and Lower Woodford Shale, it might be an indicator of intense light; this would be caused by the shallowing of the chemocline forcing the algae that produce more α-tocopherol to quench radicals. Alternatively, the increase correlating to the aromatic carotenoids could also result from the increased preservation potential of organic matter from sustained euxinic conditions.

The TMPBQ correlates strongly through the entire Woodford Shale section with α-MTTC (Figure 31), likely indicating the similarity in depth profile to isorenieratane(**I**) and paleorenieratane(**II**) to be coincidental. The α-MTTC(**XVI**) structurally resembles α-tocopherol, with the only difference being that the hydroxyl group at position 6 on the ring is replaced with hydrogen (Shanfa et al., 1989; Dutta et al., 2013). The strong correlation and similar structures could indicate that MTTC and TMPBQ come from the same source in the Woodford Shale (Figure 31). The TMPBQ/α-MTTC ratio (Figure 22) shows a similar depth profile to the total TMPBQ in the Lower Woodford Shale and Middle Woodford Shale. The similarities end in the Upper Woodford Shale; the ratio shows a peak in the early Upper Woodford Shale, while TMPBQ has its peak in the late Upper Woodford Shale. The earlier peak in the ratio indicates that there is relatively more TMPBQ than α-MTTC here. It is possible that α-MTTC is a degradation product of TMPBQ. In this ratio, looking at the structures of each (Appendix I: **XVI**, **XVII**), the remarkable similarities between the two are evident. If this is the case the TMPBQ/α-MTTC ratio would indicate the amount of diagenetic alteration that had occurred. This would mean that while productivity was increasing in the oxygenated environment of the Upper Woodford Shale, diagenetic alteration is low in the early Upper Woodford Shale, not increasing

until the later Upper Woodford Shale. Comparing the TMPBQ isomer ratio (Figure 22) to other proxies analyzed in this study, the depth profile is similar to the aromatic carotenoids. This could mean that it might be able to elucidate the redox conditions at the time of deposition. However, this is tentative as many data points for this ratio are missing due to some samples not having detectable amounts of the first isomer peak. The peak ratio is calculated by adding the 2nd and 3rd peaks then dividing them by the 1st peak. In anoxic conditions, the ratio should be large, and in oxic conditions, the ratio should be small. It shows that the Upper Woodford Shale is oxic while the Middle Woodford Shale is anoxic, fitting with the data from the aromatic carotenoids (Figure 15).

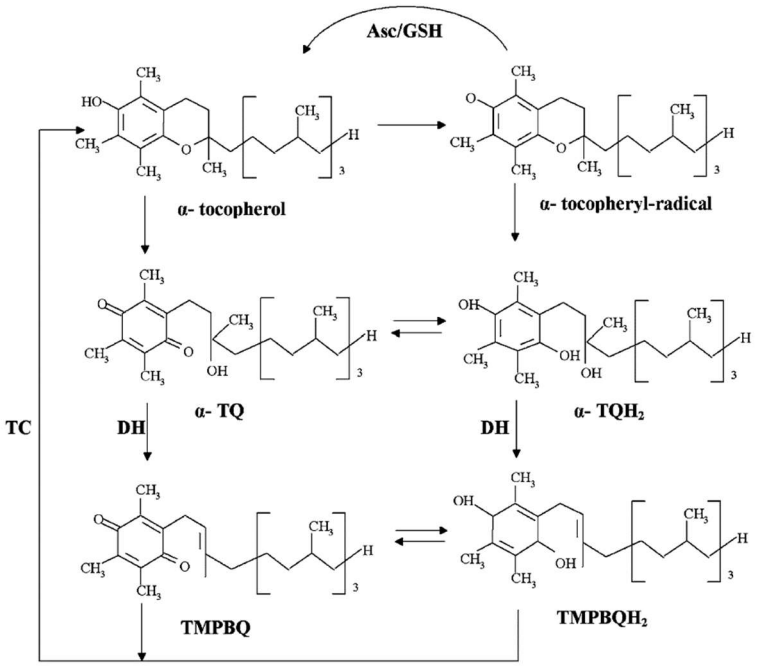

Figure 30. The tocopherol quinone-recycling system, α-TQ = α-tocopherol quinone, α-TQH_2 = α-tocopherol quinol, $TMPBQH_2$ = 2,3,5-trimethyl-6-phytyl-1,4-benzoquinol, TC = tocopherol cyclase, DH = unknown dehydratase, Asc/GSH = ascorbate-glutathione cycle. (Lushchak and Semchuk, 2012)

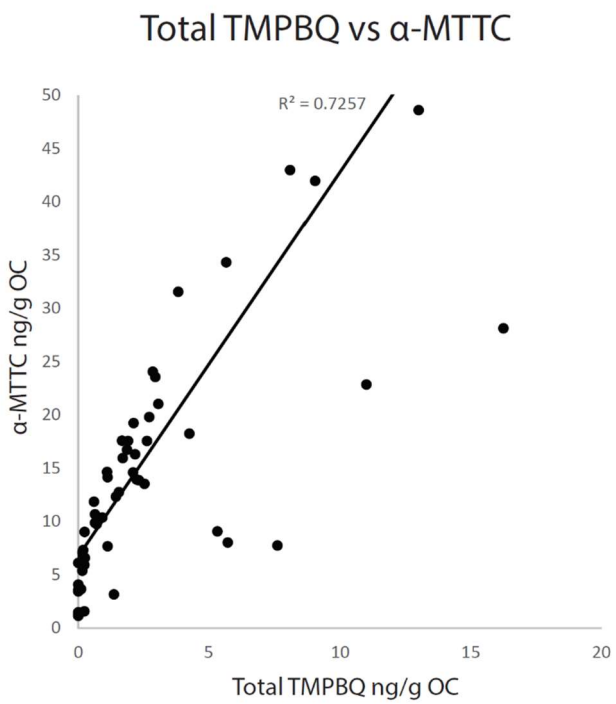

Figure 31. a correlation plot of total TMPBQ(**XVII**) and α-MTTC(**XVI**). There is a straight line of best fit with an R^2 of 0.7257.

Since δ-MTTC was not detected in any samples, it is excluded from this study; this also means that the salinity proxy α/δ-MTTC proposed by Jiang et al. (2018 and 2019) is not applicable to this study. The MTTCI ratio was determined to be an indicator of paleosalinity in previous studies (Peters et al., 2005; Jiang et al., 2018, 2019) when it was correlated to the pristane/phytane ratio and the gammacerane index indicating saline environments. Based on the MTTCI ratio, α-MTTC/total MTTCs, a general salinity profile can be established. Therefore, the ratio will be used more to show salinity changes rather than previously established cutoffs for salinity conditions by Jiang et al. (2018, 2019). Figure 32 shows how the MTTCI ratio (α-MTTC/total MTTCs) and, therefore, the salinity of the system has changed. Based on the hypothesis that a low ratio shows higher salinity conditions and a high ratio shows lower salinity conditions, most of the Lower Woodford Shale and Middle Woodford Shale show lower

salinity. This general low salinity continues until after 132.75ft, where there is a spike in salinity which stays high until the Upper Woodford Shale, where there is variable salinity seeing one large spike but mostly staying around the salinity seen in the Lower Woodford Shale and Upper Woodford Shale.

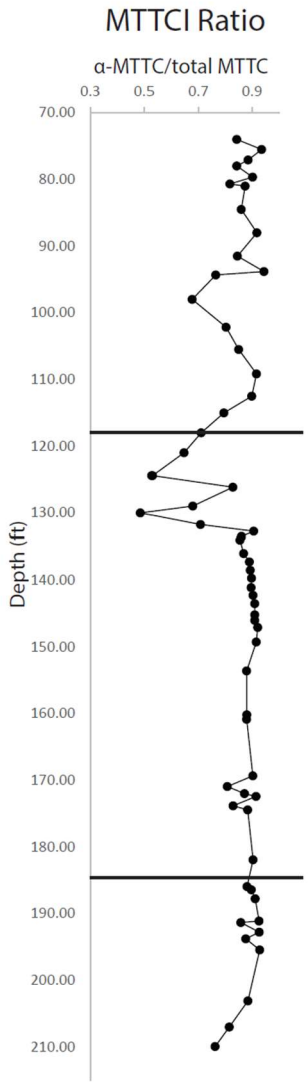

Figure 32. MTTCI ratio (α-MTTC/total MTTC) depth profile. The line at 118ft separates the Upper Woodford Shale and the Middle Woodford Shale, the line at 185ft separates the Middle Woodford Shale and the Lower Woodford Shale.

4.5 Locating the Frasnian-Famennian Boundary

The Frasnian-Famennian boundary has been placed differently in the Woodford Shale, depending on the methods used to find it (Over, 1990; Jones, 2017; Molinares-Blanco, 2019). Biomarker records are more likely to reflect regional environmental changes rather than global, so it is more difficult to correlate the findings with other known event beds. Carbon isotopes, however, will generally record disturbance of global carbon cycles.

Conodont assemblages have been historically used to define the F/F boundary since they are thought to be the teeth of jawless fish and, therefore, would be subject to extinction events (Over, 1990, 2002). They are also locally abundant and diverse in the Woodford Shale, which allows them to be used as a marker for events. Therefore, using conodont zonation can make it possible to assess global paleoenvironmental changes and correlate extinction events between stratigraphic sections (Wignall et al., 1996). Using conodonts, the F/F boundary in the Woodford Shale is defined by the disappearance of *Ancryognathus tslensl, Icriodus symmetricus, Ancryodella lobata, Palmatolepis kireevae, Palmatolepis ljaschenkoae, Palmatolepis proversa, Palmatolepis punctata,* and *Palmatolepis praetriangularis* and the appearance of *Palmatolepis lingullformis, Palmatolepis del. dellcatula, Palmatolepis subperlobata, Palmatolepis triangularls, and Palmatolepis del. clarkl* (Over, 1990). Based on conodont zonation, Over (1990) placed the F/F boundary within the lower 65.6 ft of the Woodford Shale in the outcrops they used. Since conodonts have not been analyzed in the Wyche-1 core, it is impossible to know if this fits with this core. Likely, it does not, but looking at 65.6 ft from the bottom of the core puts it around 145 ft which is reasonably close to other hypotheses for its location.

One of the other ways the F/F boundary is found is through the use of biomarkers. Using biomarkers that have been found to indicate the boundary, the location of the events can be determined. Previous studies have utilized the hydrogen index, pristine/phytane ratio, and aryl isoprenoid ratio to determine the placement of the UK and LK events that predate the F/F boundary (Hartkopf-Fröder et al., 2007). Others have used terrestrial input markers to define these events (Jones, 2017). These methods can be subject to some uncertainty. In Jones (2017), the Kellwasser and F/F boundary are both placed after the maximum flooding surface, a conclusion which is interesting since most other studies place it before. Jones (2017) used biomarkers derived from terrestrial sources to make her determination. Using these biomarkers could be viable since it is thought that the events are characterized by enhanced terrestrial input resulting from widespread fires. In addition, the use of these markers might explain why they found the Kellwasser events to occur after the MFS, as the subsequent falling of sea level could have resulted in the enhanced runoff detected.

The carbon isotope ratio is widely used to determine the locations of the F/F boundary owing to the strong positive carbon isotope excursion that is seen globally at the Kellwasser events (Chen et al., 2005; De Vleeschouwer et al., 2013; Molinares-Blanco, 2019). The carbon isotope ratios (Figure 23) show possible disagreement between this study and the Molinares-Blanco (2019) study. They placed the boundaries based on the global carbon isotope excursion graph, which shows that the LK and UK, along with the D/C boundaries, have positive carbon isotope excursions. Their data lines up nicely with the disappearance of the aromatic carotenoids and the MFS at around 130 ft, making a solid case for this being correct. However, when our data is included, the large positive excursion at 126.17 ft throws their conclusions into question. Using the global carbon isotope excursion would mean the LK and UK would shift upwards to shallower depths and would

also mean the LK does not have a strong positive excursion associated with it in this core. It could also be that the local carbon isotope excursion is different from the global average excursions. Overall, there does not seem to be enough evidence to definitively shift the events and F/F boundary without more isotope data being collected.

Overall, the F/F boundary is difficult to define and can change based on the metrics used to locate it. However, the most likely location for the F/F boundary in the Wyche-1 Woodford Shale core is probably around 130 ft. This conclusion is reached based on a couple of avenues of reasoning. Firstly, the isotope ratios, based on previous work, the F/F boundary is placed around 130 ft in the core. Although our data seems to disagree with this assessment, only a few depths were run, and since the analysis setups were different in different labs, there could be some disagreement with the results, which is why the discrepancies are seen. Without fully running our samples, a definitive location based on isotopes from our samples cannot be made. Secondly, the use of biomarkers indicating drops in overall concentrations at around 130 ft. In both porphyrins and carotenoids, the concentrations drop to almost zero at 130 ft. Since the F/F boundary is an extinction event, it follows that primary productivity indicators and GSB drop off at the extinction boundary. Although this also cannot definitively state where the F/F boundary is located, it could indicate the change from a TST to a HST, resulting in the absence of these biomarkers. The placement of the F/F boundary at 130 ft remains speculative until more works can be done and more data collected to give a more definitive depth location.

4.6 Changes of Deposition Environment during Woodford

There have been two models proposed to explain the oceanic circulation, resulting in an anoxic stratified water column (Figure 33). The first is the upwelling model, where cold, deep, oxygen-poor, and phosphate-rich water is brought up from the deep ocean resulting in primary producer blooms and anoxia (Chan and Archer, 2003; Molinares-Blanco, 2013; Connock, 2015). This model, however, does not fit the area or the data (Molinares-Blanco, 2013). The upwelling model would result in more phosphate being found in the sediment, but only the Upper Woodford Shale has high concentrations of phosphates. Upwelling would also have caused disturbance to the chemocline, which would prevent GSB from growing due to the increased mixing. Considering the high concentrations of isorenieratane(**I**) and paleorenieratane(**II**) found throughout the Woodford Shale, this model becomes less feasible. Furthermore, in modern sulfidic upwelling zones analogous to the ones proposed by the upwelling model, GSB are not found (French et al., 2014). Therefore, the upwelling model is not a likely candidate to explain the environment of deposition. The second proposed model is the stagnant circulation model, characterized by epeiric seas, high phytoplankton productivity from continental nutrient input, and shallow continental shelf environments (Figure 33), (Ozaki et al., 2011; Molinares-Blanco, 2013; Connock, 2015).

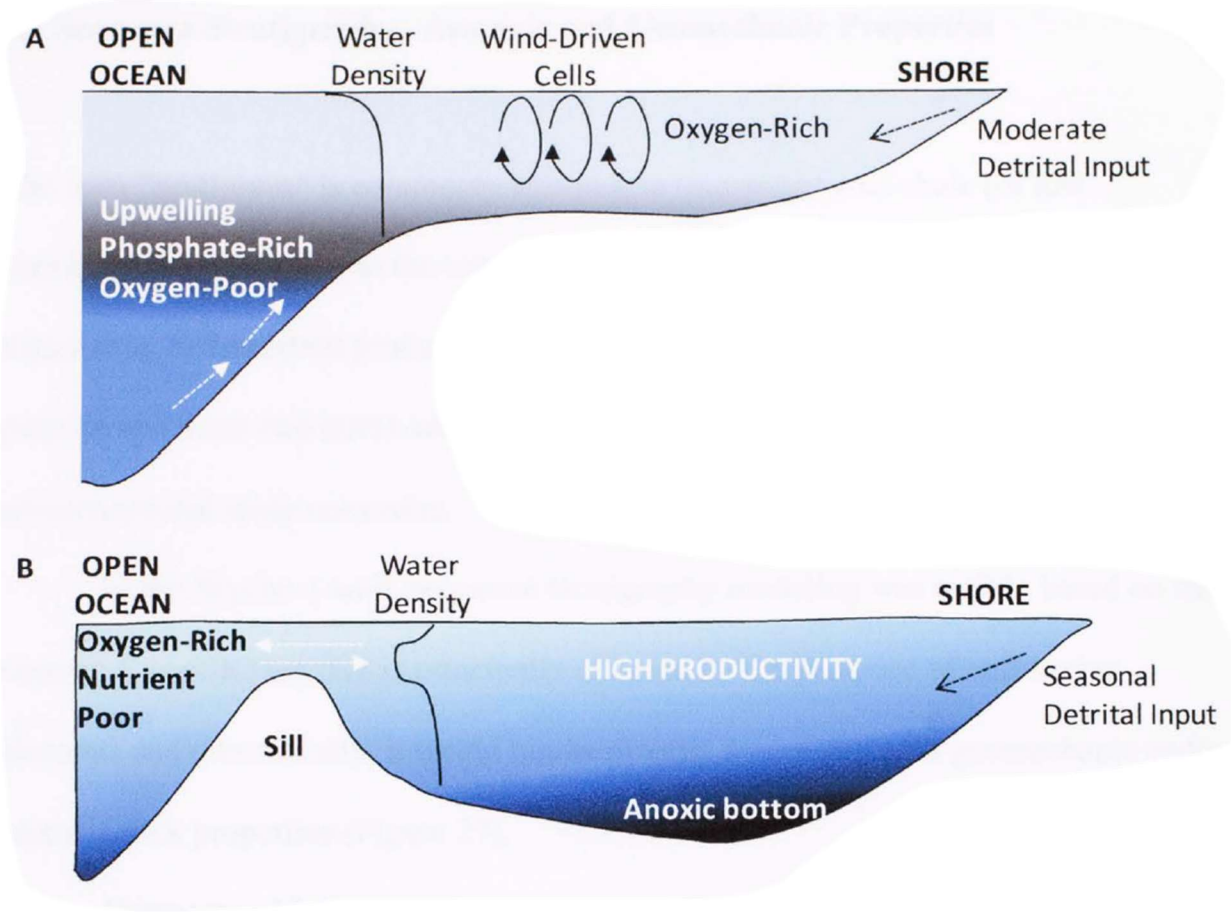

Figure 33. A) Upwelling model proposed for triggering the Late Devonian anoxic black shales. B) Stagnant circulation model proposed for triggering the Late Devonian anoxic black shales (Molinares-Blanco, 2013)

The sustained and strong stratification indicated by isorenieratane(**I**) and paleorenieratane(**II**) in the Middle Woodford Shale seems to fit this model much better (Molinares-Blanco, 2013; Connock et al., 2018). Stagnant waters would allow for the GSB to proliferate and remain relatively undisturbed and result in the increased concentrations of isorenieratane(**I**) and paleorenieratane(**II**) that is seen.

The Lower Woodford Shale is characterized by episodic PZE (Connock et al., 2018), seen by fluctuating carotenoid concentrations. As previously mentioned, the increases in concentration correspond to a regressive hemicycle followed by a transgressive hemicycle. The

Lower Woodford Shale begins in an anoxic environment based on the metalloporphyrins, then becomes oxygenated with a few spikes of anoxia. Based on the primary productivity indicators such as the MTTCs and total porphyrins, the productivity remains low. A small spike is seen in the porphyrins right before the Lower/Middle Woodford Shale boundary, which corresponds to the peak of a small transgressive hemicycle. Based on the MTTCI, the salinity in the early Lower Woodford Shale is moderately high but quickly decreases and remains relatively low through the rest of the Lower Woodford Shale.

The early Middle Woodford Shale seems to have mixed bottom waters with little to no PZE, judging by the concentration of aromatic carotenoids being low. Based on the VO/Ni ratio, there are a few isolated spikes of anoxia in the early Middle Woodford Shale. The environment begins to see increased euxinia in the mid Middle Woodford Shale, evidenced by both the increase in aromatic carotenoids and the VO/Ni ratio. During much of the Middle Woodford Shale, there is a general regressive cycle that coincides with the increased euxinia evidenced by the presence of GSB. This regressive cycle coincides with sustained PZE, ending with a significant transgressive hemicycle and the end of the PZE in the late Upper Woodford Shale. Inside the general regression, there are smaller transgressive hemicycles; at around 150 ft, a small transgressive hemicycle coincides with the increase in nickel porphyrin preservation and a change in lithology. The significance and cause of this anomaly in the nickel porphyrin concentration are as yet unknown. The sharp transgression at 130 ft, ending the general regression, also coincides with increased salinity indicated by the MTTCI ratio. This could mean that the transgression brought along the upwelling of deep saline water, which disturbed the water stratification and destroying the habitat of the GSB. According to proxies of primary

productivity like the porphyrins, MTTCs, and TMPBQ, the Middle Woodford Shale begins with higher productivity which subsequently decreases. The concentration of these proxies then begins to rise and then fall around the same depths as the sustained PZE. This might indicate that they do not show an increase in primary productivity but instead show increased organic matter preservation.

Oxygenation increases significantly, and stratification decreases in the Upper Woodford Shale. This increase in oxygenation is evidenced by the VO/Ni ratio decreasing and remaining low for most of the Upper Woodford Shale. The Upper Woodford Shale is also characterized by a large regression and overall is a HST likely as a result of Late Devonian glaciation; there are some small transgressive hemicycles, but they remain small before returning to a regressive hemicycle. Concentrations of isorenieratane and paleorenieratane remain low through the Upper Woodford Shale, with a small spike in the mid Upper Woodford Shale. The primary productivity proxies significantly increase in the Upper Woodford Shale, which also indicates that the oxygenation has increased. Salinity drops in the early Upper Woodford Shale but sees a few spikes before dropping again. The Upper Woodford Shale also contains phosphate nodules (Molinares-Blanco, 2013), indicating an abundance of phosphorous in the water column, allowing primary productivity not to be limited by this resource. Although the increase in oxygenation, phosphate nodules, primary productivity evidence, and salinity suggests that upwelling might be present in the Upper Woodford Shale, it most likely is not the case. Phosphate nodules do not appear to be triggered by upwelling in the Upper Woodford Shale, and phosphate is not necessarily a reliable indicator of upwelling (O'Brien and Veeh, 1983).

CHAPTER V

5. Conclusions

Based on the correlation of the isorenieratane/paleorenieratane ratio between the LCMS and the GCMS methods, the new faster LCMS method is viable for future characterization. This allows for the faster processing of black shale samples, which will provide greater resolution for the biomarkers they contain. In addition, the LCMS method detects carotenoids easier than GCMS without risking damage to the instrument. It thusly will provide a method to analyze polar biomarkers that previously were unable to be detected using GCMS.

The metalloporphyrins provided an interesting and unexpected result. While they have been utilized as a proxy of the water column redox potential and thermal maturity in the past, they were also used as an indicator of primary productivity in this study. They showed that primary productivity increased in the middle of the Middle Woodford Shale and the Upper Woodford Shale. The results were interesting and unexpected when the binding metal species were analyzed. Previously the ratio of nickel and vanadyl coordinated to the porphyrin has been used to indicate the redox potential of the water column. When using this ratio, there was an anomaly in the Middle Woodford Shale that disagreed with other biomarkers such as isorenieratane. This prompted an in-depth look at the ratios of the chelated metals to the different porphyrins. It was found that the porphyrins have an affinity to which metal they coordinate, so the explanation as to why this was seen needed to be found. The most probable explanation is the coordination shape of the metal ions, one being square planar in the plane of the ring and one being square pyramidal outside the plane of the ring, and the rigidity of

different porphyrin structures resulting in the difficulty of coordinating the Ni ion to porphyrins other than ETIO. This bias is also observed by Connock (2021) in another black shale core from a different time period using the same LCMS method, but has not been reported in previously published studies. This bias might discredit nickel and vanadyl metalloporphyrins from use as a proxy for redox potential in future studies unless more work can be done analyzing the metal porphyrin chelation bias and its implications for its use as a biomarker.

The novel compound trimethylphytylbenzoquinone (TMPBQ) and methyltrimethyltridecylchromans (MTTCs) strongly correlate to one another in the Woodford Shale, indicating they are likely from the same source. Based on that assessment and the similarity in structure between them, it is likely that the MTTCs are a degradation product of TMPBQ, but a compound-specific isotopic comparison would be needed to confirm this hypothesis. Since TMPBQ is part of the α-tocopherol quinone recycling system, it can be inferred that it relates to environmental stressors. Because of this, it indicates that the chemocline was shallowing in the Middle Woodford Shale, which pushed these phytoplankton higher in the water column exposing them to more intense light conditions. In the Upper Woodford Shale, the oxygenation of the water column resulted in much larger populations of phytoplankton resulting in the increase seen there. Moreover, the TMPBQ/α-MTTC ratio might help determine the organic matter preservation potential in the water column. Since MTTC is possibly a degradation product of TMPBQ, a high ratio would indicate high preservation, and a low ratio would be low preservation. It shows that preservation increased in the Middle Woodford Shale coinciding with isorenieratane and then again in the early Upper Woodford Shale. The TMPBQ isomer ratio might indicate redox conditions, while the ratio calculated

tentatively agreed with other redox proxies, the equation and lack of a first peak being detected in many samples resulted in very few data points which means a conclusion on this aspect is tentative at best. The MTTCI ratio showed that salinity remains relatively low in the Lower Woodford Shale and early Middle Woodford Shale. In the late Middle Woodford Shale, the salinity spikes before returning to the previous norm in the early Upper Woodford Shale and then spiking again in the middle Upper Woodford Shale. The salinity increase corresponds with the development of the HST and the significant decrease in all the biomarkers.

Finding the location of the F/F boundary remains uncertain. Using carbon isotope excursions to locate the Kellwasser events suggests that the boundary might be later than previously proposed. This, however, is not conclusive as there were few samples tested, so they were included into the previously found data. Different measurement techniques could have manifested in skewed results. More testing will need to be done to more accurately use our samples with isotope data to find the boundaries. Biomarker results found in this study do seem to agree with the isotope data and boundary locations reported by Molinares-Blanco (2019). Molinares-Blanco (2019) stated that the boundary is around 130 ft which corresponds to when all measured biomarkers decrease in abundance. The D/C boundary is the top of the Woodford Shale, which seems to agree with the isotope data indicating a positive excursion at the Woodford Shale top.

The stagnant circulation model best describes the environment of deposition. If there were upwelling occurring, there would be a lack of isorenieratane and paleorenieratane since modern analogs do not contain GSB. Stagnant waters, however, would allow for GSB to remain undisturbed and provide sustained strong stratification required for GSB to proliferate. The

Lower Woodford Shale has episodic PZA evidenced by the fluctuation in carotenoid concentrations with fluctuating oxygenation and low primary productivity. The Middle Woodford Shale begins with having mixed bottom waters with little to no PZE but becomes anoxic as time progresses. Eventually, there is sustained PZE where GSB grows in abundance, corresponding with a regressive hemicycle. Primary productivity seems to be high during the sustained PZE, but this might be due to the enhanced OM preservation potential of anoxic environments. The Upper Woodford Shale experienced an oxygenation increase and stratification decrease. A general regressive hemicycle characterizes the Upper Woodford Shale, but unlike in the Middle Woodford Shale, it does not correspond to anoxia and water column stratification. Primary productivity significantly increases in the Upper Woodford Shale, but isorenieratane and paleorenieratane remain low.

FUTURE WORK

1. Investigate the bias in formation between VO and Ni porphyrins. The bias found in this study between the metalloporphyrins might exclude them from future utilization without further investigation on the mechanism of metal chelation to fossil porphyrins. Getting standards of free porphyrins and under laboratory conditions testing their coordination with the metals should provide insight into what causes this bias. X-ray crystallography can also be used to show the 3D structure of these metalloporphyrins

which might further offer an explanation as to the cause of the bias. Another structural characterization method that could be used would be Non-contact Atomic Force Microscopy similar to the one used in Zhang et. al (2019).

2. Test if GSB can survive in sulfide conditions low enough that would allow for Ni to be present in large enough concentrations to allow the formation of Ni porphyrins. Ni being high between the depths of 155-133 ft suggests there is low sulfide in the water preventing nickel sulfide from forming. It is important to know if GSB can continue to live in low sulfide environments low enough for Ni to continue to exist in order to explain the high Ni between these depths that occur along with high carotenoid concentrations. To test this laboratory growth of GSB might be required testing different concentrations of sulfide. The lowest concentrations would then need to be compared to the highest concentrations of sulfide in which nickel does not precipitate out as nickel sulfide.
3. More research needs to be done on TMPBQ and what it could possibly indicate about the environment of deposition. This would start with compound specific isotope measurements of TMPBQ and of MTTCs to determine if they are likely from the same source.
4. Testing the rest of our samples for their organic carbon isotope ratios. The rest of the samples being tested with the same method would be beneficial in determining the location of positive excursions which would indicate the locations of the F/F boundary and the Kellwasser events. While the Molinares-Blanco (2019) isotope data seems to indicate where the boundary is our data seems to disagree. Further testing should be

done to determine if it is something in the testing causing the isotope data to disagree or if the location of the boundary is indeed at a different depth. Combining the isotope data with the biomarker data from this study should provide strong evidence for the actual depth.

BIBLIOGRAPHY

Abousleiman, Y.N., Tran, M.H., Hoang, S., Bobko, C.P., Ortega, A., Ulm, F.-J., 2007. Geomechanics Field and Laboratory Characterization of the Woodford Shale: The Next Gas Play. Presented at the SPE Annual Technical Conference and Exhibition, OnePetro. doi:10.2118/110120-MS

Aderoju, T., Bend, S., 2018. Reconstructing the palaeoecosystem and palaeodepositional environment within the Upper Devonian–Lower Mississippian Bakken Formation: A biomarker approach. Organic Geochemistry 119, 91–100.

Algeo, T.J., Berner, R.A., Maynard, J.B., Scheckler, S.E., 1995. Late Devonian Oceanic Anoxic Events and Biotic Crises: "Rooted" in the Evolution of Vascular Land Plants? GSA TODAY 24.

Algeo, T.J., Scheckler, S.E., Beerling, D.J., Chaloner, W.G., Woodward, F.I., 1998. Terrestrial-marine teleconnections in the Devonian: links between the evolution of land plants, weathering processes, and marine anoxic events. Philosophical Transactions of the Royal Society of London. Series B: Biological Sciences 353, 113–130.

Baker, E.W., Louda, J.W., 1983. Thermal Aspects of Chlorophyll Geochemistry. Advances in Organic Geochemistry (Edited by Bjorøy M. et al) Chichester, Wiley 401–421.

Barwise, A.J.G., Roberts, J., 1984. Diagenetic and catagenetic pathways for porphyrins in sediments. Organic Geochemistry 6, 167–176.

Bergquist, B.A., 2017. Mercury, volcanism, and mass extinctions. Proceedings of the National Academy of Sciences 114, 8675–8677.

Biebl, H., Pfennig, N., 1978. Growth yields of green sulfur bacteria in mixed cultures with sulfur and sulfate reducing bacteria. Archives of Microbiology 117, 9–16.

Brocks, J.J., Schaeffer, P., 2008. Okenane, a biomarker for purple sulfur bacteria (Chromatiaceae), and other new carotenoid derivatives from the 1640Ma Barney Creek Formation. Geochimica et Cosmochimica Acta 72, 1396–1414.

Brocks, J.J., Summons, R.E., 2005. Sedimentary Hydrocarbons, Biomarkers for Early Life, in: Schlesinger, W.H. (Ed.), Biogeochemistry. Elsevier Ltd, pp. 63–115.

Brune, D.C., 1989. Sulfur oxidation by phototrophic bacteria. Biochimica et Biophysica Acta (BBA) - Bioenergetics 975, 189–221.

Buckner, N., Slatt, R.M., Coffey, B., Davis, R.J., 2009. Stratigraphy of the Woodford Shale from Behind-Outcrop Drilling, Logging, and Coring. AAPG Search and Discovery article #5014, 24.

Cardott, B.J., 2012. Thermal maturity of Woodford Shale gas and oil plays, Oklahoma, USA. International Journal of Coal Geology, Shale Gas and Shale Oil Petrology and Petrophysics 103, 109–119.

Catuneanu, O., 2017. Chapter One - Sequence Stratigraphy: Guidelines for a Standard Methodology, in: Montenari, M. (Ed.), Stratigraphy & Timescales, Advances in Sequence Stratigraphy. Academic Press, pp. 1–57.

Chan, M.A., Archer, A.W., 2003. Extreme Depositional Environments: Mega End Members in Geologic Time. Geological Society of America.

Chen, D., Qing, H., Li, R., 2005. The Late Devonian Frasnian–Famennian (F/F) biotic crisis: Insights from δ13Ccarb, δ13Corg and 87Sr/86Sr isotopic systematics. Earth and Planetary Science Letters 235, 151–166.

Chen, J.H., Philp, R.P., 1991. Porphyrin distributions in crude oils from the Jianghan and Biyang basins, China. Chemical Geology 91, 139–151.

Chicarelli, M.I., Wolff, G.A., Murray, M., Maxwell, J.R., 1984. Porphyrins with a novel exocyclic ring system in an oil shale. Tetrahedron 40, 4033–4039.

Clifford, D.J., Clayton, J.L., Sinninghe Damsté, J.S., 1998. 2,3,6-/3,4,5-Trimethyl substituted diaryl carotenoid derivatives (Chlorobiaceae) in petroleums of the Belarussian Pripyat River Basin. Organic Geochemistry 29, 1253–1267.

Comer, J., 1991. Stratigraphic Analysis of the Upper Devonian Woodford Formation, Permian Basin, West Texas and Southeastern New Mexico (Report Investigation), Report Investigation. University of Texas at Austin, Bureau of Economic Geology. doi:10.23867/RI0201D

Connock, G.T., 2015. Paleoenvironmental Interpretation of the Woodford Shale, Wyche Farm Shale Pit, Pontotoc Country, Arkoma Basin, Oklahoma With Primary Focus on Water Column Structure. University of Oklahoma.

Connock, G.T., 2021. Novel Biomarker Application Reveals the Microbial Ecological Dynamics Surrounding Oceanic Anoxic Event II (OAE-2). University of Oklahoma.

Connock, G.T., Nguyen, T.X., Philp, R.P., 2018. The development and extent of photic-zone euxinia concomitant with Woodford Shale deposition. AAPG Bulletin 102, 959–986.

Copper, P., 1986. Frasnian/Famennian mass extinction and cold-water oceans. Geology 14, 835–839.

Cui, X., Liu, X.-L., Shen, G., Ma, J., Husain, F., Rocher, D., Zumberge, J.E., Bryant, D.A., Summons, R.E., 2020. Niche expansion for phototrophic sulfur bacteria at the Proterozoic–Phanerozoic transition. Proceedings of the National Academy of Sciences 117, 17599–17606.

Cullen, A., 2020. Woodford Shale Mercury Anomalies from the McAlister Cemetery Quarry, Oklahoma: A North American Test of the Volcanic-Trigger Hypothesis for Late Devonian Mass Extinctions. The Shale Shaker Oklahoma City Geological Society 71.

David, A., 1998. Recognition of Photic Zone Anoxia from LC-MS Studies of Porphyrin Distributions in Ancient Sediments. University of Bristol.

De Vleeschouwer, D., Rakociński, M., Racki, G., Bond, D.P.G., Sobień, K., Claeys, P., 2013. The astronomical rhythm of Late-Devonian climate change (Kowala section, Holy Cross Mountains, Poland). Earth and Planetary Science Letters 365, 25–37.

Drew, M.G.B., Mitchell, P.C.H., Scott, C.E., 1984. Crystal and molecular structure of three oxovanadium(IV) porphyrins: oxovanadium tetraphenylporphyrin(I), oxovanadium(IV) etioporphyrin(II) and the 1:2 adduct of (II) with 1,4-dihydroxybenzene(III). Hydrogen bonding involving the VO group. Relevance to catalytic demetallisation. Inorganica Chimica Acta 82, 63–68.

Dutta, S., Bhattacharya, S., Raju, S.V., 2013. Biomarker signatures from Neoproterozoic–Early Cambrian oil, western India. Organic Geochemistry 56, 68–80.

Eckardt, C.B., Keely, B.J., Waring, J.R., Chicarelli, M.I., Maxwell, J.R., De Leeuw, J.W., Boon, J.J., Runnegar, B., Macko, S., Hudson, J.D., 1991. Preservation of Chlorophyll-Derived Pigments in Sedimentary Organic Matter [and Discussion]. Philosophical Transactions: Biological Sciences 333, 339–348.

Eganhouse, R.P., 1997. Molecular Markers and Environmental Organic Geochemistry: An Overview, in: Molecular Markers in Environmental Geochemistry, ACS Symposium Series. American Chemical Society, pp. 1–20.

Ettensohn, F.R., 1992. Controls on the origin of the Devonian-Mississippian oil and gas shales, east-central United States. Fuel 71, 1487–1492.

Fang, H., Yongchuan, S., Yaozong, L., 1993. Application of organic facies studies to sedimentary basin analysis: a case study from the Yitong Graben, China. Organic Geochemistry 20, 27–42.

Farrimond, P., Taylor, A., TelnÆs, N., 1998. Biomarker maturity parameters: the role of generation and thermal degradation. Organic Geochemistry 29, 1181–1197.

French, K.L., Rocher, D., Zumberge, J.E., Summons, R.E., 2015. Assessing the distribution of sedimentary C 40 carotenoids through time. Geobiology 13, 139–151.

French, K.L., Sepúlveda, J., Trabucho-Alexandre, J., Gröcke, D.R., Summons, R.E., 2014. Organic geochemistry of the early Toarcian oceanic anoxic event in Hawsker Bottoms, Yorkshire, England. Earth and Planetary Science Letters 390, 116–127.

Frigaard, N.-U., Bryant, D.A., 2004. Seeing green bacteria in a new light: genomics-enabled studies of the photosynthetic apparatus in green sulfur bacteria and filamentous anoxygenic phototrophic bacteria. Archives of Microbiology 182, 265–276.

Frigaard, N.-U., Chew, A.G.M., Li, H., Maresca, J.A., Bryant, D.A., 2003. Chlorobium Tepidum: Insights into the Structure, Physiology, and Metabolism of a Green Sulfur Bacterium Derived from the Complete Genome Sequence. Photosynthesis Research 78, 93–117.

Frigaard, N.-U., Maresca, J.A., Yunker, C.E., Jones, A.D., Bryant, D.A., 2004. Genetic Manipulation of Carotenoid Biosynthesis in the Green Sulfur Bacterium Chlorobium tepidum. Journal of Bacteriology 186, 5210–5220.

Fulton, J.M., Arthur, M.A., Thomas, B., Freeman, K.H., 2018. Pigment carbon and nitrogen isotopic signatures in euxinic basins. Geobiology 16, 429–445.

Goericke, R., Strom, S.L., Bell, M.A., 2000. Distribution and sources of cyclic pheophorbides in the marine environment. Limnology and Oceanography 45, 200–211.

Grasby, S.E., Them, T.R., Chen, Z., Yin, R., Ardakani, O.H., 2019. Mercury as a proxy for volcanic emissions in the geologic record. Earth-Science Reviews 196, 102880.

Grice, K., Brocks, J.J., 2011. BIOMARKERS (ORGANIC, COMPOUND-SPECIFIC ISOTOPES). Encyclopedia of Geobiology 167–182.

Grice, K., Schaeffer, P., Schwark, L., Maxwell, J.R., 1996. Molecular indicators of palaeoenvironmental conditions in an immature Permian shale (Kupferschiefer, Lower Rhine Basin, north-west Germany) from free and S-bound lipids. Organic Geochemistry 25, 131–147.

Grosjean, E., Adam, P., Connan, J., Albrecht, P., 2004. Effects of weathering on nickel and vanadyl porphyrins of a Lower Toarcian shale of the Paris basin1 1Associate editor: G. Logan. Geochimica et Cosmochimica Acta 68, 789–804.

Gueneli, N., McKenna, A.M., Ohkouchi, N., Boreham, C.J., Beghin, J., Javaux, E.J., Brocks, J.J., 2018. 1.1-billion-year-old porphyrins establish a marine ecosystem dominated by bacterial primary producers. Proceedings of the National Academy of Sciences 115, E6978–E6986.

Hartgers, W.A., Damsté, J.S.S., Koopmans, M.P., Leeuw, J.W. de, 1993. Sedimentary evidence for a diaromatic carotenoid with an unprecedented aromatic substitution pattern. Journal of the Chemical Society, Chemical Communications 1715–1716.

Hartgers, W.A., Sinninghe Damsté, J.S., Requejo, A.G., Allan, J., Hayes, J.M., Ling, Y., Xie, T.-M., Primack, J., de Leeuw, J.W., 1994. A molecular and carbon isotopic study towards the origin and diagenetic fate of diaromatic carotenoids. Organic Geochemistry 22, 703–725.

Hartkopf-Fröder, C., Kloppisch, M., Mann, U., Neumann-Mahlkau, P., Schaefer, R.G., Wilkes, H., 2007. The end-Frasnian mass extinction in the Eifel Mountains, Germany: new insights from organic matter composition and preservation. Geological Society, London, Special Publications 278, 173–196.

Huseby, B., Barth, T., Ocampo, R., 1996. Porphyrins in Upper Jurassic source rocks and correlations with other source rock descriptors. Organic Geochemistry 25, 273–294.

Isaksen, G.H., Bohacs, K.M., 1995. Geological Controls of Source Rock Geochemistry Through Relative Sea Level; Triassic, Barents Sea, in: Katz, B.J. (Ed.), Petroleum Source Rocks. Springer Berlin Heidelberg, Berlin, Heidelberg, pp. 25–50.

Jiang, K., Lin, C., Cai, C., Zhang, X., Huang, S., Fan, Z., 2019. Current Status and Challenges of Methyltrimethyltridecylchromans Research in Source Rocks and Crude Oils. ACS Omega 4, 9835–9842.

Jiang, K., Lin, C., Zhang, X., Cai, C., Xiao, F., He, W., Peng, L., 2018. Variations in abundance and distribution of methyltrimethyltridecylchromans (MTTCs) in sediments from saline lacustrine settings in Cenozoic lacustrine basins, China. Organic Geochemistry 121, 58–67.

Joachimski, M.M., Buggisch, W., 2002. Conodont apatite δ18O signatures indicate climatic cooling as a trigger of the Late Devonian mass extinction. Geology 30, 711–714.

Johnson, J.G., Klapper, G., Sandberg, C.A., 1985. Devonian eustatic fluctuations in Euramerica. GSA Bulletin 96, 567–587.

Johnson, K., Suneson, N., 1997. Rockhounding and earth-science activities in Oklahoma, 1995 workshop.

Jones, L.C., 2017. An Integrated Analysis of Sequence Stratigraphy, Petroleum Geochemistry, and Devonian Mass Extinction Events in the Woodford Shale, Southern Oklahoma. University of Oklahoma.

Junium, C.K., Freeman, K.H., Arthur, M.A., 2015. Controls on the stratigraphic distribution and nitrogen isotopic composition of zinc, vanadyl and free base porphyrins through Oceanic Anoxic Event 2 at Demerara Rise. Organic Geochemistry 80, 60–71.

Junium, C.K., Mawson, D.H., Arthur, M.A., Freeman, K.H., Keely, B.J., 2008. Unexpected occurrence and significance of zinc alkyl porphyrins in Cenomanian–Turonian black shales of the Demerara Rise. Organic Geochemistry, Advances in Organic Geochemistry 2007 39, 1081–1087.

Kim, J.S., Reibenspies, J.H., Darensbourg, M.Y., 1996. Characteristics of Nickel(0), Nickel(I), and Nickel(II) in Phosphino Thioether Complexes: Molecular Structure and S-Dealkylation of (Ph2P(o-C6H4)SCH3)2Ni0. Journal of the American Chemical Society 118, 4115–4123.

Kohnen, M.E.L., Schouten, S., Damsté, J.S.S., Leeuw, J.W. de, Merritt, D.A., Hayes, J.M., 1992. Recognition of Paleobiochemicals by a Combined Molecular Sulfur and Isotope Geochemical Approach. Science 256, 358–362.

Koopmans, M.P., Köster, J., Van Kaam-Peters, H.M.E., Kenig, F., Schouten, S., Hartgers, W.A., de Leeuw, J.W., Sinninghe Damsté, J.S., 1996a. Diagenetic and catagenetic products of isorenieratene: Molecular indicators for photic zone anoxia. Geochimica et Cosmochimica Acta 60, 4467–4496.

Koopmans, M.P., Schouten, S., Kohnen, M.E.L., Sinninghe Damsté, J.S., 1996b. Restricted utility of aryl isoprenoids as indicators for photic zone anoxia. Geochimica et Cosmochimica Acta 60, 4873–4876.

Kravchinsky, V.A., Konstantinov, K.M., Courtillot, V., Savrasov, J.I., Valet, J.-P., Cherniy, S.D., Mishenin, S.G., Parasotka, B.S., 2002. Palaeomagnetism of East Siberian traps and kimberlites: two new poles and palaeogeographic reconstructions at about 360 and 250 Ma. Geophysical Journal International 148, 1–33.

Lewan, M.D., 1984. Factors controlling the proportionality of vanadium to nickel in crude oils. Geochimica et Cosmochimica Acta 48, 2231–2238.

Lewan, M.D., Maynard, J.B., 1982. Factors controlling enrichment of vanadium and nickel in the bitumen of organic sedimentary rocks. Geochimica et Cosmochimica Acta 46, 2547–2560.

Li, M., Larter, S.R., Taylor, P., Jones, D.M., Bowler, B., Bjoroy, M., 1995. Biomarkers or not biomarkers? A new hypothesis for the origin of pristane involving derivation from

methyltrimethyltridecylchromans (MTTCs) formed during diagenesis from chlorophyll and alkylphenols. Organic Geochemistry 23, 159–167.

Louda, J.W., Loitz, J.W., Rudnick, D.T., Baker, E.W., 2000. Early diagenetic alteration of chlorophyll-a and bacteriochlorophyll-a in a contemporaneous marl ecosystem; Florida Bay. Organic Geochemistry 31, 1561–1580.

Louda, J.W., Mongkhonsri, P., Baker, E.W., 2011. Chlorophyll degradation during senescence and death-III: 3–10yr experiments, implications for ETIO series generation. Organic Geochemistry 42, 688–699.

Lushchak, V.I., Semchuk, N.M., 2012. Tocopherol biosynthesis: chemistry, regulation and effects of environmental factors. Acta Physiologiae Plantarum 34, 1607–1628.

Marín, P., Márquez, G., Gallego, J.R., Permanyer, A., 2014. Characterization of asphaltic oil occurrences from the southeastern margin of the Basque-Cantabrian Basin, Spain. Geologica Acta 12, 327–342.

McGhee, G.R., 1996. The Late Devonian Mass Extinction: The Frasnian/Famennian Crisis. Columbia University Press.

Meyer, K.M., Kump, L.R., 2008. Oceanic Euxinia in Earth History: Causes and Consequences. Annual Review of Earth and Planetary Sciences 36, 251–288.

Meyer, K.M., Macalady, J.L., Fulton, J.M., Kump, L.R., Schaperdoth, I., Freeman, K.H., 2011. Carotenoid biomarkers as an imperfect reflection of the anoxygenic phototrophic community in meromictic Fayetteville Green Lake. Geobiology 9, 321–329.

Moldowan, J.M., Seifert, W.K., Gallegos, E.J., 1985. Relationship Between Petroleum Composition and Depositional Environment of Petroleum Source Rocks1. AAPG Bulletin 69, 1255–1268.

Molinares-Blanco, C.E., 2013. Stratigraphy and Palynomorphs Composition of the Woodford Shale in the Wyche Farm Shale Pit, Pontotoc County, Oklahoma. The University of Oklahoma.

Molinares-Blanco, C.E., 2019. Paleoenvironments and Sediments Around the Frasnian/Famennian (F/F) Transition in the Woodford Shale, South Central Oklahoma – A Multiproxy Approach. The University of Oklahoma.

Mosbrugger, V., 1990. The Tree Habit in Land Plants: A Functional Comparison of Trunk Constructions with a Brief Introduction into the Biomechanics of Trees. Springer.

O'Brien, G.W., Veeh, H.H., 1983. Are Phosphorites Reliable Indicators of Upwelling ?, in: Suess, E., Thiede, J. (Eds.), Coastal Upwelling Its Sediment Record: Part A: Responses of the Sedimentary Regime to Present Coastal Upwelling, NATO Conference Series. Springer US, Boston, MA, pp. 399–419.

Ohkouchi, N., Y, C., Kashiyama, Y., Ogawa, N., 2010. Isotopomers of chlorophyll nuclei: Theory and application. pp. 271–290.

Over, D., 1990. Conodont biostratigraphy of the Woodford shale (late Devonian-early Carboniferous) in the Arbuckle Mountains, south-central Oklahoma.

Over, D.J., 2002. The Frasnian/Famennian boundary in central and eastern United States. Palaeogeography, Palaeoclimatology, Palaeoecology 181, 153–169.

Overmann, J., Cypionka, H., Pfennig, N., 1992. An extremely low-light adapted phototrophic sulfur bacterium from the Black Sea. Limnology and Oceanography 37, 150–155.

Ozaki, K., Tajima, S., Tajika, E., 2011. Conditions required for oceanic anoxia/euxinia: Constraints from a one-dimensional ocean biogeochemical cycle model. Earth and Planetary Science Letters 304, 270–279.

Perry, W.J., Gautier, D.L., Dolton, G.L., Takahashi, K.I., Varnes, K.L., 1995. Arkoma Basin Province (062) 17.

Peters, K.E., Walters, C.C., Moldowan, J.M., 2005. The Biomarker Guide, Biomarkers and Isotopes in Petroleum Exploration and Earth History, 2nd ed. Cambridge University Press, Cambridge.

Philp, R.P., DeGarmo, C.D., 2020. Geochemical characterization of the Devonian-Mississippian Woodford Shale from the McAlister Cemetery Quarry, Criner Hills Uplift, Ardmore Basin, Oklahoma. Marine and Petroleum Geology 112, 104078.

Portas, R.M., Slatt, R., 2010. Characterization and Origin of Fracture Patterns in a Woodford Shale Quarry in Southeastern Oklahoma for Application to Exploration and Development; #50352 (2010).

Posamentier, H.W., Jervey, M.T., Vail, P.R., 1988. Eustatic Controls on Clastic Deposition I—conceptual Framework. SEPM Special Publication 42.

Posamentier, H.W., Vail, P.R., 1988. Eustatic Controls on Clastic Deposition II—Sequence and Systems Tract Models. SEPM Special Publication 42.

Pyle, D.M., Mather, T.A., 2003. The importance of volcanic emissions for the global atmospheric mercury cycle. Atmospheric Environment 37, 5115–5124.

Qian, K., Edwards, K.E., Mennito, A.S., Walters, C.C., Kushnerick, J.D., 2010. Enrichment, Resolution, and Identification of Nickel Porphyrins in Petroleum Asphaltene by Cyclograph Separation and Atmospheric Pressure Photoionization Fourier Transform Ion Cyclotron Resonance Mass Spectrometry. Analytical Chemistry 82, 413–419.

Racki, G., 1999. The Frasnian–Famennian biotic crisis: How many (if any) bolide impacts? Geologische Rundschau 87, 617–632.

Rakociński, M., Marynowski, L., Pisarzowska, A., Bełdowski, J., Siedlewicz, G., Zatoń, M., Perri, M.C., Spalletta, C., Schönlaub, H.P., 2020. Volcanic related methylmercury poisoning as the possible driver of the end-Devonian Mass Extinction. Scientific Reports 10, 7344.

Romero, A.M., Philp, R.P., 2012. Organic geochemistry of the Woodford Shale, southeastern Oklahoma: How variable can shales be?Organic Geochemistry of the Woodford Shale, Southeastern Oklahoma. AAPG Bulletin 96, 493–517.

Shanfa, F., Jiamo, F., Eglinton, G., Brassell, S., 1989. The occurrence and geochemistry of Di - and trimethyl - 2- (4,8,12 trimethyltridecyl) chromans and benzohopanes in Fushun cannel coal, Northeast China. Chinese Journal of Geochemistry 8, 317–321.

Simmons, M.D., 2012. Chapter 13 - Sequence Stratigraphy and Sea-Level Change, in: Gradstein, F.M., Ogg, J.G., Schmitz, M.D., Ogg, G.M. (Eds.), The Geologic Time Scale. Elsevier, Boston, pp. 239–267.

Sinninghe Damste, J.S., Keely, B.J., Betts, S.E., Baas, M., Maxwell, J.R., de Leeuw, J.W., 1993. Variations in abundances and distributions of isoprenoid chromans and long-chain alkylbenzenes in sediments of the Mulhouse Basin: a molecular sedimentary record of palaeosalinity. Organic Geochemistry 20, 1201–1215.

Sinninghe Damste, J.S., Kock-van Dalen, A.C., de Leeuw, J.W., Schenck, P.A., Guoying, S., Brassell, S.C., 1987. The identification of mono-, di- and trimethyl 2-methyl-2-(4,8,12-trimethyltridecyl)chromans and their occurrence in the geosphere. Geochimica et Cosmochimica Acta 51, 2393–2400.

Slatt, R., Singh, P., Borges, G., Perez, R., Portas, R., Vallejo, J., Ammerman, M., Coffey, W., Eslinger, E., 2009. Reservoir Characterization of Unconventional Gas Shales: Example from the Barnett Shale, Texas, U.S.A. AAPG Search and Discovery article 30075, 25.

Slatt, R.M., Buckner, N., Abousleiman, Y., Sierra, R., Philp, P.R., Miceli-Romero, A., Portas, R., O'Brien, N., Tran, M., Davis, R., Wawrzyniec, T., 2012a. Outcrop-behind Outcrop (Quarry): Multiscale Characterization of the Woodford Gas Shale, Oklahoma 382–402.

Slatt, R.M., Philp, P.R., Abousleiman, Y., Singh, P., Perez, R., Portas, R., Marfurt, K.J., Madrid-Arroyo, S., O'Brien, N., Eslinger, E., Baruch, E.T., 2012b. Pore-to-regional-scale Integrated Characterization Workflow for Unconventional Gas Shales 127–150.

Slatt, R.M., Rodriguez, N.D., 2012. Comparative sequence stratigraphy and organic geochemistry of gas shales: Commonality or coincidence? Journal of Natural Gas Science and Engineering, Unconventional Natural Gas 8, 68–84.

Sousa Júnior, G.R., Santos, A.L.S., de Lima, S.G., Lopes, J.A.D., Reis, F.A.M., Santos Neto, E.V., Chang, H.K., 2013. Evidence for euphotic zone anoxia during the deposition of Aptian source rocks based on aryl isoprenoids in petroleum, Sergipe–Alagoas Basin, northeastern Brazil. Organic Geochemistry 63, 94–104.

Spaak, G., Edwards, D.S., Allen, H.J., Grotheer, H., Summons, R.E., Coolen, M.J.L., Grice, K., 2018. Extent and persistence of photic zone euxinia in Middle–Late Devonian seas – Insights from the Canning Basin and implications for petroleum source rock formation. Marine and Petroleum Geology 93, 33–56.

Stuart Walker, J., Keely, B.J., 2004. Distribution and significance of chlorophyll derivatives and oxidation products during the spring phytoplankton bloom in the Celtic Sea April 2002. Organic Geochemistry, Advances in Organic Geochemistry 2003. Proceedings of the 21st International Meeting on Organic Geochemistry 35, 1289–1298.

Suneson, N.H., 2012. Arkoma Basin Petroleum - Past, Present, and Future. Shale Shaker Oklahoma City Geological Society 63, 35.

Sutherland, P.K., 1988. Late Mississippian and Pennsylvanian depositional history in the Arkoma basin area, Oklahoma and Arkansas. GSA Bulletin 100, 1787–1802.

Treibs, A., 1936. Chlorophyll- und Häminderivate in organischen Mineralstoffen. Angewandte Chemie 49, 682–686.

Turner, B.W., Molinares-Blanco, C.E., Slatt, R.M., 2015. Chemostratigraphic, palynostratigraphic, and sequence stratigraphic analysis of the Woodford Shale, Wyche Farm Quarry, Pontotoc County, Oklahoma. Interpretation 3, SH1–SH9.

Turner, B.W., Tréanton, J.A., Slatt, R.M., 2016. The use of chemostratigraphy to refine ambiguous sequence stratigraphic correlations in marine mudrocks. An example from the Woodford Shale, Oklahoma, USA. Journal of the Geological Society 173, 854–868.

Urban, J.B., 1960. Microfossils of the Woodford Shale of Oklahoma. University of Oklahoma.

van Breugel, Y., Baas, M., Schouten, S., Mattioli, E., Damsté, J.S.S., 2006. Isorenieratane record in black shales from the Paris Basin, France: Constraints on recycling of respired CO2 as

a mechanism for negative carbon isotope shifts during the Toarcian oceanic anoxic event. Paleoceanography 21. doi:https://doi.org/10.1029/2006PA001305

van Breugel, Y., Schouten, S., Paetzel, M., Ossebaar, J., Sinninghe Damsté, J.S., 2005. Reconstruction of δ13C of chemocline CO2 (aq) in past oceans and lakes using the δ13C of fossil isorenieratene. Earth and Planetary Science Letters 235, 421–434.

van der Meer, M.T.J., Schouten, S., Sinninghe Damsté, J.S., 1998. The effect of the reversed tricarboxylic acid cycle on the 13C contents of bacterial lipids. Organic Geochemistry 28, 527–533.

van Gemerden, H., 1983. Physiological ecology of purple and green bacteria. Annales de l'Institut Pasteur / Microbiologie 134, 73–92.

Wang, K., Attrep, M., Orth, C.J., 1993. Global iridium anomaly, mass extinction, and redox change at the Devonian-Carboniferous boundary. Geology 21, 1071–1074.

Wignall, P.B., Kozur, H., Hallam, A., 1996. On the timing of palaeoenvironmental changes at the Permo-Triassic (P/TR) boundary using conodont biostratigraphy. Historical Biology 12, 39–62.

Zhang, Y., Schulz, F., Rytting, B.M., Walters, C.C., Kaiser, K., Metz, J.N., Harper, M.R., Merchant, S.S., Mennito, A.S., Qian, K., Kushnerick, J.D., Kilpatrick, P.K., Gross, L., 2019. Elucidating the Geometric Substitution of Petroporphyrins by Spectroscopic Analysis and Atomic Force Microscopy Molecular Imaging. Energy & Fuels 2019, 6088–6097.

APPENDIX I Compound Structures

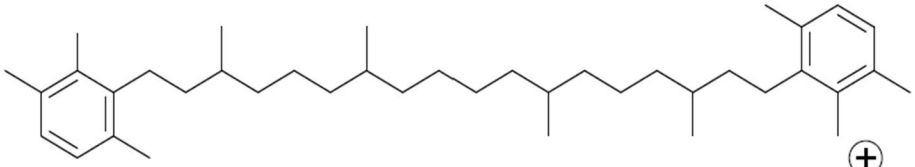

I Isorenieratane m/z: 564.5503

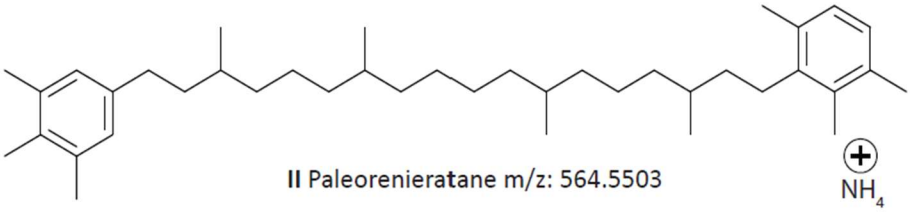

II Paleorenieratane m/z: 564.5503

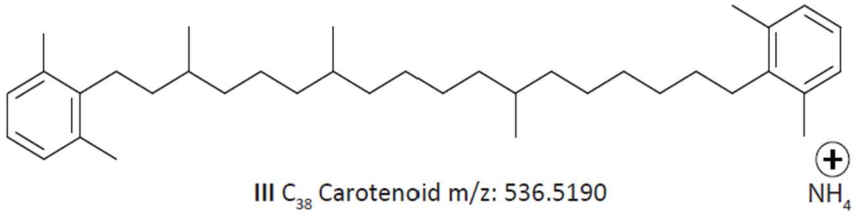

III C_{38} Carotenoid m/z: 536.5190

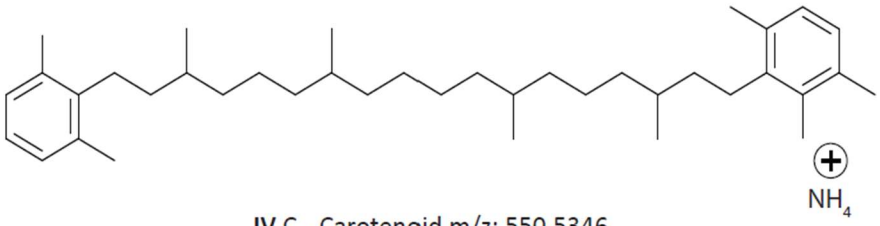

IV C_{39} Carotenoid m/z: 550.5346

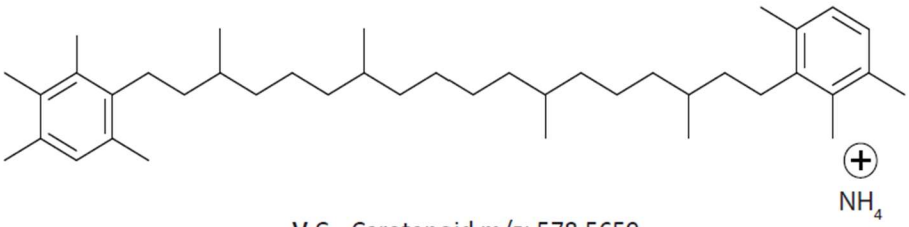

V C_{41} Carotenoid m/z: 578.5659

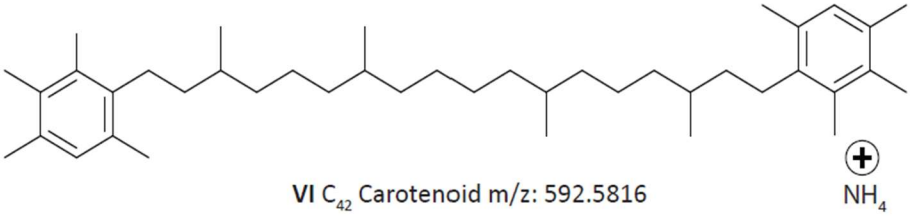

VI C_{42} Carotenoid m/z: 592.5816

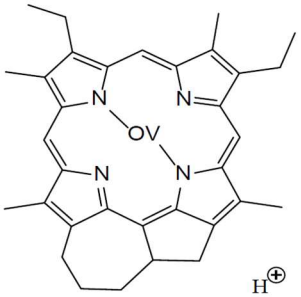

VII VO-BiCAP

C_{33} m/z: 554.2245

Alkylation Derivatives

C_{31} m/z: 526.1932

C_{32} m/z: 540.2089

C_{33} m/z: 552.2089

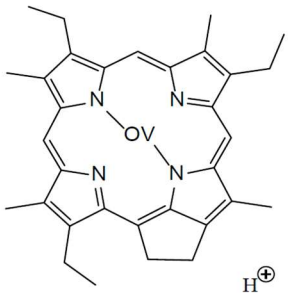

VIII VO-DPEP

C_{32} m/z: 542.2245

Alkylation Derivatives

C_{29} m/z: 500.1776

C_{30} m/z: 514.1932

C_{31} m/z: 528.2089

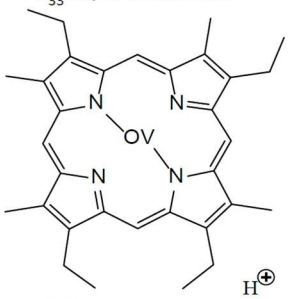

IX VO-ETIO

C_{32} m/z: 544.2402

Alkylation Derivatives

C_{29} m/z: 502.1932

C_{30} m/z: 516.2089

C_{31} m/z: 530.2245

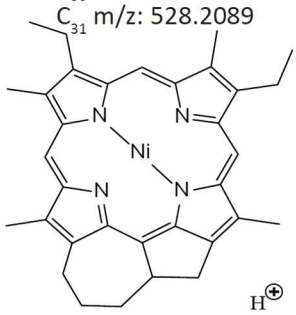

X Ni-BiCAP

C_{33} m/z: 545.2210

Alkylation Derivatives

C_{31} m/z: 517.1897

C_{32} m/z: 531.2053

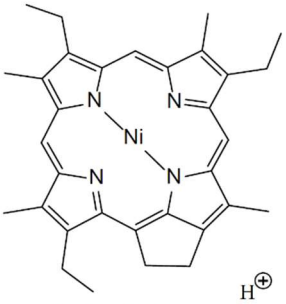

XI Ni-DPEP

C_{32} m/z: 533.2210

Alkylation Derivatives

C_{30} m/z: 505.1897

C_{31} m/z: 519.2053

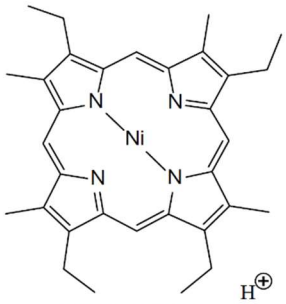

XII Ni-ETIO

C_{32} m/z: 535.2366

Alkylation Derivatives

C_{27} m/z: 465.1584

C_{28} m/z: 479.1740

C_{29} m/z: 493.1897

C_{30} m/z: 507.2053

C_{31} m/z: 521.2210

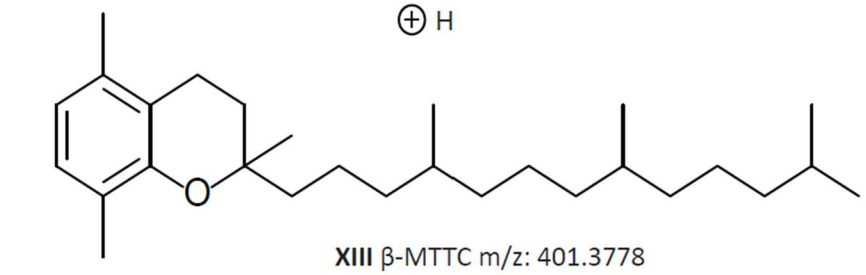

XIII β-MTTC m/z: 401.3778

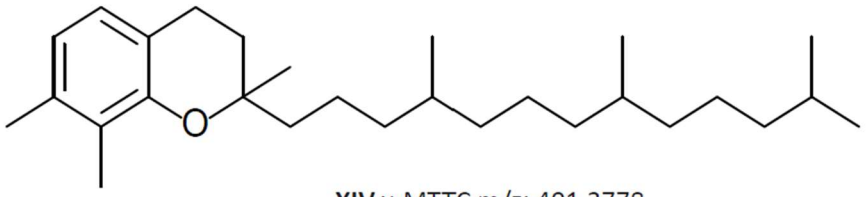

XIV γ-MTTC m/z: 401.3778

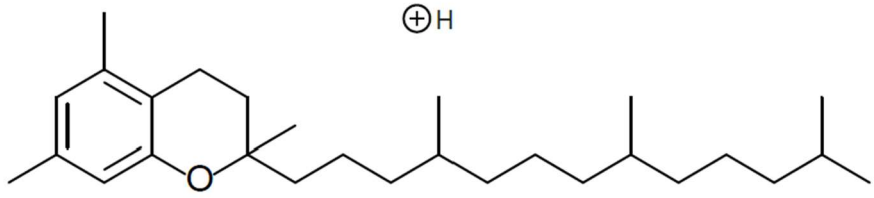

XV ζ-MTTC m/z: 401.3778

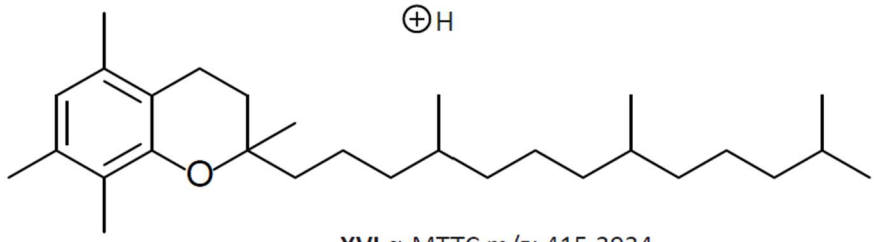

XVI α-MTTC m/z: 415.3934

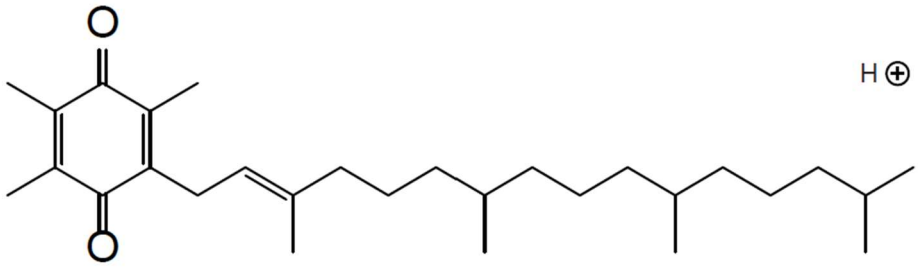

XVII TMPBQ m/z: 429.3727

APPENDIX II Tables

Table 2. Aromatic Carotenoid Methylation Derivatives(**I-VI**). Concentrations are in ng/g OC

Sample	Depth (ft)	C38 Carotenoid (ng/g OC)	C39 Carotenoid (ng/g OC)	Isorenieratane (ng/g OC)	Paleorenieratane (ng/g OC)	C41 Carotenoid (ng/g OC)	C42 Carotenoid (ng/g OC)
WCH-1	74.00	0.00	1.97	3.25	7.77	0.00	0.00
WCH-2	75.50	0.00	0.00	2.24	3.63	0.00	0.00
WCH-3	77.08	0.00	0.00	1.36	2.46	0.00	0.00
WCH-4	78.00	0.00	0.00	1.99	4.35	0.00	0.00
WCH-5	79.67	0.00	0.00	1.64	2.87	0.00	0.00
WCH-6	80.67	0.00	0.00	1.74	3.47	0.00	0.00
WCH-7	81.00	0.00	0.86	2.41	4.18	0.00	0.00
WCH-8	84.50	0.00	0.95	1.79	3.87	0.00	0.00
WCH-9	88.00	0.00	0.63	2.51	4.61	0.00	0.00
WCH-10	91.50	0.00	0.00	0.63	0.81	0.00	0.00
Wch-40	93.83	0.00	1.70	5.72	10.01	0.00	0.00
WCH-11	94.33	0.00	0.00	0.50	0.94	0.00	0.00
WCH-12	98.00	0.00	0.00	0.47	0.77	0.00	0.00
WCH-13	102.17	0.00	0.00	1.39	0.61	0.00	0.00
WCH-14	105.50	0.00	0.00	1.85	0.76	0.00	0.00
Wch-41	109.17	0.00	3.32	13.14	7.41	0.00	0.00
Wch-42	112.50	0.00	2.65	8.47	4.24	0.00	0.00
WCH-15	115.00	0.00	0.10	1.41	0.87	0.00	0.00
WCH-16	118.00	0.00	0.00	0.47	0.27	0.00	0.00
WCH-17	121.00	0.00	0.00	3.12	5.26	0.89	0.00
WCH-18	124.42	0.00	0.00	0.47	0.87	0.00	0.00
Wch-43	126.17	0.00	1.31	1.86	5.04	0.78	0.00
WCH-19	129.00	0.00	3.69	3.31	15.26	2.80	0.00
WCH-20	130.00	0.00	1.58	1.37	4.38	0.72	0.00
Wch-60	131.75	0.37	8.77	11.43	35.10	6.92	1.89
Wch-61	132.75	1.01	20.13	25.53	120.17	15.76	4.33
WCH-21	133.50	1.05	18.79	38.39	122.73	13.46	2.25
Wch-44	134.00	0.00	5.76	9.01	30.02	4.56	0.68
WCH-22	136.00	0.70	22.91	39.08	138.21	16.20	1.87
WCH-23	137.25	1.12	24.95	47.93	174.43	18.07	2.40
WCH-24	138.50	0.77	21.84	42.87	146.43	16.30	2.11
WCH-25	139.67	0.95	19.49	40.13	126.08	14.27	1.60
WCH-26	141.08	0.81	23.48	44.57	168.81	17.58	2.13
WCH-27	142.25	1.14	20.87	32.99	141.11	14.70	1.88
WCH-28	143.50	1.21	26.00	40.23	184.52	18.68	2.42
Wch-45	145.17	0.00	7.57	13.45	61.69	6.84	1.13
WCH-29	146.00	1.20	23.67	33.63	166.83	16.65	2.22
WCH-30	147.08	1.44	36.96	59.70	298.40	26.31	3.34
WCH-31	149.25	1.36	36.01	53.03	299.00	26.39	3.62
Wch-46	153.58	0.00	5.81	12.91	42.20	5.57	0.79
Wch-47	160.17	0.00	6.49	13.54	37.68	6.04	0.87
Wch-48	160.83	0.77	21.48	49.06	117.79	17.38	1.73
Wch-49	169.33	0.00	15.91	33.95	80.00	12.45	2.10
Wch-50	170.92	0.00	9.71	21.83	46.01	7.96	0.51
Wch-51	172.00	0.00	6.20	12.76	20.61	4.53	0.00
Wch-52	172.42	0.00	3.07	8.97	6.66	2.09	0.00
Wch-53	173.83	0.00	5.95	16.18	12.83	3.44	0.00
Wch-54	174.42	0.00	2.81	5.55	5.09	1.37	0.00
Wch-32	181.92	0.00	4.51	21.15	8.49	0.00	0.00
Wch-33	185.92	0.00	4.87	23.92	13.42	2.51	0.00
Wch-34	186.42	0.00	6.57	32.70	15.96	3.85	0.00
Wch-35	187.75	0.00	4.11	13.11	12.87	2.99	0.42
Wch-36	191.08	0.00	8.81	24.43	35.26	6.48	0.54
Wch-55	191.33	0.00	4.07	9.84	8.18	2.34	0.00
Wch-37	192.75	0.00	7.33	23.22	24.07	5.04	0.35
Wch-38	193.75	0.00	2.57	6.69	4.03	1.59	0.17

Wch-39	195.42	0.00	5.98	21.13	16.80	4.40	0.17
Wch-56	203.08	0.00	8.43	27.63	21.72	5.01	0.00
Wch-57	207.00	0.00	4.68	12.95	9.49	2.75	0.00
Wch-58	209.92	0.00	1.71	2.44	2.75	0.76	0.00

Table 3. Isorenieratane/Paleorenieratane ratios for LCMS and GCMS, GCMS data taken from Connock et al. 2018

sample	depth (ft)	Isorenieratane/ Paleorenieratane LCMS	Isorenieratane/ Paleorenieratane GCMS
WCH-1	74.00	0.42	
WCH-2	75.50	0.62	
WCH-3	77.08	0.55	
WCH-4	78.00	0.46	
WCH-5	79.67	0.57	
WCH-6	80.67	0.50	
WCH-7	81.00	0.58	
WCH-8	84.50	0.46	
WCH-9	88.00	0.54	
WCH-10	91.50	0.77	
Wch-40	93.83	0.57	0.40
WCH-11	94.33	0.53	
WCH-12	98.00	0.61	
WCH-13	102.17	2.29	
WCH-14	105.50	2.44	
Wch-41	109.17	1.77	0.90
Wch-42	112.50	2.00	1.86
WCH-15	115.00	1.63	
WCH-16	118.00	1.76	
WCH-17	121.00	0.59	
WCH-18	124.42	0.54	
Wch-43	126.17	0.37	0.29
WCH-19	129.00	0.22	
WCH-20	130.00	0.31	
Wch-60	131.75	0.33	0.26
Wch-61	132.75	0.21	0.16
WCH-21	133.50	0.31	
Wch-44	134.00	0.30	0.20
WCH-22	136.00	0.28	
WCH-23	137.25	0.27	
WCH-24	138.50	0.29	
WCH-25	139.67	0.32	
WCH-26	141.08	0.26	
WCH-27	142.25	0.23	
WCH-28	143.50	0.22	
Wch-45	145.17	0.22	0.15
WCH-29	146.00	0.20	
WCH-30	147.08	0.20	
WCH-31	149.25	0.18	
Wch-46	153.58	0.31	0.24
Wch-47	160.17	0.36	0.29
Wch-48	160.83	0.42	0.35
Wch-49	169.33	0.42	0.33
Wch-50	170.92	0.47	0.38
Wch-51	172.00	0.62	0.49
Wch-52	172.42	1.35	0.65
Wch-53	173.83	1.26	1.19
Wch-54	174.42	1.09	0.99
Wch-32	181.92	2.49	1.54
Wch-33	185.92	1.78	0.63

Wch-34	186.42	2.05	1.43
Wch-35	187.75	1.02	0.76
Wch-36	191.08	0.69	0.61
Wch-55	191.33	1.20	1.00
Wch-37	192.75	0.96	0.56
Wch-38	193.75	1.66	1.59
Wch-39	195.42	1.26	1.12
Wch-56	203.08	1.27	1.12
Wch-57	207.00	1.36	1.21
Wch-58	209.92	0.89	1.67

Table 4. Porphyrin sums of each class of compound. BiCAP, DPEP, and ETIO reported in ng/g OC

Sample	Depth (ft)	VO-BiCAP (ng/g OC)	Ni-BiCAP (ng/g OC)	VO-DPEP (ng/g OC)	Ni-DPEP (ng/g OC)	VO-ETIO (ng/g OC)	Ni-ETIO (ng/g OC)
WCH-1	74.00	30.91	400.62	69.86	1226.78	12.00	1468.88
WCH-2	75.50	122.58	1318.49	180.32	4040.24	25.89	4147.96
WCH-3	77.08	108.69	510.34	124.78	1952.99	30.54	2686.11
WCH-4	78.00	91.87	1422.44	166.34	4850.82	21.04	4256.90
WCH-5	79.67	294.61	1262.37	409.53	2848.97	80.44	3062.79
WCH-6	80.67	197.12	373.60	385.65	1525.06	71.86	2101.18
WCH-7	81.00	748.08	642.68	1040.04	2442.31	207.10	2614.80
WCH-8	84.50	348.14	607.68	480.51	2478.33	99.43	2684.43
WCH-9	88.00	230.44	1039.07	322.65	3344.55	73.24	3458.51
WCH-10	91.50	4515.86	210.00	5838.20	913.05	1369.90	1181.21
WCH-40	93.83	182.98	110.89	205.93	315.44	37.03	292.07
WCH-11	94.33	2122.29	213.38	2193.37	1067.99	427.20	1454.81
WCH-12	98.00	174.88	55.27	231.65	548.04	47.74	959.32
WCH-13	102.17	1275.46	143.80	1110.89	726.02	209.32	852.06
WCH-14	105.50	2197.96	167.94	1971.55	873.69	374.21	1085.00
WCH-41	109.17	3524.59	492.90	2799.63	1551.21	417.60	1060.32
WCH-42	112.50	1332.84	110.35	1155.00	540.08	155.19	370.56
WCH-15	115.00	1527.55	240.01	1154.15	1008.80	229.01	1128.56
WCH-16	118.00	266.33	102.35	221.90	366.40	43.97	375.26
WCH-17	121.00	460.58	4.40	375.09	159.13	65.49	319.32
WCH-18	124.42	578.58	9.86	514.88	112.63	77.29	107.86
WCH-43	126.17	109.11	0.00	117.56	106.10	10.39	147.03
WCH-19	129.00	136.77	0.00	105.35	67.04	11.55	164.37
WCH-20	130.00	74.83	0.00	65.15	4.16	1.71	23.96
WCH-60	131.75	556.35	1.97	440.44	26.52	45.55	47.63
WCH-61	132.75	551.15	27.92	463.69	191.68	57.70	290.36
WCH-21	133.50	396.95	75.74	342.32	863.30	43.12	1608.85
WCH-44	134.00	166.55	7.03	156.02	90.08	20.00	185.08
WCH-22	136.00	510.70	166.36	450.59	1685.81	46.41	3604.12
WCH-23	137.25	379.27	95.27	310.70	943.32	31.27	1755.95
WCH-24	138.50	676.12	119.38	542.79	1032.13	41.56	1560.18
WCH-25	139.67	770.57	119.18	689.40	987.33	64.16	1467.65
WCH-26	141.08	930.98	106.05	824.13	1054.40	68.21	1441.74
WCH-27	142.25	709.28	261.32	685.51	2066.52	66.49	2776.08
WCH-28	143.50	823.49	278.07	915.57	2350.70	77.03	3458.48
WCH-45	145.17	346.71	21.22	377.28	215.95	29.29	248.45
WCH-29	146.00	944.83	288.83	1066.33	2422.85	100.47	3292.29
WCH-30	147.08	702.62	365.13	817.62	2917.77	71.63	3316.36
WCH-31	149.25	541.20	186.56	589.35	1615.58	48.57	2438.31
WCH-46	153.58	851.26	3.57	649.80	49.78	50.81	107.97
WCH-47	160.17	406.25	6.82	293.90	98.82	13.71	215.22
WCH-48	160.83	428.70	7.44	284.63	91.43	23.22	182.05
WCH-49	169.33	536.82	9.61	330.64	122.82	24.85	197.42
WCH-50	170.92	566.61	2.23	414.28	39.72	38.07	64.89
WCH-51	172.00	98.09	4.61	60.68	101.56	7.02	123.94
WCH-52	172.42	524.82	42.40	387.50	375.24	41.42	358.23

WCH-53	173.83	728.38	5.61	580.59	45.35	63.95	49.26
WCH-54	174.42	313.11	26.78	255.94	122.58	14.52	159.40
WCH-32	181.92	543.96	203.53	440.93	626.03	42.04	338.94
WCH-33	185.92	1031.48	444.12	960.86	1217.38	89.68	521.91
WCH-34	186.42	1717.07	729.74	1860.13	1947.93	191.31	937.08
WCH-35	187.75	317.77	50.09	323.25	180.89	36.61	102.05
WCH-36	191.08	102.66	15.61	76.06	86.58	6.17	64.80
WCH-55	191.33	362.56	80.24	263.12	430.57	19.64	427.00
WCH-37	192.75	229.88	4.18	159.08	23.75	13.29	24.32
WCH-38	193.75	165.57	16.53	114.29	54.95	9.02	48.68
WCH-39	195.42	142.55	13.96	96.56	41.86	6.51	43.83
WCH-56	203.08	471.96	71.75	435.90	383.53	41.09	436.78
WCH-57	207.00	451.38	5.33	325.93	27.96	31.74	24.20
WCH-58	209.92	289.14	9.06	234.39	31.25	12.01	55.62

Table 5. VO/Ni porphyrin ratio, DPEP/ETIO ratio, and T_{max}. T_{max} data taken from Connock et al. 2018

sample	depth (ft)	VO/Ni Porphyrins	DPEP/ETIO	Tmax
WCH-1	74.00	0.04	0.88	
WCH-2	75.50	0.03	1.01	
WCH-3	77.08	0.05	0.76	
WCH-4	78.00	0.03	1.17	
WCH-5	79.67	0.11	1.04	
WCH-6	80.67	0.16	0.88	
WCH-7	81.00	0.35	1.23	
WCH-8	84.50	0.16	1.06	
WCH-9	88.00	0.08	1.04	
WCH-10	91.50	5.09	2.65	
Wch-40	93.83	0.60	1.59	428
WCH-11	94.33	1.73	1.73	
WCH-12	98.00	0.29	0.77	
WCH-13	102.17	1.51	1.73	
WCH-14	105.50	2.14	1.95	
Wch-41	109.17	2.17	2.94	426
Wch-42	112.50	2.59	3.22	427
WCH-15	115.00	1.22	1.59	
WCH-16	118.00	0.63	1.40	
WCH-17	121.00	1.87	1.39	
WCH-18	124.42	5.08	3.39	
Wch-43	126.17	0.93	1.42	424
WCH-19	129.00	1.10	0.98	
WCH-20	130.00	5.04	2.70	
Wch-60	131.75	13.69	5.01	416
Wch-61	132.75	2.10	1.88	420
WCH-21	133.50	0.31	0.73	
Wch-44	134.00	1.21	1.20	424
WCH-22	136.00	0.18	0.59	
WCH-23	137.25	0.26	0.70	
WCH-24	138.50	0.46	0.98	
WCH-25	139.67	0.59	1.09	
WCH-26	141.08	0.70	1.24	
WCH-27	142.25	0.29	0.97	
WCH-28	143.50	0.30	0.92	
Wch-45	145.17	1.54	2.14	421
WCH-29	146.00	0.35	1.03	
WCH-30	147.08	0.24	1.10	
WCH-31	149.25	0.28	0.89	
Wch-46	153.58	9.58	4.39	416
Wch-47	160.17	2.22	1.72	419
Wch-48	160.83	2.62	1.83	418

Wch-49	169.33	2.71	2.04	419
Wch-50	170.92	9.54	4.41	410
Wch-51	172.00	0.72	1.24	421
Wch-52	172.42	1.23	1.91	422
Wch-53	173.83	13.70	5.53	418
Wch-54	174.42	1.89	2.18	426
Wch-32	181.92	0.88	2.80	427
Wch-33	185.92	1.12	3.74	423
Wch-34	186.42	1.04	3.37	424
Wch-35	187.75	2.03	3.64	420
Wch-36	191.08	1.11	2.29	421
Wch-55	191.33	0.69	1.55	424
Wch-37	192.75	7.70	4.86	421
Wch-38	193.75	2.40	2.93	423
Wch-39	195.42	2.46	2.75	420
Wch-56	203.08	1.06	1.71	424
Wch-57	207.00	14.07	6.33	419
Wch-58	209.92	5.58	3.93	419

Table 6. MTTC concentrations in ng/g OC.

Sample	Depth (ft)	β-MTTC (ng/g OC)	γ-MTTC (ng/g OC)	ζ-MTTC (ng/g OC)	α-MTTC (ng/g OC)	MTTCI (α-MTTC/total MTTC)
WCH-1	74.00	1.85	1.10	6.10	48.60	0.84
WCH-2	75.50	2.09	2.23	1.64	86.73	0.94
WCH-3	77.08	1.92	6.08	1.94	76.83	0.89
WCH-4	78.00	2.29	7.28	1.15	57.61	0.84
WCH-5	79.67	2.60	6.81	1.98	104.57	0.90
WCH-6	80.67	1.63	6.25	1.73	42.98	0.82
WCH-7	81.00	2.64	7.05	2.65	85.74	0.87
WCH-8	84.50	1.89	5.62	1.82	56.98	0.86
WCH-9	88.00	1.73	1.68	1.70	57.25	0.92
WCH-10	91.50	1.80	2.21	1.16	28.12	0.84
WCH-40	93.83	5.18	1.02	3.55	164.77	0.94
WCH-11	94.33	2.08	3.46	1.50	22.85	0.76
WCH-12	98.00	1.13	1.89	0.67	7.74	0.68
WCH-13	102.17	0.92	0.54	0.52	8.02	0.80
WCH-14	105.50	0.79	0.50	0.31	9.07	0.85
WCH-41	109.17	0.92	0.28	0.25	15.95	0.92
WCH-42	112.50	0.38	0.27	0.21	7.68	0.90
WCH-15	115.00	0.20	0.37	0.24	3.16	0.80
WCH-16	118.00	0.27	0.26	0.12	1.57	0.71
WCH-17	121.00	0.57	0.95	0.43	3.55	0.65
WCH-18	124.42	0.28	0.68	0.36	1.48	0.53
WCH-43	126.17	0.64	0.35	0.18	5.67	0.83
WCH-19	129.00	0.48	0.80	0.65	4.08	0.68
WCH-20	130.00	0.34	0.50	0.38	1.16	0.49
WCH-60	131.75	0.69	0.19	1.35	5.39	0.71
WCH-61	132.75	0.60	0.00	0.92	14.61	0.91
WCH-21	133.50	0.92	0.75	1.17	17.55	0.87
WCH-44	134.00	1.31	0.40	0.58	13.53	0.85
WCH-22	136.00	0.58	0.83	1.12	16.74	0.87
WCH-23	137.25	1.13	0.57	0.75	19.79	0.89
WCH-24	138.50	1.11	0.51	0.48	17.57	0.89
WCH-25	139.67	0.66	0.74	0.59	17.55	0.90
WCH-26	141.08	0.76	0.69	0.78	19.24	0.90
WCH-27	142.25	0.93	0.38	0.92	21.03	0.90
WCH-28	143.50	0.87	0.62	0.89	24.06	0.91
WCH-45	145.17	1.19	0.29	0.51	20.04	0.91
WCH-29	146.00	0.98	0.52	0.83	23.55	0.91
WCH-30	147.08	1.36	0.46	1.12	34.32	0.92

WCH-31	149.25	1.34	0.70	0.86	31.56	0.92
WCH-46	153.58	1.09	0.67	0.52	16.69	0.88
WCH-47	160.17	0.73	0.28	0.87	13.94	0.88
WCH-48	160.83	0.65	0.60	0.76	14.65	0.88
WCH-49	169.33	0.61	0.34	0.57	14.15	0.90
WCH-50	170.92	0.56	1.10	0.81	10.37	0.81
WCH-51	172.00	0.38	0.25	0.45	7.31	0.87
WCH-52	172.42	0.17	0.18	0.21	5.95	0.91
WCH-53	173.83	0.47	1.02	0.38	9.01	0.83
WCH-54	174.42	0.35	0.21	0.22	5.92	0.88
WCH-32	181.92	0.79	0.56	0.39	16.30	0.90
WCH-33	185.92	3.66	1.50	3.65	65.11	0.88
WCH-34	186.42	0.81	0.16	0.50	12.76	0.90
WCH-35	187.75	0.34	0.31	0.30	9.87	0.91
WCH-36	191.08	0.38	0.18	0.39	11.85	0.93
WCH-55	191.33	0.52	0.23	0.42	7.09	0.86
WCH-37	192.75	0.41	0.18	0.26	10.69	0.93
WCH-38	193.75	0.20	0.15	0.16	3.65	0.88
WCH-39	195.42	0.20	0.18	0.14	6.60	0.93
WCH-56	203.08	0.54	0.23	0.50	9.75	0.88
WCH-57	207.00	0.46	0.78	0.16	6.13	0.81
WCH-58	209.92	0.23	0.10	0.09	1.34	0.76

Table 7. Trimethylphytylbenzoquinone (TMPBQ) concentrations separated by isomer peaks identified in the chromatograph reported in ng/g OC

Sample	Depth (ft)	TMPBQ Peak 1 (ng/g OC)	TMPBQ Peak 2 (ng/g OC)	TMPBQ Peak 3 (ng/g OC)	Total TMPBQ (ng/g OC)	TMPBQ peak ratio (2+3)/1	TMPBQ/ α-MTTC
WCH-1	74.00	7.07	2.23	3.70	13.00	0.84	0.27
WCH-2	75.50	8.98	6.34	11.59	26.91	2.00	0.31
WCH-3	77.08	5.28	0.00	5.87	11.15	1.11	0.15
WCH-4	78.00	9.40	0.00	4.00	13.39	0.43	0.23
WCH-5	79.67	6.22	1.55	6.52	14.29	1.30	0.14
WCH-6	80.67	4.22	0.00	3.89	8.10	0.92	0.19
WCH-7	81.00	5.32	1.20	6.47	12.99	1.44	0.15
WCH-8	84.50	4.52	1.93	5.01	11.46	1.54	0.20
WCH-9	88.00	5.34	3.58	4.91	13.83	1.59	0.24
WCH-10	91.50	7.00	5.18	4.07	16.25	1.32	0.58
Wch-40	93.83	3.50	2.25	3.29	9.04	1.58	0.22
WCH-11	94.33	5.89	2.58	2.53	11.00	0.87	0.48
WCH-12	98.00	4.26	2.19	1.17	7.62	0.79	0.98
WCH-13	102.17	2.20	2.47	1.06	5.72	1.61	0.71
WCH-14	105.50	2.13	1.13	2.06	5.32	1.49	0.59
Wch-41	109.17	0.95	0.12	0.62	1.70	0.78	0.11
Wch-42	112.50	1.12	0.00	0.00	1.12	0	0.15
WCH-15	115.00	0.79	0.05	0.52	1.37	0.73	0.43
WCH-16	118.00	0.17	0.03	0.04	0.23	0.41	0.15
WCH-17	121.00	0.00	0.00	0.00	0.00	0	0
WCH-18	124.42	0.00	0.00	0.00	0.00	0	0
Wch-43	126.17	0.00	0.00	0.00	0.00	0	0
WCH-19	129.00	0.00	0.00	0.00	0.00	0	0
WCH-20	130.00	0.00	0.00	0.00	0.00	0	0
Wch-60	131.75	0.09	0.00	0.06	0.15	0.61	0.03
Wch-61	132.75	0.00	0.93	1.17	2.09	0	0.14
WCH-21	133.50	0.46	1.08	1.08	2.63	4.67	0.15
Wch-44	134.00	0.00	0.93	1.60	2.53	0	0.19
WCH-22	136.00	0.47	0.32	1.07	1.86	2.96	0.11
WCH-23	137.25	0.00	1.24	1.47	2.71	0	0.14
WCH-24	138.50	0.00	0.61	1.06	1.67	0	0.10
WCH-25	139.67	0.00	0.83	1.07	1.90	0	0.11
WCH-26	141.08	0.00	0.74	1.37	2.11	0	0.11

WCH-27	142.25	0.26	1.23	1.57	3.06	10.93	0.15
WCH-28	143.50	0.30	1.04	1.51	2.85	8.53	0.12
Wch-45	145.17	0.00	1.74	2.50	4.24	0	0.23
WCH-29	146.00	0.00	1.26	1.69	2.95	0	0.13
WCH-30	147.08	0.81	1.99	2.85	5.66	5.96	0.16
WCH-31	149.25	0.00	1.61	2.21	3.82	0	0.12
Wch-46	153.58	0.00	0.50	1.82	2.32	0	0.17
Wch-47	160.17	0.00	0.38	1.85	2.23	0	0.16
Wch-48	160.83	0.00	0.32	0.78	1.10	0	0.08
Wch-49	169.33	0.00	0.00	1.12	1.12	0	0.08
Wch-50	170.92	0.00	0.00	0.92	0.92	0	0.09
Wch-51	172.00	0.00	0.00	0.18	0.18	0	0.03
Wch-52	172.42	0.00	0.00	0.14	0.14	0	0.02
Wch-53	173.83	0.00	0.00	0.24	0.24	0	0.03
Wch-54	174.42	0.00	0.00	0.23	0.23	0	0.04
Wch-32	181.92	1.05	0.85	0.28	2.17	1.08	0.13
Wch-33	185.92	0.61	0.45	0.38	1.44	1.38	0.12
Wch-34	186.42	0.56	0.80	0.19	1.55	1.77	0.12
Wch-35	187.75	0.00	0.11	0.53	0.64	0	0.06
Wch-36	191.08	0.00	0.00	0.59	0.59	0	0.05
Wch-55	191.33	0.00	0.00	0.16	0.16	0	0.02
Wch-37	192.75	0.00	0.00	0.63	0.63	0	0.06
Wch-38	193.75	0.10	0.00	0.00	0.10	0	0.03
Wch-39	195.42	0.00	0.15	0.11	0.25	0	0.04
Wch-56	203.08	0.00	0.00	0.71	0.71	0	0.07
Wch-57	207.00	0.00	0.00	0.00	0.00	0	0
Wch-58	209.92	0.00	0.00	0.00	0.00	0	0

Table 8. $\delta^{13}C$ whole organic carbon values. Samples are marked if they came from previous studies or this study's samples *(Molinares-Blanco, 2019)*

Sample	Depth (ft)	$\delta^{13}C$
Molinares (2019)	70.60	-29.72
Molinares (2019)	73.60	-28.81
Wch-1	74.00	-29.04
Wch-2	75.50	-30.36
Wch-3	77.80	-30.28
Molinares (2019)	79.60	-29.12
Molinares (2019)	83.01	-29.78
Molinares (2019)	86.20	-29.78
Molinares (2019)	89.01	-28.82
Molinares (2019)	93.60	-28.65
Molinares (2019)	98.00	-27.94
Molinares (2019)	104.20	-29.04
Wch-41	109.17	-29.08
Molinares (2019)	109.40	-28.71
Molinares (2019)	111.90	-29.27
Molinares (2019)	114.80	-29.29
Molinares (2019)	119.30	-29.64
Molinares (2019)	120.59	-29.91
Molinares (2019)	122.05	-29.16
Molinares (2019)	124.60	-29.42
Wch-43	126.17	-27.00
Molinares (2019)	129.10	-29.08
Wch-20	130.00	-29.28
Molinares (2019)	132.10	-28.30
Wch-21	133.50	-29.23
Molinares (2019)	134.30	-28.65
Wch-22	136.00	-29.44
Molinares (2019)	136.01	-28.97
Molinares (2019)	137.40	-28.88

Molinares (2019)	139.80	-29.06
Molinares (2019)	143.80	-28.71
Wch-45	145.17	-28.87
Molinares (2019)	147.10	-28.94
Molinares (2019)	151.01	-29.15
Molinares (2019)	153.20	-28.90
Molinares (2019)	156.30	-28.74
Molinares (2019)	160.50	-29.62
Wch-48	160.83	-29.36
Molinares (2019)	163.20	-29.39
Molinares (2019)	165.20	-30.15
Wch-54	174.42	-29.03
Molinares (2019)	181.00	-29.67
Wch-32	181.92	-28.50
Molinares (2019)	191.20	-28.76
Wch-55	191.33	-28.57
Molinares (2019)	202.70	-29.89
Wch-56	203.08	-29.37

APPENDIX III Chromatograms

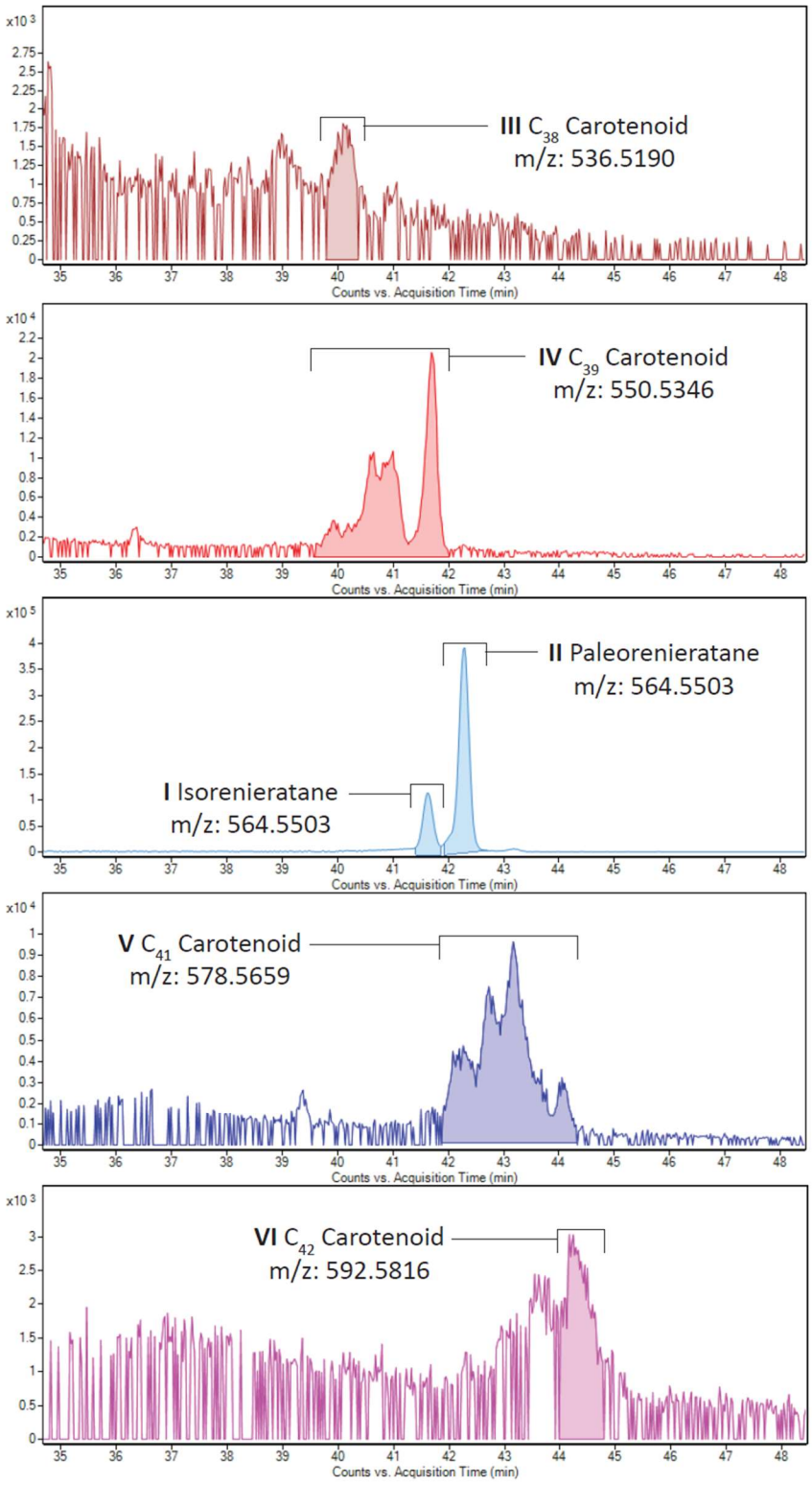

Figure 34. Chromatograms of the aromatic carotenoids with the peaks of interest highlighted.

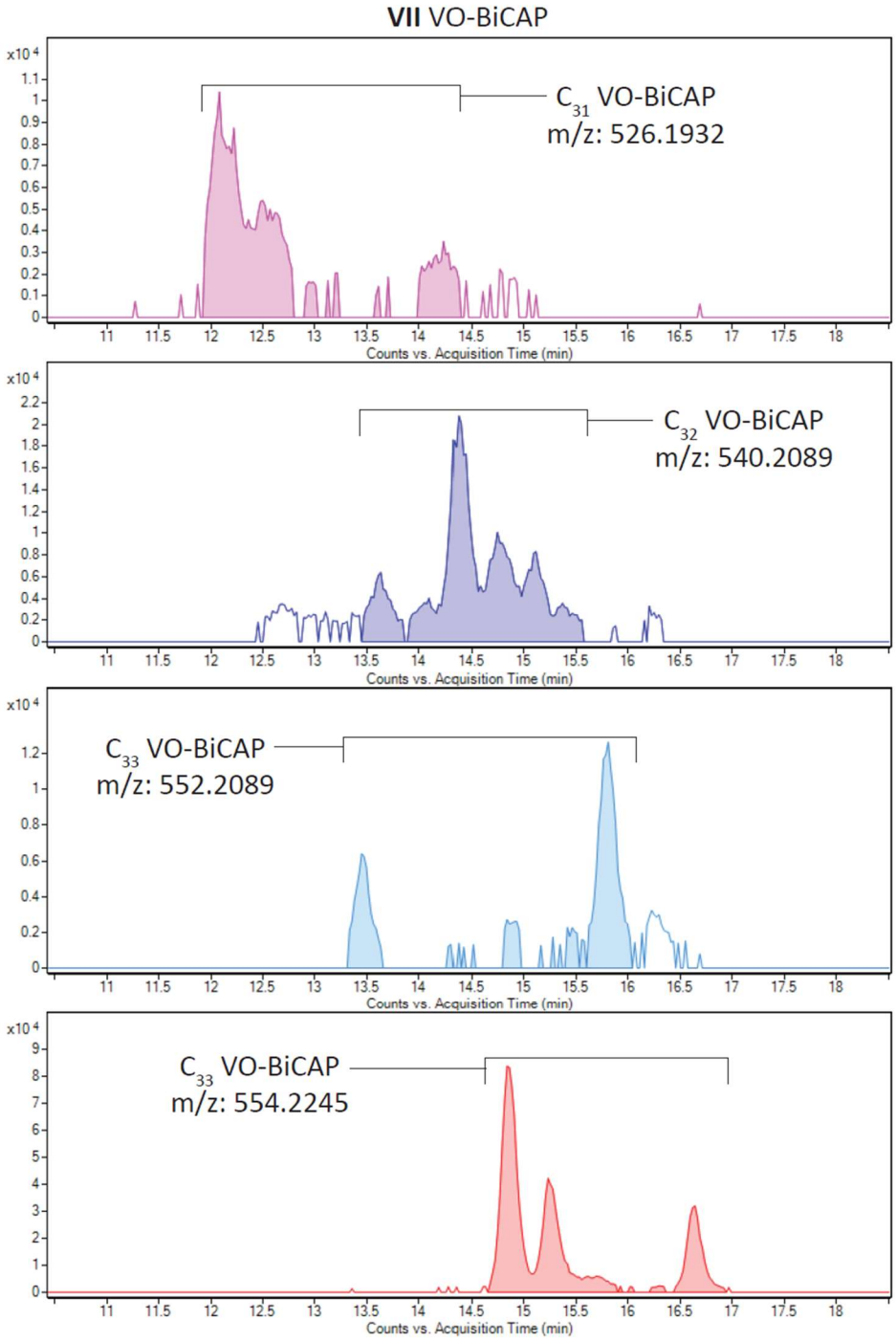

Figure 35. Chromatograms of the VO-BiCAP porphyrins. Peaks of interest are highlighted.

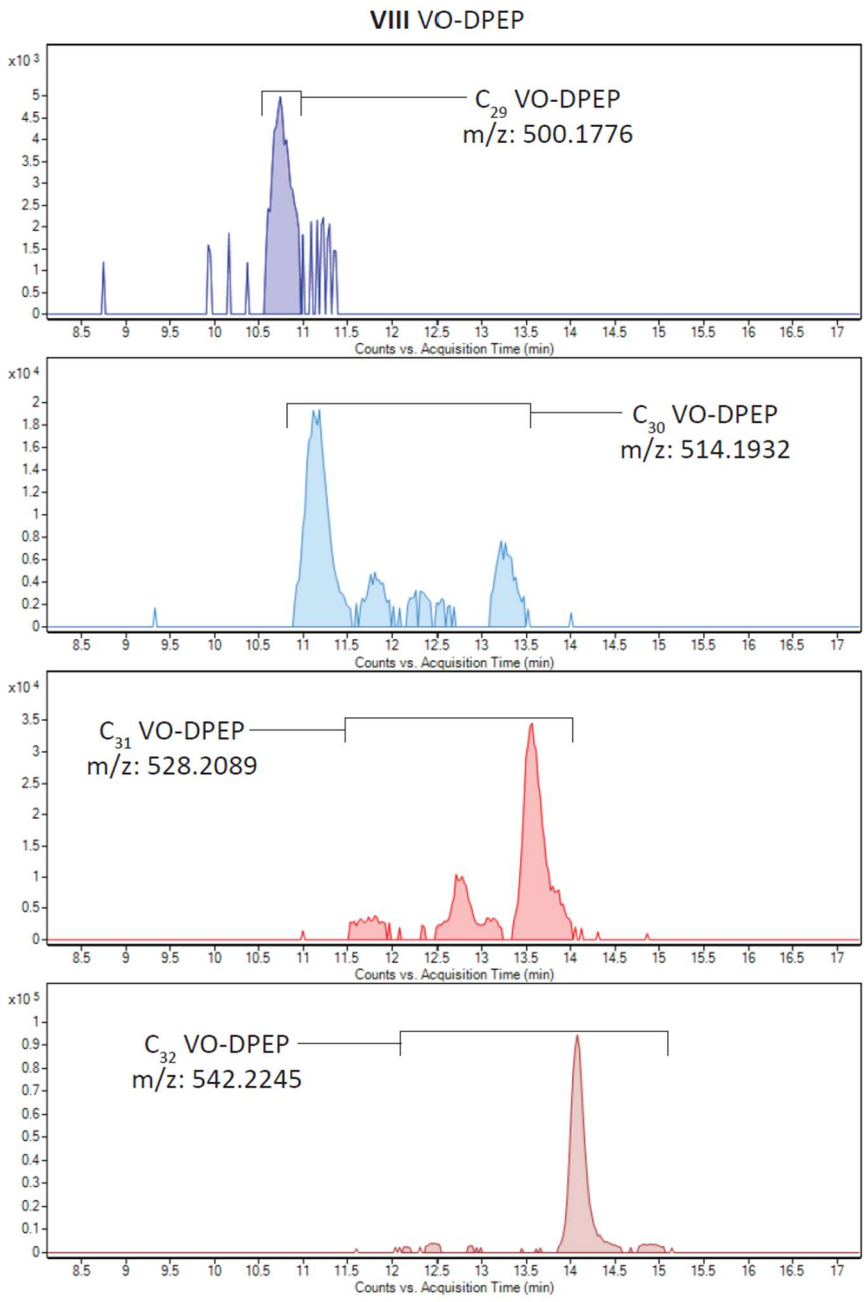

Figure 36. Chromatograms of the VO-DPEP porphyrins. Peaks of interested are highlighted.

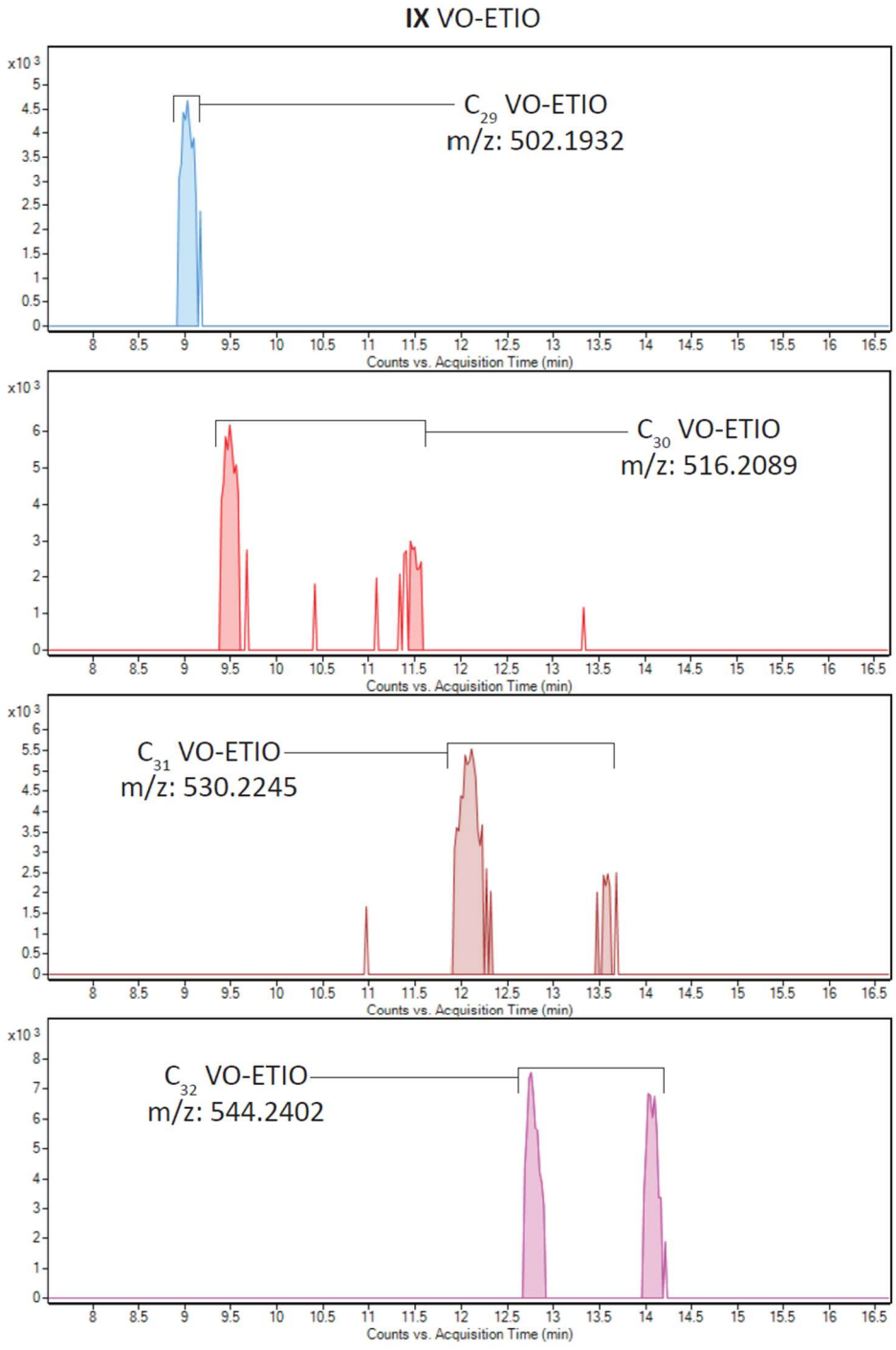

Figure 37. Chromatograms of the VO-ETIO porphyrins. Peaks of interested are highlighted.

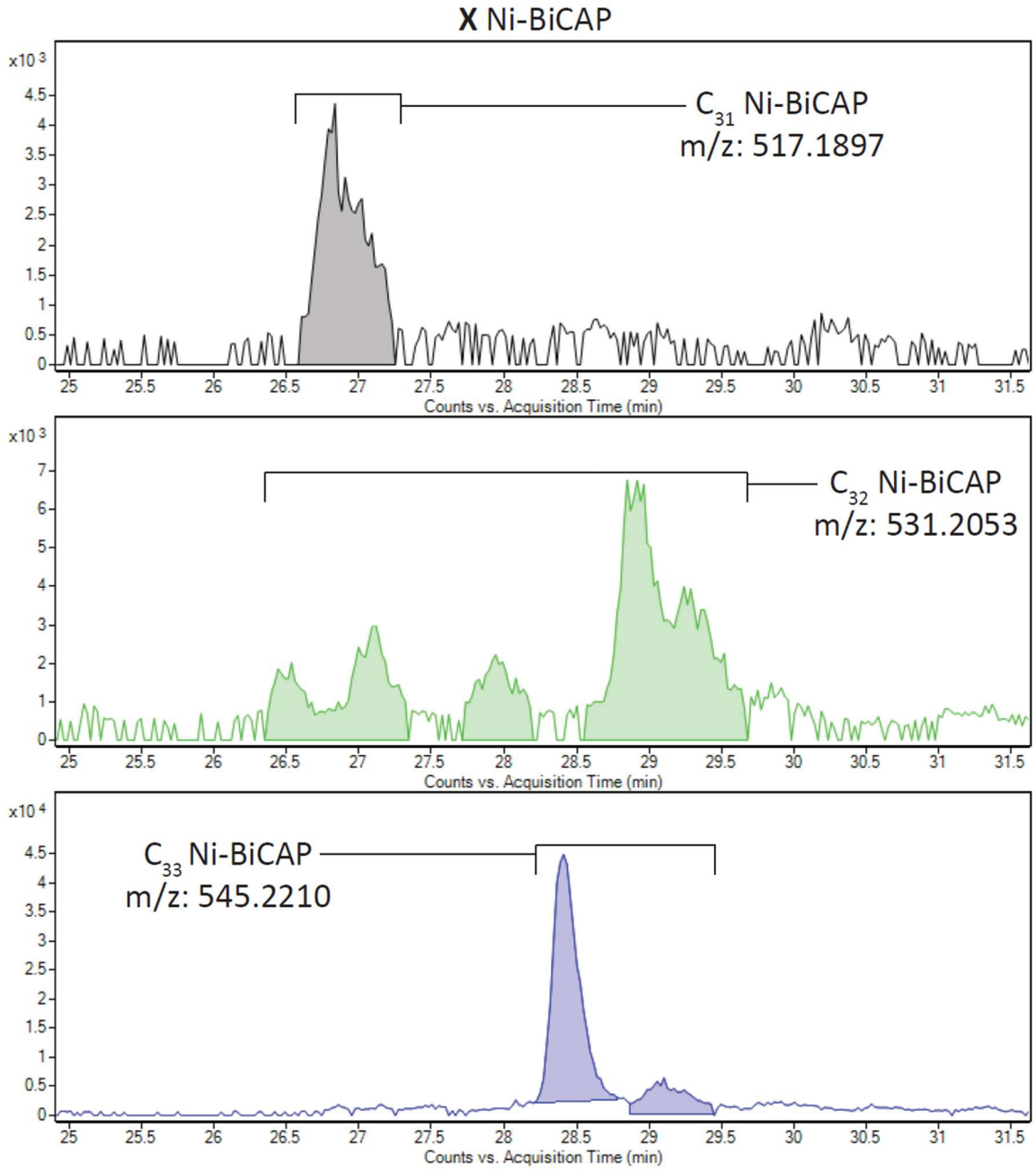

Figure 38. Chromatograms of the Ni-BiCAP porphyrins. Peaks of interest are highlighted.

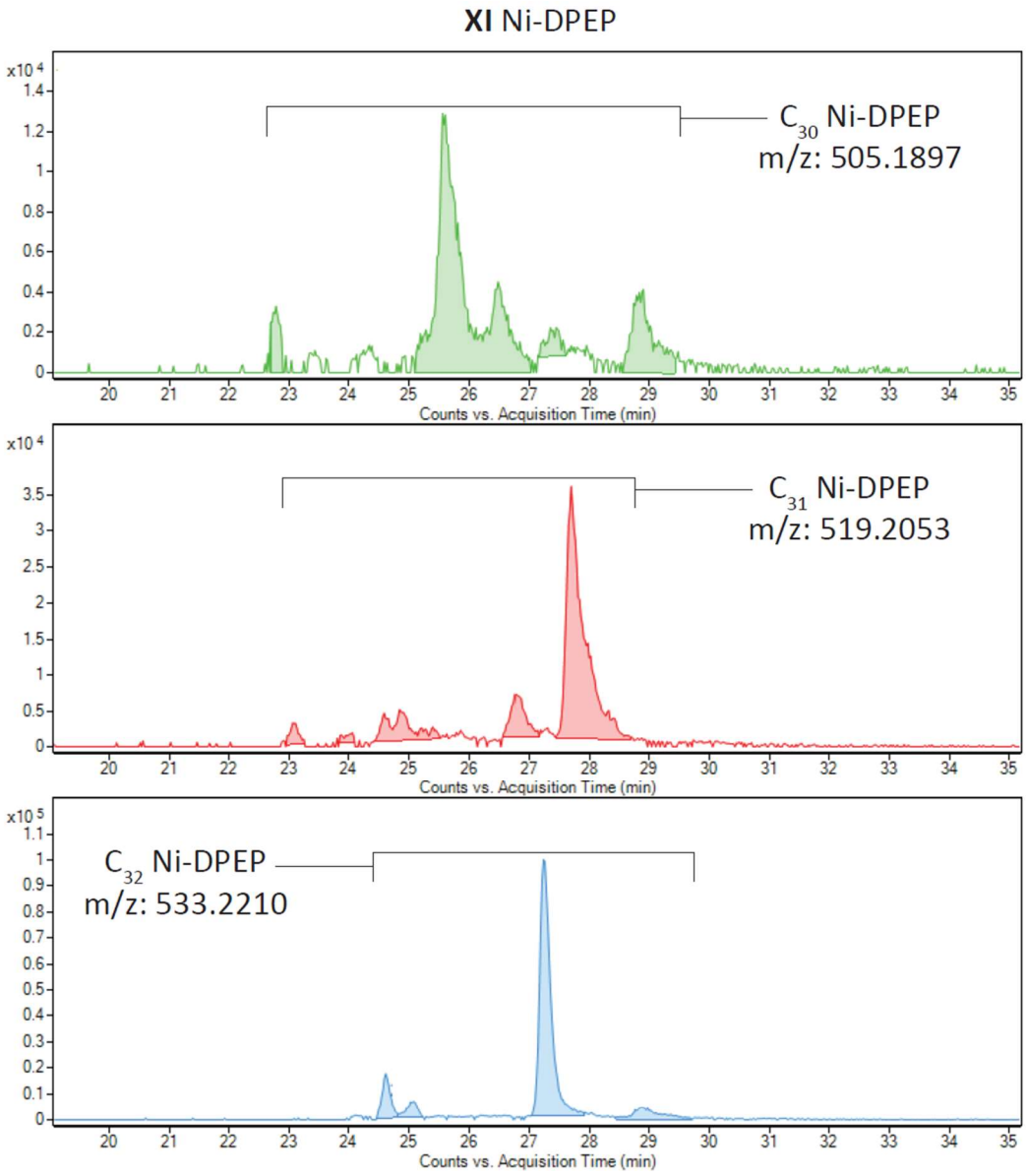

Figure 39. Chromatograms of the Ni-DPEP porphyrins. Peaks of interest are highlighted.

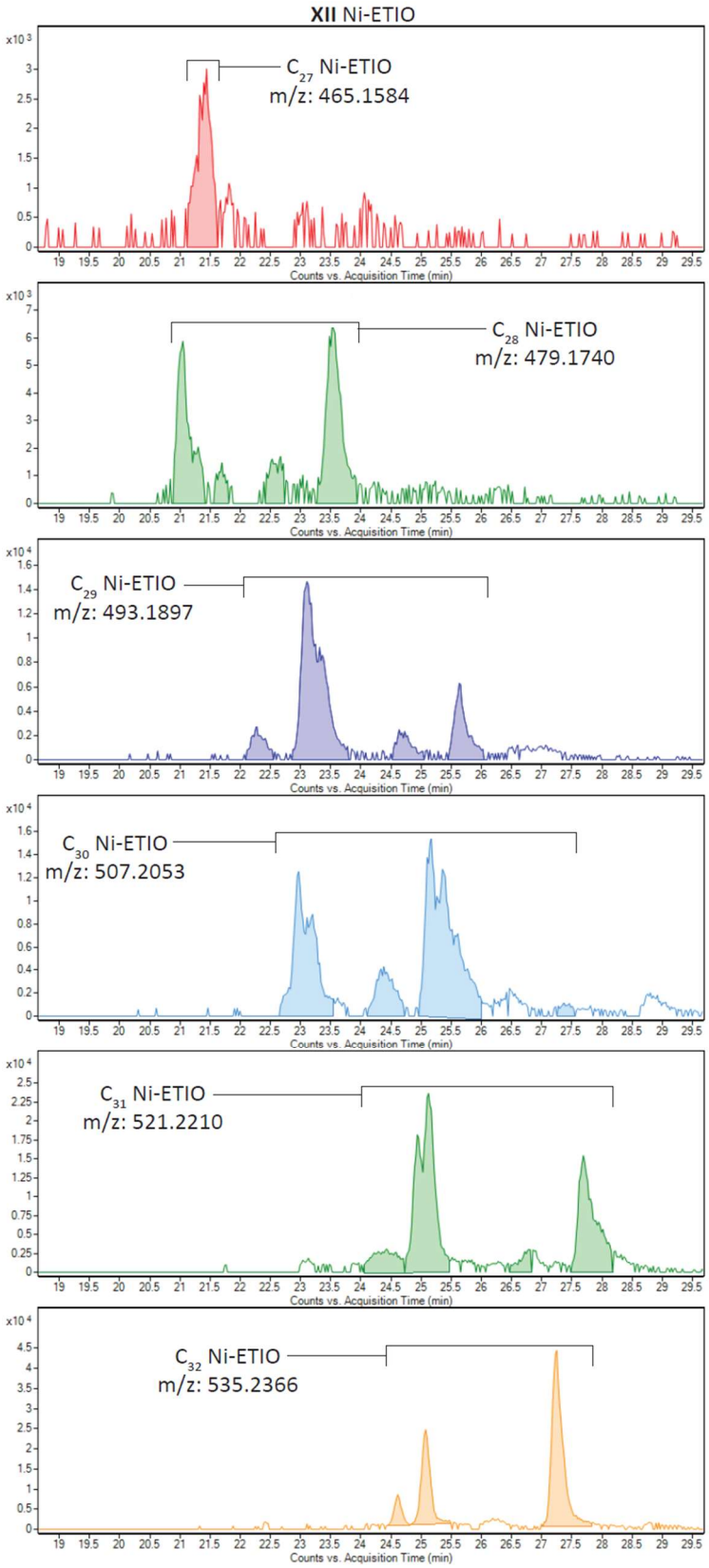

Figure 40. Chromatograms of the Ni-ETIO porphyrins. Peaks of interest are highlighted.